In Vivo Quantitative MRI of Hemodynamics, Endothelial Function, and Metabolites

by

Sultan Zaman Mahmud

A dissertation submitted to the Graduate Faculty of
Auburn University
in partial fulfillment of the
requirements for the Degree of
Doctor of Philosophy

Auburn, Alabama
May 6, 2023

Keywords: MRI, Blood Flow, Perfusion, Venous Oxygen Saturation, Blood-Brain Barrier, MR Spectroscopic Imaging

Approved by

Adil Bashir, Ph.D., Chair, Associate Professor of Electrical and Computer Engineering
Thomas S. Denney Jr., Ph.D., Professor of Electrical and Computer Engineering
Shiwen Mao, Ph.D., Professor of Electrical and Computer Engineering
Meredith Reid, Ph.D., Assistant Professor of Electrical and Computer Engineering
Emily C. Graff, Ph.D., Associate Professor of Pathobiology

Abstract

Magnetic resonance (MR) hemodynamic imaging involves the study of vascular blood circulation. The regulation of tissue oxygenation depends directly on the regulation of blood flow. Impaired blood flow, oxygen supply, oxygen consumption, and vascular integrity are major contributors to organ dysfunction as these can limit the supply of nutrients and clearance of toxic substrates. MR metabolite imaging, also known as MR spectroscopic imaging (MRSI), is the detection and quantification of in vivo chemical compounds (metabolites) by protons (^{1}H), phosphorus (^{31}P), or other atoms attached to the molecules. Changes in metabolite content are an early marker of diseases and in general, may precede anatomical/structural changes. Therefore, efficient techniques for robust measurement of blood flow, endothelial function, and metabolite content can be very beneficial to investigate pathology in various organs.

The specific goals of this work were: (i) to determine the feasibility of a novel technique for real-time simultaneous measurement of arterial blood flow, perfusion, venous oxygen saturation, and bioenergetics (^{31}P MRS) in the human skeletal muscle; (ii) to develop a novel technique to measure perfusion and blood-brain barrier (BBB) permeability using magnetization transfer (MT) and arterial spin labeling (ASL) in the human brain; (iii) to develop a robust technique for high-resolution fast ^{1}H MRSI of the human brain using non-Cartesian (rosette) trajectory; and (iv) to demonstrate high-resolution human spinal cord imaging using motion-insensitive rosette trajectory with MT preparation and compressed sensing MRI. The overarching goal of the work presented here is to develop new non-invasive techniques that can provide novel information about pathology and help monitor disease progression and the efficacy of treatment.

Acknowledgments

I would like to thank my advisor, Dr. Bashir for his guidance and support. Without his supervision, this journey would not have been possible. I would also like to thank other committee members, Dr. Denney, Dr. Mao, Dr. Reid, and Dr. Graff for their support and helpful suggestions. I would like to extend my gratitude to Dr. Beyers and Julie for their help throughout this journey. Last but not the least, I would like to thank my parents, my brothers, and Nasim for their help and support.

Table of Contents

List of Tables

List of Figures

List of Abbreviations

ASL	Arterial Spin Labeling
ATT	Arterial Transit Time
BBB	Blood-Brain Barrier
CASL	Continuous Arterial Spin Labeling
CBF	Cerebral Blood Flow
CBV	Cerebral Blood Volume
CNR	Contrast-to-Noise Ratio
CNS	Central Nervous System
CS	Compressed Sensing
CSF	Cerebrospinal Fluid
CSI	Chemical Shift Imaging
FAIR	Flow-Sensitive Alternating Inversion Recovery
FID	Free Induction Decay
FLASH	Fast Low Angle Shot
FOV	Field of View
GM	Gray Matter
GRE	Gradient Recalled Echo
IRB	Institutional Review Board
MRI	Magnetic Resonance Imaging
MRS	Magnetic Resonance Spectroscopy
MRSI	Magnetic Resonance Spectroscopic Imaging
MT	Magnetization Transfer

MTR	Magnetization Transfer Ratio
PASL	Pulsed Arterial Spin Labeling
PLD	Post-Labeling Delay
PS	Permeability Surface Area Product
RF	Radio Frequency
RSI	Rosette Spectroscopic Imaging
SAR	Specific Absorption Rate
SATIR	Saturation Inversion Recovery
SBW	Spectral Bandwidth
SC	Spinal Cord
SNR	Signal-to-Noise Ratio
SvO_2	Venous Oxygen Saturation
TE	Echo Time
TR	Repetition Time
UHF	Ultra-High Field
WM	White Matter
^{1}H MRS	Proton Magnetic Resonance Spectroscopy
^{31}P MRS	Phosphorus Magnetic Resonance Spectroscopy

Chapter 1

Introduction

Hemodynamics refers to "the physical study of flowing blood and of all solid structures through which it flows" [1]. Therefore, hemodynamic imaging involves the study of vascular blood flow and vessel integrity. Blood flow consists of a macrovascular component that refers to the global transport of blood through the arteries, and a microvascular component (perfusion) that is the delivery of the vascular blood to the tissue. Blood flow regulates the supply of oxygen and other nutrients to the tissue, which is very crucial for the healthy functioning of any organ [2]. Adequate oxygen supply and consumption play a vital role in mitochondrial energy production, and impairments may contribute to reduced oxidative capacity of mitochondria [3-5]. Impaired cellular energy production is shown to play a significant role in diseases such as Type II diabetes (T2DM), chronic obstructive pulmonary disease (COPD), heart failure (HF), peripheral artery disease (PAD), and Barth syndrome (BTHS) [6-13]. This leads to a decline in physical function and an increased risk for disability and mortality [14]. The development of non-invasive measurements of blood flow and oxygen extraction may elucidate valuable biomarkers in studies of organ dysfunction and disease propagation.

Arterial spin labeling (ASL) MRI techniques are widely used to magnetically label blood water as an endogenous tracer to measure perfusion in brain and other organs non-invasively. The exchange of blood water from the vascular circulation to the tissue through the capillary wall was initially

considered free and unrestricted; however, several studies have shown evidence of restricted water exchange [15-17]. The exchange of blood water between vascular space and tissue space is regulated primarily by the permeability of the capillary wall, which is composed of a single layer of endothelial cells [2]. Therefore, the endothelial function plays a vital role in regulating the exchange of water, oxygen, and other nutrients from the intravascular space to the tissue space.

The delivery of blood water from vascular space to the tissue space is affected primarily by two physiological processes: water filtration and water diffusion [18, 19]. While diffusion refers to the passage of water molecules across the capillary wall because of Brownian motion, filtration refers to the motion due to the osmotic pressure gradient. Slits and pores between endothelial cells play a major role in water filtration in capillaries outside the central nervous system (CNS) because bulk flow can take place across the capillary wall through these slits and pores. However, it has very little contribution to water diffusion because the total surface area of these pores and slits is very small compared to the total capillary surface area. The water channels (aquaporin) have a diameter on the order of a single water molecule in the CNS. Therefore, these channels only permit water diffusion but not water filtration in the CNS. While the ratio between the filtration and the diffusion is fifty or more outside the CNS (i.e. skeletal muscle), it is close to unity in the CNS. Thus, the exchange of water between vascular space and tissue space is more restricted in the CNS and regulated primarily by the blood-brain barrier (BBB) [15, 20-23].

Given that the BBB plays a fundamental role in regulating the exchange of nutrients between the vascular circulation and the CNS [24], it provides a suitable functional environment for the nervous system by restricting neurotoxins and macromolecules from entering the tissue[25]. Disturbance in the BBB can result in the altered functional activity of the CNS, which is associated with many pathological conditions such as multiple sclerosis (MS), Alzheimer's disease, Parkinson's disease,

tumors, and stroke[26-30]. In addition, the BBB prevents the brain uptake of most pharmaceuticals. However, novel approaches have demonstrated the potential to overcome this barrier and increase drug delivery in diseases like brain tumors, Parkinson's disease, and lysosomal storage [31-33]. The development of non-invasive techniques to measure BBB permeability is clinically relevant in investigating a variety of CNS diseases and to measure treatment response.

Proton (^{1}H) magnetic resonance spectroscopy (MRS) is a valuable tool to assess CNS diseases non-invasively [34]. In vivo chemical compounds such as ^{1}H metabolites represent specific biomarkers in the CNS; for example, the creatine (Cr) in the MR spectrum represents energy metabolism, the choline (Cho) represents cell membrane turnover, GABA represents inhibitory neurotransmission, etc.[35] Concentrations of these metabolites can be used to probe the biochemistry of the CNS and alterations in these metabolites may precede anatomical changes. The most widely used technique for MRS is single voxel spectroscopy, which can be useful if the disease is homogeneous, or the disease is focal and the region of interest (ROI) is known. However, most CNS diseases such as schizophrenia, Alzheimer's disease, frontotemporal dementia, etc. are heterogeneous in nature and necessitate the acquisition of spectral information at multiple spatial locations [36, 37]. MR spectroscopic imaging (MRSI) enables the acquisition of spatial and spectral information simultaneously. However, for traditional MRSI methods, which use only the phase encoding (PE) technique, the total acquisition time can be very lengthy as it samples a single k-space position per repetition time (TR) and makes it difficult for clinical applications. Techniques for simultaneous spatial-spectral encoding (SSE), such as rosette spectroscopic imaging (RSI) can accelerate the imaging time to a clinically feasible limit. Therefore, the development of such efficient MRSI techniques is critical for clinical applications.

The spinal cord (SC) is the linkage between the brain and the surrounding nervous system and plays a vital role in pathologies such as multiple sclerosis, cervical spondylotic myelopathy, amyotrophic lateral sclerosis, and neurodegenerative diseases [38-42]. MRI is routinely used for non-invasive diagnosis of SC pathology. However, the ability to detect early or subtle pathological features in SC pathology is limited by the spatial resolution, contrast to noise ratio (CNR), and physiological motion [43-45]. Routine Cartesian MRI of the SC is prone to image artifacts caused by physiological motion. Non-Cartesian acquisition techniques such as rosette can help reduce the artifacts caused by the physiological motion, as the rosette imaging technique is inherently insensitive to bulk motion [46-48]. The development of such non-Cartesian techniques for SC imaging with high spatial resolution, high SNR and CNR, and reduced motion artifacts can be very useful in clinical applications.

Improved non-invasive imaging techniques for quantitative evaluation of hemodynamics, endothelial function, and metabolites can be very beneficial in the early diagnosis of different CNS and musculoskeletal diseases. Therefore, the aim of this work was to develop efficient and improved non-invasive imaging techniques for the assessment of hemodynamic, endothelial, and metabolite information in the skeletal muscle and the CNS. The specific goals of this work were to demonstrate: (i) the feasibility and repeatability of a novel technique for the combined measurement of arterial blood flow, perfusion, venous oxygen saturation, and bioenergetics (^{31}P MRS) in the skeletal muscle, (ii) a novel non-contrast technique to measure perfusion and BBB permeability using magnetization transfer (MT) and arterial spin labeling (ASL) in the human brain, (iii) a robust technique for fast high-resolution ^{1}H MRSI of the human brain using non-Cartesian (rosette) trajectory, and (iv) a robust technique using motion-insensitive rosette trajectory for high-resolution human spinal cord imaging with MT weighting and the application

of compressed sensing. These techniques can improve the efficiency in providing hemodynamic, endothelial, and metabolic information, which can be very useful in the early diagnosis of a wide range of diseases.

Chapter 2

Combined Measurement of Arterial Blood Flow, Venous Oxygen Saturation, Muscle Perfusion, and Muscle Bioenergetics following Dynamic Exercise

2.1 Background

Impaired cellular energy production can play a vital role in muscle debility [49], which is a regular manifestation in a number of diseases such as COPD, heart failure, mitochondrial disease, Barth syndrome (BTHS), multiple sclerosis (MS) and Parkinson's disease (PD) [6-10]. Inadequate oxygen (O_2) supply and/or mitochondrial impairment can alter the production of cellular energy, which is essential for muscle function. Skeletal muscle O_2 extraction has been found to be closely related to mitochondrial function [10, 50, 51]. Assessment of O_2 supply and extraction, combined with muscle bioenergetics, can provide important information in understanding the biochemical mechanisms of muscle fatigue in pathological conditions.

Macro-vascular blood flow, microvascular blood flow (perfusion), and venous oxygen saturation (SvO_2) are tightly coupled, and together they may provide important information about deficits in skeletal muscle function. Blood flow within the macro-vasculature is related to the global transport of blood, O_2, and other nutrients. Perfusion is the delivery of blood, O_2, and other nutrients to the tissue space. Arterial and venous oxygen saturation measured together with blood flow can provide information about oxygen consumption according to Fick principle [52]. MRI allows non-invasive measurement of dynamic changes in these metabolic parameters. Real-time changes in macro-

vascular blood flow can be measured from velocity-encoded projections using the phase contrast [53-55] or complex difference method [56]. Perfusion can be quantified using saturation inversion recovery (SATIR)[57] arterial spin labeling (ASL) technique, a variant of flow alternative inversion recovery (FAIR) ASL method, and has been validated to determine muscle perfusion. Venous oxygen saturation (SvO_2) can be measured using multi-echo gradient recalled echo (GRE) data through susceptometry-based oximetry, which depends on the difference in magnetic susceptibility between deoxygenated intravascular blood and surrounding tissue [58, 59]. Studies have concluded that simultaneous measurement of muscle perfusion and SvO_2 during reactive hyperemia following a brief period of ischemia could successfully detect impaired vascular reactivity in patients with peripheral artery disease[60].

In addition, phosphorus magnetic resonance spectroscopy (^{31}P-MRS) is a well-established method to measure skeletal muscle biogenetics [61, 62]. The rate constant of post-exercise phosphocreatine (PCr) resynthesis is inversely proportional to the rate of oxygen consumption. It has been shown that post-exercise PCr recovery relies entirely on oxidative adenosine triphosphate production indicating that mitochondrial function of skeletal muscles can be determined from analysis of PCr recovery following muscular exercise [63]. While ^{31}P MRS has been widely applied for muscle oxidative capacity, relatively few studies have examined energetics, perfusion, and O_2 metabolism simultaneously in a single imaging session [64-66]. Combining ^{31}P MRS with muscle hemodynamics and O_2 metabolism offers an improved opportunity to observe the adaptation and capacity of working muscle. Recently, simultaneous interleaved acquisition of muscle perfusion by ^{1}H arterial spin labeling (ASL) MRI and energy metabolism (^{31}P MRS) in vivo has been demonstrated following dynamic exercise to study the recovery kinetics of muscle perfusion and oxidative ATP

production in the aging population[67]. Despite the importance of these approaches, the repeatability of these techniques has not been thoroughly investigated.

In this work, our aim was to determine the repeatability of real-time blood flow measurements and SvO_2 kinetics with moderate-intensity plantar flexion exercise. We chose the plantar flexion exercise since its dynamic contractions are a more accurate model of working muscle than isometric muscle contractions. In addition, the exercise of small muscle groups can help isolate local hemodynamic and energetic measurements from central system limitations and are more representative of the exercise capacity of an individual [68, 69]. The specific aims of the study were to demonstrate a modified pulse sequence that enables simultaneous rapid imaging of blood flow in the popliteal artery, SvO_2 in the popliteal vein, and relative perfusion (i.e., change from resting perfusion) in the calf muscle following plantar flexion stimulation and determine the repeatability of these parameters in healthy individuals. We also investigated the PCr recovery kinetics following the same exercise protocol and compared them to hemodynamic measurements. Finally, we demonstrated the clinical potential of our multi-parametric imaging with two Barth syndrome (BTHS) patients, a disease that affects mitochondrial function[7, 70]. Our primary hypothesis was that assessment of O_2 supply and extraction, combined with muscle bioenergetics, may provide a better understanding of the biochemical mechanisms of muscle fatigue in pathological conditions. The findings of this work have already been published [71].

2.2 Materials and Methods

2.2.1 Theory

Detailed theories to measure skeletal muscle perfusion using arterial spin labeling[57, 66], arterial blood flow using velocity encoded projections[55, 72, 73], and venous oxygen saturation using magnetic resonance susceptometry based oximetry[74-76] have been described in several studies. These theories with necessary modifications for this study are summarized below.

2.2.1.1 Perfusion imaging

Saturation inversion recovery (SATIR) is a variant of the classical FAIR ASL approach and has been validated previously for perfusion quantification in human leg muscles [57, 66, 67, 77]. A modification of the SATIR ASL approach was used in this study. SATIR requires the application of slice selective (tag, (M_{SS})) and non-selective (control, (M_{NS})) inversion pulses, followed by a post-labeling delay (PLD), to quantify perfusion in the unit of mL/100g/min. In order to improve the temporal resolution and enable adequate sampling of dynamic changes, only a slice selective inversion pulse was used in this study. With this limitation, only the change in perfusion (i.e. relative perfusion) from a baseline (i.e. resting perfusion value) can be determined instead of the actual perfusion. The theory is presented below.

With only the slice selective inversions, the signal intensities at rest and following exercise are given by [57]

$$M_{SS,rest} = M_0\left(1 - e^{-\left(r_1 + \frac{F_{rest}}{\lambda}\right)T}\right) \quad 2.1$$

$$M_{SS,exercise} = M_0\left(1 - e^{-\left(r_1 + \frac{F_{exercise}}{\lambda}\right)T}\right) \quad 2.2$$

Here, $M_{SS,rest}$ and $M_{SS,exrcise}$ are the measured signals with slice selective inversion at rest and following exercise respectively; F_{rest} and $F_{exercise}$ are the perfusions (mL/100g/min) at rest and following exercise respectively; λ is tissue partition coefficient (0.9 mL/g); relaxation rate constant r_1 = 0.7 s^{-1} at 3T [78]; and T is the post labeling delay (PLD). Optimal value for PLD should be ~ T_1 = 1.4s. However, a smaller value (~0.92 s) is chosen for better temporal sampling of dynamic changes [57, 60, 79].

Eq 2.1 and 2.2 can be rearranged to yield the relative perfusion ($\Delta F = F_{exercise} - F_{rest}$)

$$\Delta F = -\frac{\lambda}{T} ln\left(\frac{M_{SS,rest} - M_{SS,exercise}}{M_0 - M_{SS,rest}} + 1\right) \quad 2.3$$

Here, ΔF is the relative perfusion (i.e., change from resting value) in the unit of mL/100g/min. Measured total signal ($M_{SS,rest} + M_{SS,exercise}$) from Eq 2.1 and 2.2 can be written as

$$M_{SS,rest} + M_{SS,exercise} = M_0\left(2 - e^{-r_1 T}(e^{-\frac{F_{rest}}{\lambda}T} + e^{-\frac{F_{exercise}}{\lambda}T})\right) \quad 2.4$$

The term ($e^{-\frac{F_{rest}}{\lambda}T} + e^{-\frac{F_{exercise}}{\lambda}T}$) in Eq 2.4 is approximately constant (i.e., ranges from 1.98 – 1.99) for physiological range (5 – 100 mL/100g/min) of perfusion in exercising skeletal muscle and Eq 2.4 simplifies to

$$M_{SS,rest} + M_{SS,exercise} = M_0(2 - 2e^{-r_1 T}) \quad 2.5$$

With this approximation, Eq 2.3 can be reduced to

$$\Delta F = -\frac{\lambda}{T} ln\left(\frac{M_{SS,exercise} - M_{SS,rest}}{M_{SS,exercise} + M_{SS,rest}} 2(1 - e^{r_1 T}) + 1\right) \qquad 2.6$$

Eq 2.6 shows that, the relative perfusion (ΔF) can be calculated from slice selective labeling data only. The error in ΔF calculated using Eq 2.6 is on the order of 1% or less from the true ΔF value (Figure 2.1).

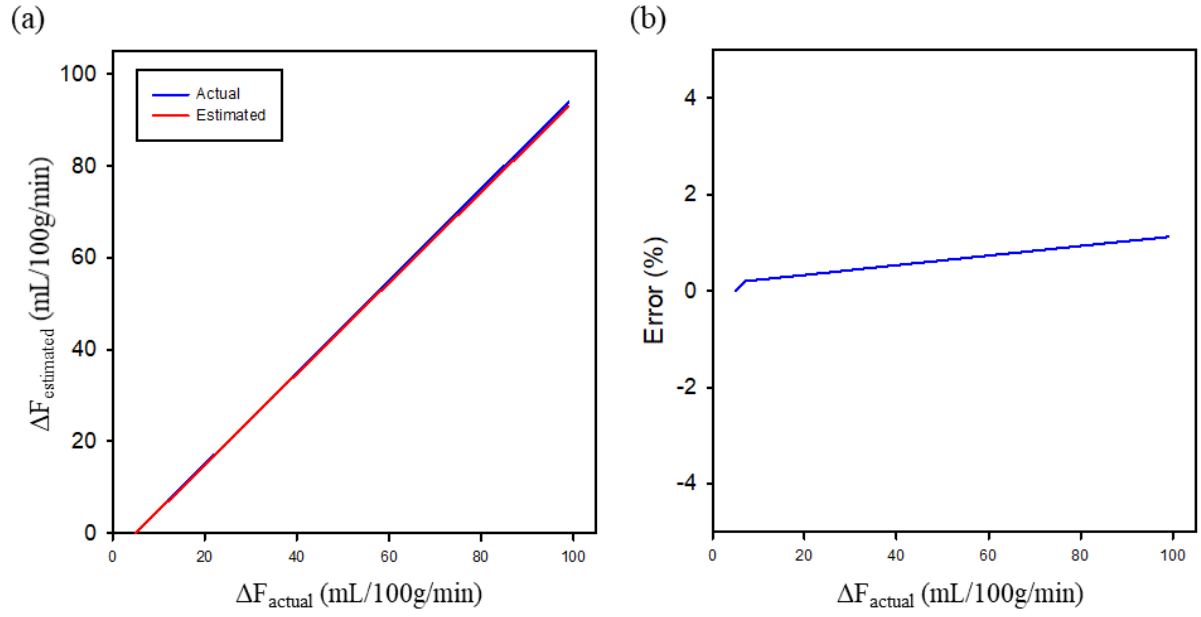

Figure 2.1: (a) Simulation showing the comparison between actual relative perfusion ($\Delta F = F_{exercise} - F_{rest}$, blue) calculated from slice selective (SS) and non-selective (NS) acquisitions, and estimated (red) ΔF based on theory developed in this in this study (Eq 2.6) using only the SS acquisitions. Input values for the simulation were r_1 = 0.7 s^{-1}, PLD=0.9 s, λ=0.9 mL/g. (b) Error (%) between actual and estimated relative perfusion is ~1% or less for the physiological range of perfusion values.

The relatively long PLD has been exploited in several studies to interleave additional pulse sequence modules for multi-parametric examination of skeletal muscle physiology, i.e., interleaved ^{31}P and ^{1}H ASL[64, 67, 80]; interleaved perfusion, venous oxygen saturation, T_2* and flow[60, 79, 81]. We incorporated a multi-echo GRE sequence during PLD to measure arterial blood flow and venous oxygen saturation simultaneously. A schematic of the pulse sequence is shown in Figure 2.2.

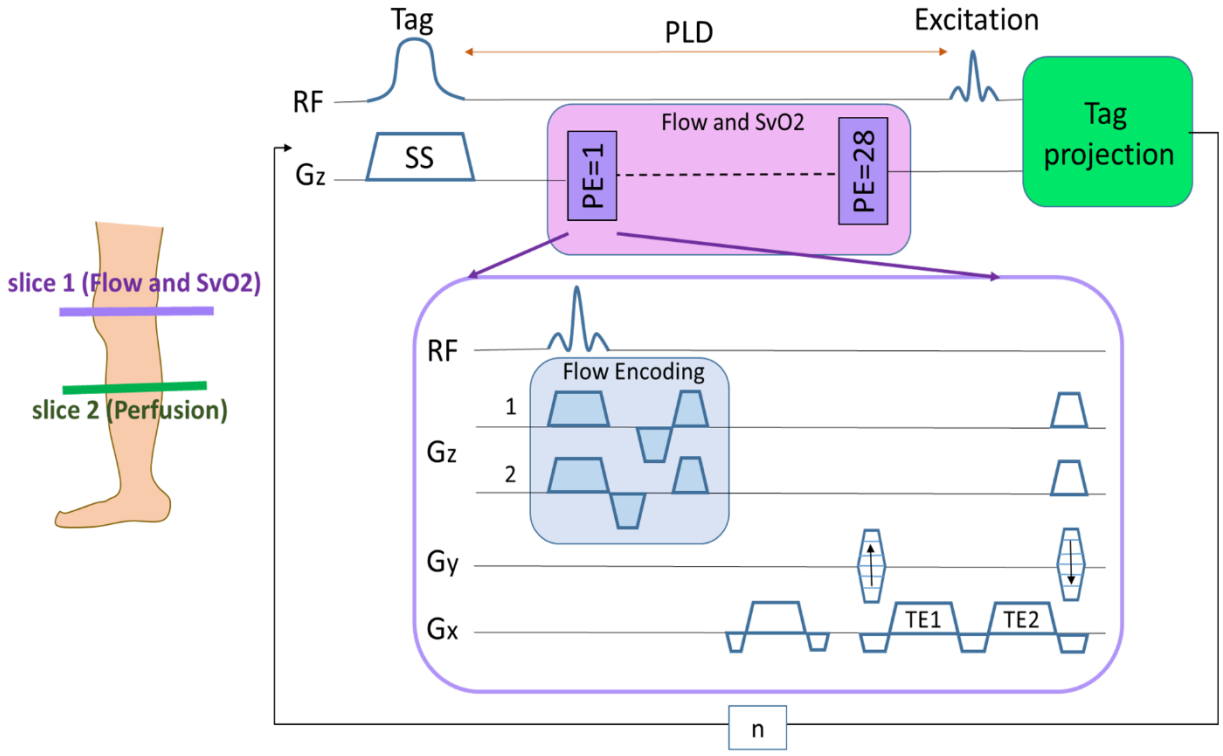

Figure 2.2: Schematic of the pulse sequence. Outer loop (top) represents the modified SATIR perfusion block: tagging – PLD – excitation and acquisition. All the gradients and ADC are not shown for clarity. Inner loop (pink) is multi-gradient echo pulse sequence for acquisition of bulk blood flow and SvO_2. First echo consists of flow encoded projections (no phase encoding) to measure flow. Phase encoding is turned on for 2nd and 3rd echoes for full 2D images used to

determine venous SvO_2. TR for inner block was 32 ms and 28 excitation, i.e., phase encodes (PE) can be acquired in PLD = 0.9 s. The combined interleaved sequence was looped for continuous data acquisition, i.e., baseline (1 min) – exercise (2 min) – recovery (~ 6 min) as described in the experimental protocol section.

2.2.1.2 Projection flow imaging

A velocity encoded projection method was used for real-time imaging of blood flow in the popliteal artery[55]. Phase-encoding gradients are turned off to yield a projection of the imaging slice. The velocity encoded and compensated projection images are acquired at sequential excitations. These images are subtracted to remove the signal from stationary tissue, hence isolating the flowing blood. The phase differences of the projection images are converted to velocity using standard relation between phase ($\Delta\emptyset$) and velocity (v) [54, 81].

$$v = \frac{VENC}{\pi}\Delta\emptyset \qquad 2.7$$

where v = blood velocity (cm/s), $\Delta\emptyset$ is the phase difference between two velocity encoded projections, and VENC (cm/s) is the velocity encoding factor chosen to avoid aliasing [54]. Velocity was converted to flow (ml/s) using the cross-sectional area of the artery. The projection velocity mapping technique was validated in a calibrated flow phantom (Figure 2.3).

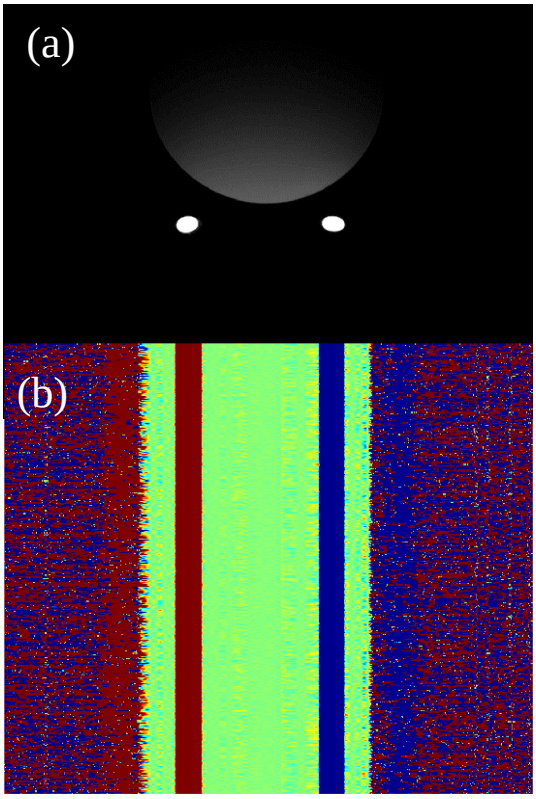

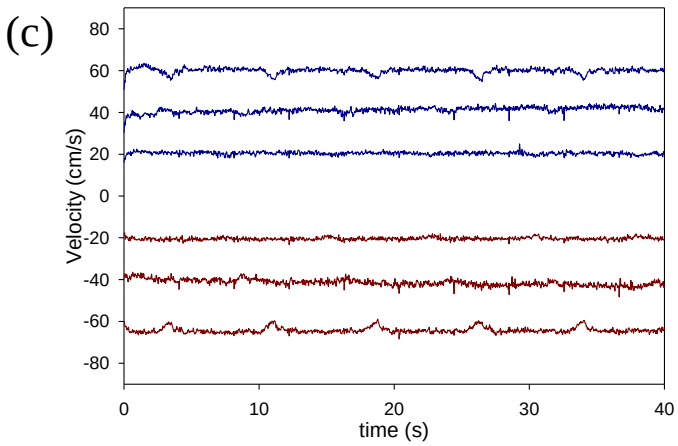

(d)

Expected Velocity (cm/s)	Measured Velocity (cm/s)
20	20.3±0.8
40	41.2±1.5
60	60.7±1.3

Figure 2.3: (a) Flow phantom. Static large load and two tubes with flowing water. The velocity was controlled with a calibrated water pump. The gradient in signal intensity is due to the sensitivity of surface coil placed below the phantom. (b) Time series of velocity projection images. The blue and red vertical stripes represent flow encoded phase difference images of the two tubes with flow in opposite directions. (c) Time series plot of velocity for three velocity settings. (d) Table showing that average velocity was quantified successfully with the projection method.

2.2.1.3 Venous oxygen saturation (SvO_2) imaging

Venous oxygen saturation (SvO_2) was determined using susceptometry-based oximetry, which relies on difference in magnetic susceptibility between deoxygenated intravascular blood and the surrounding muscle tissue (assumed to have susceptibility of fully oxygenated blood). The

susceptibility difference between venous blood and tissue results in a shift in the local magnetic field, which can be measured using phase difference ($\Delta\varphi$) of GRE images at different echo times (ΔTE). The phase difference is a function of the blood oxygen saturation (SvO_2) in the vein and the hematocrit (Hct). Using a long cylinder model for the vein, the oxygen saturation in the vein can be estimated in units of percent of oxygenated hemoglobin [81-83].

$$SvO_2(\%) = 100\left[1 - \frac{2\frac{\Delta\varphi}{\Delta TE}}{\gamma\chi_{do}HctB_o\left(cos^2\theta - \frac{1}{3}\right)}\right] \qquad 2.8$$

Where $\Delta\varphi$= phase difference of the two GRE images acquired at two echo times, γ= proton gyromagnetic ratio (42.576 MHz/T), ΔTE =difference of two echo times, χ_{do}= 4π×0.27 ppm [72, 84] is the susceptibility difference between deoxygenated and oxygenated red blood cells, Hct (hematocrit) = 0.43 [72] and θ is the vessel tilt angle with respect to main magnetic field. Pilot experiments confirmed that interleaved velocity projection imaging with dual echo GRE does not cause artifacts (Figure 2.4).

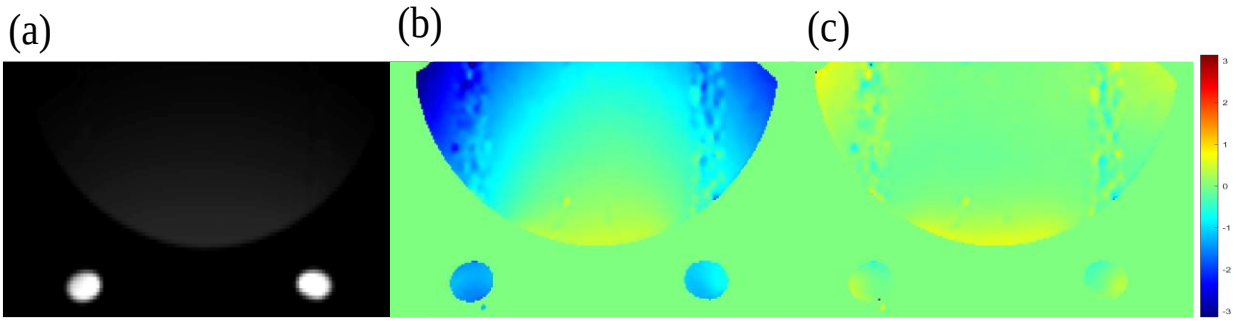

Figure 2.4: Double echo GRE for SvO_2 measurement. (a) Reference image. (b) Phase difference image of the phantom. (c) Field inhomogeneity is reduced by fitting to second order polynomial. It should be noted that static field inhomogeneity is expected to be more severe in phantom because

of the field gradients caused by the air phantom interface. Retrospective correction of magnetic field inhomogeneity is effective in reducing the effect of the background field on measuring SvO_2 using susceptibility-based oximetry.

2.2.2 Pulse sequence design

The schematic of pulse sequence is shown in Figure 2.2. The perfusion module consists of a slice selective inversion spin tagging pulse followed by post-labeling delay (PLD) (outer loop). The phase encoding was disabled giving a projection of the imaging slice (distal location) resulting in bulk perfusion estimate summed over the slice. Slice profile of the adiabatic blood tagging pulse was experimentally measured to confirm that it does not affect the bulk flow and SvO_2 measurements (Figure 2.5). A multi-echo GRE module (inner loop) was interleaved during PLD to measure flow and SvO_2 at proximal slice location (inner module, Figure 2.2). The phase encoding gradients are turned off for the first echo and velocity encoded projections of the imaging slice are obtained. The velocity encoding and compensation gradients are toggled every TR, and subtraction of the two resulting images allows the quantitative assessment of arterial velocity at a temporal resolution of $2 \times TR$. Phase encoding is enabled for the second and third echoes yielding 2D images for magnetic field mapping used for SvO_2 measurements. The temporal resolution for SvO_2 is equal to the number of phase encodes $\times$ TR.

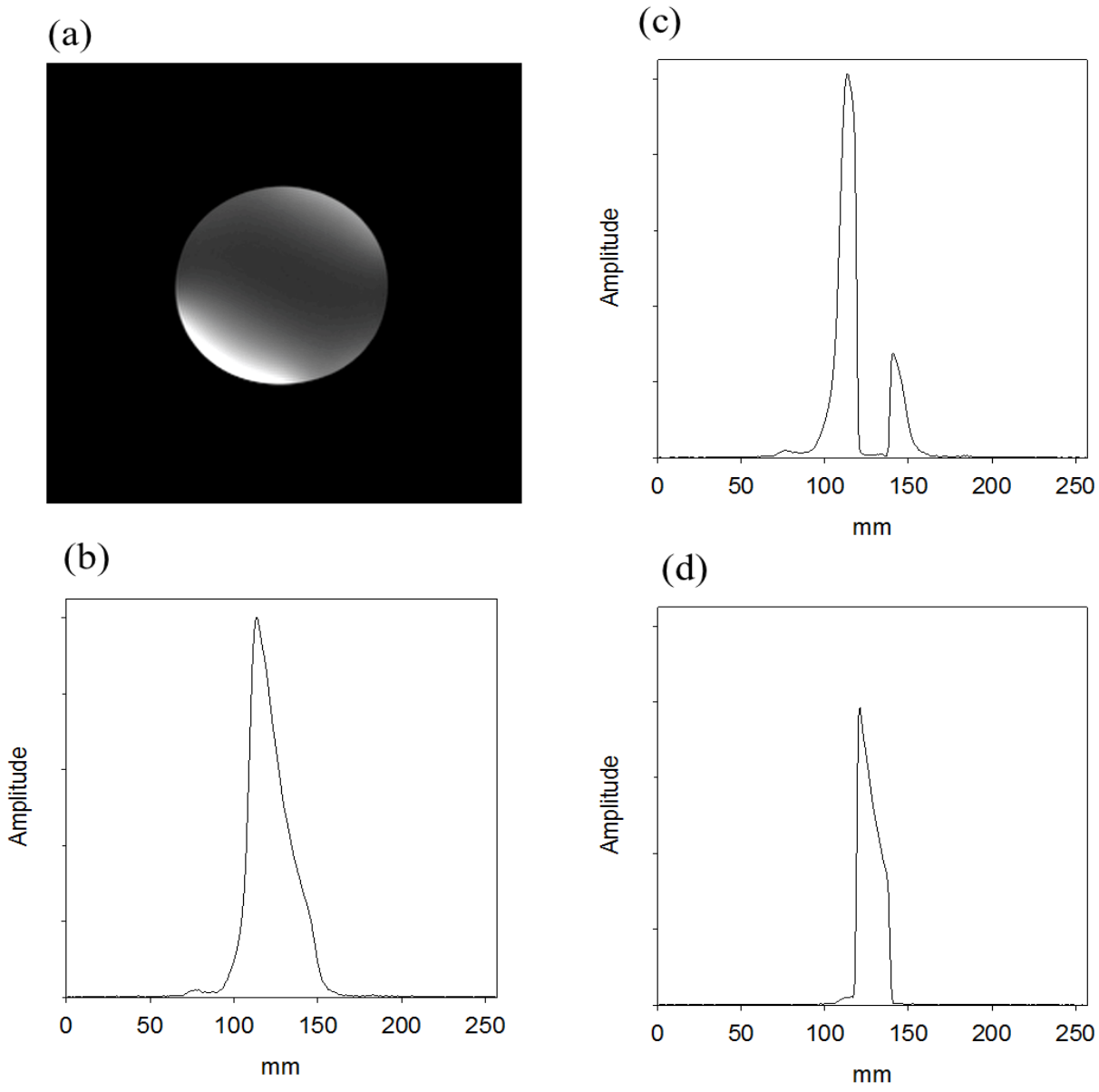

Figure 2.5: Experiment to determine slice profile of the adiabatic inversion pulse used for perfusion spin labeling. (a) Reference image of phantom. (b) 1D projection profile, i.e., phase encoding is turned off and data is acquired with non-selective excitation and in presence of readout gradient. (c) 1D profile acquired as average of two excitations with and without slice selective adiabatic inversion pulse. The sum of two acquisition eliminates the signal from the inverted slice location. Near zero signal demonstrates excellent efficiency of adiabatic inversion pulse. (d)

Profile of the adiabatic inversion pulse used in the experiment. Signal outside the selected slice is essentially zero indicating excellent localization of the adiabatic pulse.

2.2.3 Recruitment

The study was approved by the Washington University in St. Louis Human Studies Committee and all the subjects provided informed consent before participating in the study. Eight healthy subjects age = 38 ± 11 years, weight = 80 ± 10 kg participated in the study (5 male). Seven out of those eight subjects also participated in ^{31}P MRS study immediately after the ^{1}H hemodynamic scans. Inclusion criteria were normal range of motion (>20^{o}) for ankle joint flexion and no history of metabolic disease, heart failure, COPD, or neuromuscular disease. All subjects were non-smokers and were asked to refrain from alcohol or competitive exercise training 24 hours before the scan. In addition, two participants with BTHS (age=19 and 26 years, weight=67 and 89 kg respectively) also participated the study. All participants were right-handed and only the right leg was imaged. Siemens 3T Magnetom (Erlangen, Germany) with broadband capabilities was used for all the experiments.

2.2.4 Experimental protocol

2.2.4.1 Exercise design

Exercise consisted of unilateral plantar flexion against a force adjusted to 30 % MVIC using a pressurized pneumatic cylinder. MVIC was measured in a prior visit using a dedicated dynamometric ergometer (Biodex Medical Systems, Inc; Shirley, New York). During this visit, the participants were seated on dynamometer with the knee fully extended and supported by the chair. The pelvis and lower leg were secured with straps to avoid unnecessary movement. The foot

was placed in the dynamometer dorsiflexion (DF)/plantar flexion attachment with the ankle in the neutral position. The test consisted of three maximal isometric contractions sustained for 3 seconds. One minute rest was provided between successive contractions.

During the scanning visit, the volunteers were positioned supine on the MR table with their right foot firmly strapped to a pedal of a home-built plantar flexion exercise device compatible in MR environment (Figure 2.6). Velcro straps were fastened over the subject's leg to prevent the displacement of the leg relative to the MRI coil. After the initial familiarization period, the participants were given at least 10 min rest before the experiment protocol. During the exam protocol, each participant performed 30 plantar flexions at a cadence of 1 plantar flexion exercise every 2 sec. An audio click was provided to the participant and was used to maintain plantar flexion repetition rate during exercise. All subjects performed two repeated exercise bouts, separated by at least 10-min recovery period. Flow, SvO_2 and relative perfusion measurements were performed at rest, during plantar flexion, and at least 5 minutes during recovery from exercise.

At the completion of proton imaging the MRI table was pulled from the scanner, and a homebuilt $^{31}P/^{1}H$ surface coil with 8 cm diameter for the phosphorus coil replaced the body array coil. The subject was not removed from the table only the coils were switched. The subject performed the exact same exercise protocol for ^{31}P energetic measurements. Exercise performance was monitored using Digital Gauge and Transmitter (Ashcroft Industries, Stratford, CT) and USB-6009 Data Acquisition unit (National Instruments, Austin, TX).

Figure 2.6: Picture of home-made plantar flexion exercise device. (a) Velcro straps secure the subjects leg and foot to the device. Air pressure in the calibrated pneumatic cylinder provides the resistive force. Arrows point to the stops used to control the range of motion. (b) A groove under subject's leg secures the RF coil and prevents it from sliding.

2.2.4.2 Acquisition protocol

2.2.4.2.1 ^{1}H MRI acquisition

To visualize the anatomy, multi-slice gradient echo images were acquired at two locations (knee for flow and SvO_2 and calf for perfusion) with following acquisition parameters: 512 × 512 acquisition matrix, 192 × 192 mm^2 field of view, 5 mm slice thickness, TR/TE = 20/6.14 ms, 326 Hz/pixel receiver bandwidth, 20° flip angle. Typical location of two slices is shown in Figure 2.7. The proximal slice (SL-1) was used for velocity-encoded projections and dual echo GRE images; and the distal slice (SL-2) for perfusion measurements. Siemens whole body volume coil was used for transmit. and the surface body array coil placed longitudinally under the leg was used for signal reception. Longitudinal placement of the coil provides sufficient coverage to image both slices.

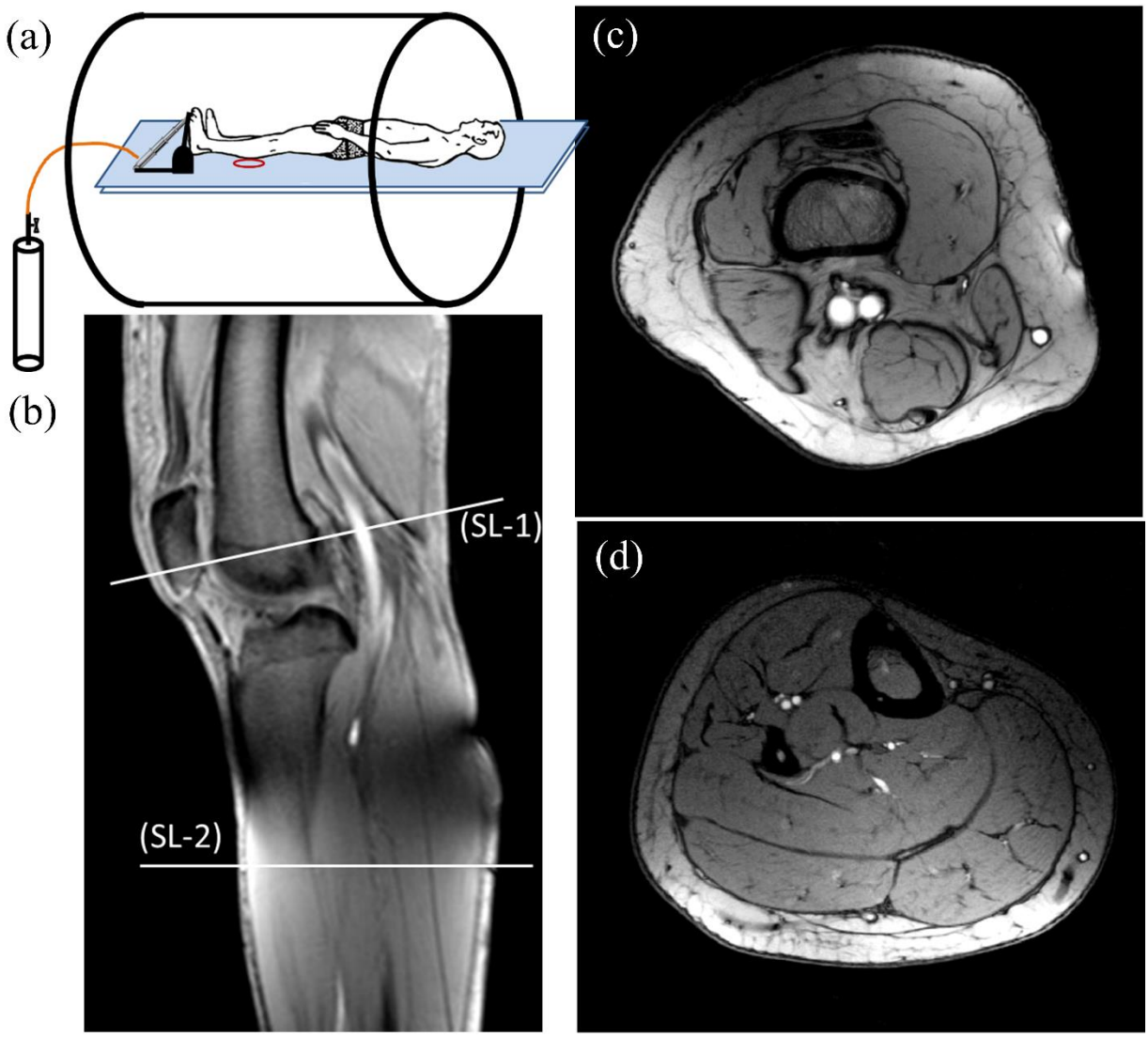

Figure 2.7: (a) Schematic of plantar flexion exercise setup in the scanner. The foot and leg are firmly secured to the exercise device. Resistance to exercise was provided by air pressure in the calibrated pneumatic cylinder. (b) Typical locations of the two slices used for interleaved data acquisition. (c) Representative slice for blood flow and SvO_2. (d) Slice for relative perfusion measurements.

The parameters for perfusion projection imaging were: 5 mm slice thickness, 256 acquisition matrix (phase encoding is disabled), 256 × 192 mm^2 FOV, 500 Hz/pixel bandwidth, flip angle =

20°. An 8.6 ms adiabatic hyperbolic secant inversion pulse was used for spin tagging. Only slice selective inversion pulses were used with tagging slice thickness = 2 × imaging slice thickness. Temporal resolution for perfusion projections was 0.92s (with PLD=0.9 s; and additional 20 ms for spoiling gradients and saturation pulses). Acquisition parameters for multi-echo GRE module interleaved in PLD for flow and susceptometry imaging were: 5 mm slice thickness, 256 × 192 acquisition matrix, 256 × 192 mm^2 FOV, 500 Hz/pixel bandwidth, flip angle = 20°. Repetition time (TR) for each excitation was 32 ms, echo times = 4.92, 9.84 and 14.76 ms, and v_{enc}= 150 cm/s. During each PLD, 28 phase encoding lines for GRE images were acquired.

2.2.4.2.2 ^{31}P MRS acquisition

Multi-slice proton MR localizers were initially acquired to determine the position of the leg with respect to the surface coil. Automatic localized shimming procedure was performed before ^{31}P data acquisition. MR data were acquired throughout the rest-exercise-recovery protocol with the following parameters: 2.56 ms adiabatic half passage excitation pulse, 2 s recovery time, 1024 data points, and 2.5 kHz spectral width. Fully relaxed (TR = 20 s, 4 averages) and partially saturated (TR = 2 s, 40 averages) spectra were acquired at rest to determine partial saturation correction factors.

2.2.5 Data analysis

2.2.5.1 ^{1}H MRI Analysis

Data analysis was performed offline with custom software written in MATLAB (MathWorks, Natick, MA). Relative perfusion (ΔF) throughout the rest-exercise-recovery protocol is calculated using Eq 2.6. The signals from first ten projections at rest were averaged and used as $M_{SS,rest}$.

Relative perfusion from each projection was averaged excluding 10 % of the projection from terminal sides. The time course of ΔF in general did not demonstrate exponential behavior; therefore, fitting it to mono-exponential decay was not justified and would convey little information. Cumulative ΔF area under the curve (AUC) was determined as marker of post exercise hyperemia [66].

Velocity was calculated from the phase difference of the velocity encoded and compensated projection images using Eq 2.7. The background static tissue signal was eliminated by fitting the static tissue signal to a 2nd order polynomial and interpolating the tissue signal for arterial region and subsequently subtracting the interpolated arterial static tissue signal from the arterial blood signal. The vessel boundaries and average vessel diameter were determined by averaging several phase difference images, which provide high contrast between vessels and static tissue. The diameter of the vessel was used to convert the velocity to blood flow rate in ml/s. The time-course (averaged over 10 cardiac cycles to eliminate pulsatile effects) for popliteal artery blood flow was used to evaluate post-exercise recovery time constant modeled as a single exponential. The blood flow in the vein was not calculated because VENC was chosen to avoid aliasing due to high post-exercise arterial blood velocity and far exceeds the blood velocity in the vein.

SvO_2 was calculated from the phase difference of the GRE images acquired at two different echo times. After unwrapping, the static field inhomogeneity was determined by fitting the phase difference image to a second-order polynomial surface in a ROI surrounding but excluding the blood vessels as described before[82]. This static field inhomogeneity was subtracted from the unwrapped phase difference image, and SvO_2 was calculated using Eq 2.8. Post-exercise SvO_2 recovery time constant was calculated by fitting the recovery SvO_2 to a mono-exponential curve.

2.2.5.2 ^{31}P MRS Analysis

Processing of ^{31}P MRS spectra was done using jMRUI (Java-Based Magnetic Resonance User Interface) software [85]. Nonlinear least-squares algorithm (AMARES) was used to fit the spectra in the time domain using known ^{31}P resonance frequencies and J-couplings as described before [62, 86-88]. Adenosine triphosphate (ATP), phosphodiesterase (PDE), PCr and inorganic phosphate (Pi) were fitted to Lorentzian line shapes. PCr and Pi absolute concentration was calculated assuming resting [ATP] = 8.2 mmol/L [62, 89]. Post-exercise PCr recovery was fitted to single exponential curve to measure recovery time constant τPCr [62]:

$$PCr(t) = \Delta PCr\left(1 - e^{\frac{-t}{\tau PCr}}\right) + PCr_{end} \qquad 2.9$$

where $PCrend$ is the PCr concentration at the end of the exercise and $\Delta PCr = [PCr]_{rest} - PCr_{end}$. Initial PCr recovery rate V_{iPCr} was calculated using [62]

$$V_{iPCr} = \frac{\Delta PCr}{\tau PCr} \qquad 2.10$$

Maximal oxidative flux Q_{max} was calculated using [62, 63]

$$Q_{max} = \frac{[PCr]}{\tau PCr} \qquad 2.11$$

2.2.6 Statistical analysis

Test–retest repeatability was measured by repeating the exercise and imaging protocol with at least a 10-minute rest interval. Coefficient of variation (CV) was used to determine repeatability, i.e.,

to determine the degree to which repeated measurements vary for individuals[90]. Bland-Altman analyses and average intraclass correlation coefficient (ICC) were used to assess the agreement of measured parameters at rest, immediately post exercise, and time constants of recovery between the two trials[90, 91]. All data are reported as mean ± standard deviation.

2.3 Results

Typical locations for slices and representative axial images are shown in Figure 2.7. The proximal slice (SL-1) shows typical view of the popliteal artery and vein, and the distal slice (SL-2) shows location of relative perfusion and ^{31}P acquisition.

2.3.1 Relative perfusion (ΔF)

Figure 2.8b shows representative real-time relative perfusion weighted projections acquired during rest-exercise-recovery protocol and time course of ΔF averaged over the slice (Figure 2.8c). ΔF increased to 51.83±15.00 mL/100g/min immediately following cessation of plantar flexion exercise. Post exercise hyperemia (AUC) was 88.45 ± 35.75 mL/100g/min. The results are summarized in Table 2.1. ΔF during the exercise was not determined due to excessive movement.

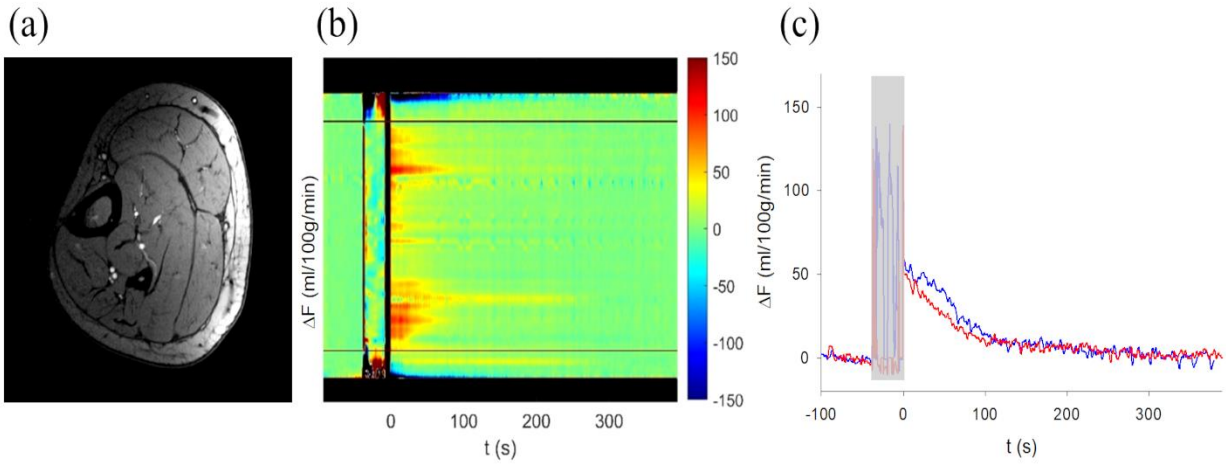

Figure 2.8: (a) Scout image at the location of leg where perfusion projections were acquired. The image is rotated for 90° to correspond to the projections. (b) Time series of projections showing the relative change in perfusion. The signal between the two horizontal lines was integrated to generate the relative perfusion (ΔF) time series plots. (c) Relative perfusion time course plot. Blue and red plots indicate test-retest repeatability.

Table 2.1: Arterial blood flow (popliteal artery), venous oxygen saturation (popliteal vein) and relative perfusion (calf muscle, peak and area under the curve (AUC)) values (mean±SD) from all subjects for 1st and 2nd measurements with intra-class correlation coefficient (ICC), coefficient of variation (%CV), and correlation coefficient (R).

		Measurement				
		1st	2nd	ICC	% CV (range)	R
Flow (mL/s)	Rest	1.71 ± 0.56	1.87 ± 0.63	0.8	11.9 (0.7 – 23.6)	0.81
	Post Exercise	11.18 ± 3.17	11.28 ± 3.29	0.95	8.3 (1.04 – 18.2)	0.89
	Time Constant	36.74 ± 6.02	39.32 ± 7.9	0.86	6.7 (1.4 – 15.9)	0.82
	Rest	69.44 ± 4.20	71.48 ± 5.33	0.89	4.48 (0.2 – 9.6)	0.90

SvO_2 (%)	Post Exercise	45.23 ± 6.24	46.62 ± 7.1	0.92	2.23 (0.2 – 5.7)	0.87
	Time Constant	67.65 ± 14.18	74.7 ± 14.92	0.88	8.72 (1.7 – 15.6)	0.88
ΔF **(mL/100g/min)**	Post Exercise	52.81 ± 15.96	50.84 ± 15.0	0.86	13.5 (0.7 – 42.2)	0.73
	AUC	85.82 ± 28.79	91.08 ± 42.7	0.88	19.5 (7.3 – 43.6)	0.83

SvO_2 =venous oxygen saturation, AUC=area under the curve, ΔF=relative perfusion.

2.3.2 Flow

A representative data set for flow imaging is shown in Figure 2.9. The time series of phase difference images between velocity encoded projections (Figure 2.9b) was used to calculate the time course of velocity and flow (Figure 2.9c and 2.9d). At rest, blood flow in popliteal artery for the healthy individuals was 1.79 ± 0.58 mL/s and increased to 11.18±3.02 mL/s immediately after the cessation of exercise. The blood flow recovered to resting value with time constant of 38.03 ± 6.91 s. The results are summarized in Table 2.1.

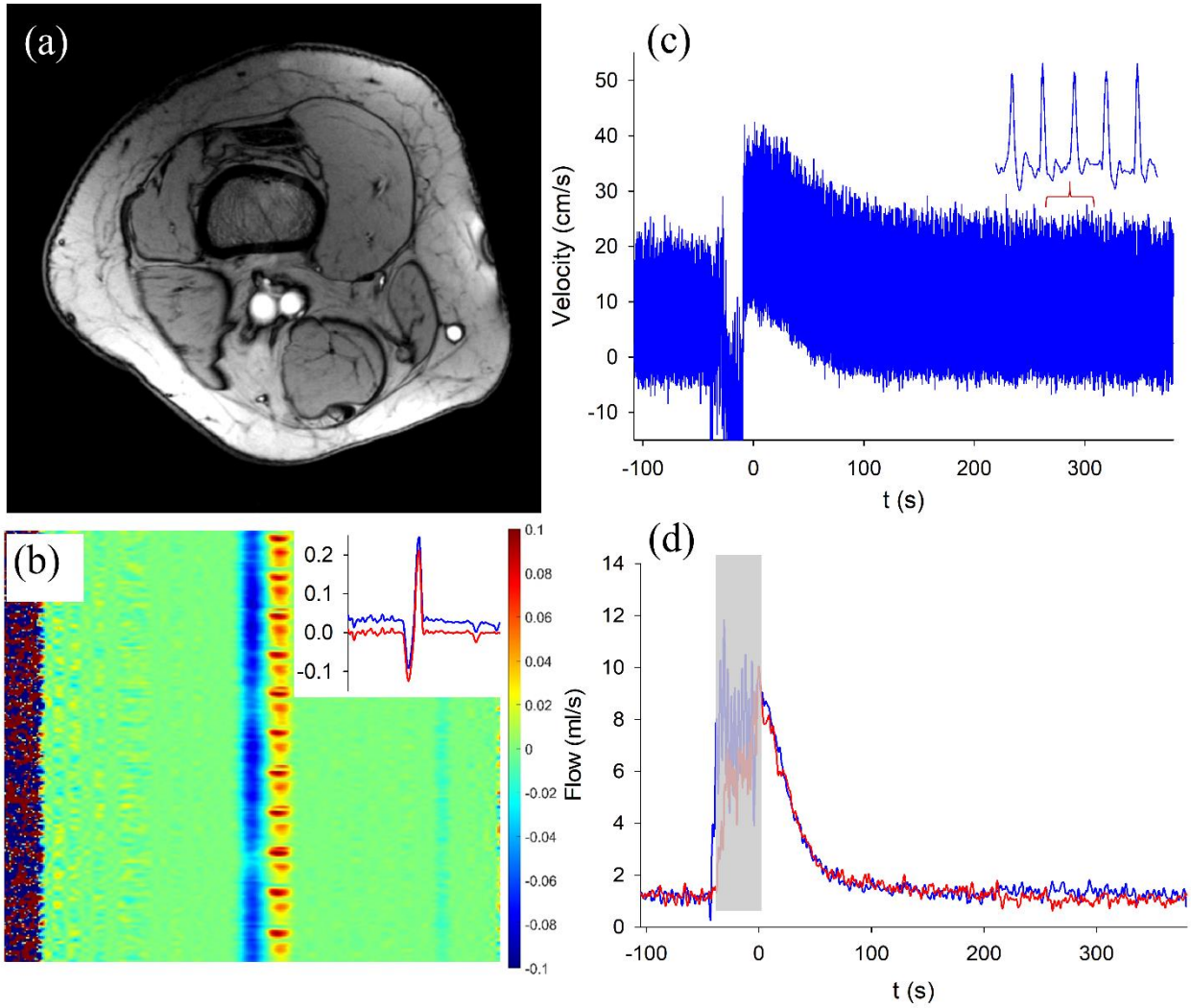

Figure 2.9: (a) Scout image of the slice for blood flow quantification. (b) Time series of velocity projection. Each horizontal row is one projection, and the vertical axis is the time series. Blue and red vertical bars are the velocity encoded phase for the popliteal vein and artery. Inset is the phase difference plot of one projection before (blue) and after (red) static tissue signal removal. (c) Time course of blood velocity in the artery with magnified view showing tri-phasic flow waveform in the inset caused by heartbeats. (d) Blood flow was calculated by converting time-average velocity over several heartbeats into ml/s using the diameter of the popliteal artery; where blue and red

plots indicate test-retest repeatability. The shaded region indicates exercise period and was not included in data analysis due to motion artifacts.

2.3.3 SvO_2

Figure 2.10 shows a sample magnitude image (Figure 2.10a); phase difference images, before (Figure 2.10b) and after (Figure 2.10c) background field correction; and time course of the popliteal vein SvO_2 (Figure 2.10d). The phase contrast between the artery and vein is due to susceptibility between oxygenated and de-oxygenated blood. SvO_2 at rest was 70.46±4.76 % and decreased to 45.93±6.5 % immediately after the cessation of exercise. It recovered to resting value with time constant 71.19±14.53 s (Table 2.1).

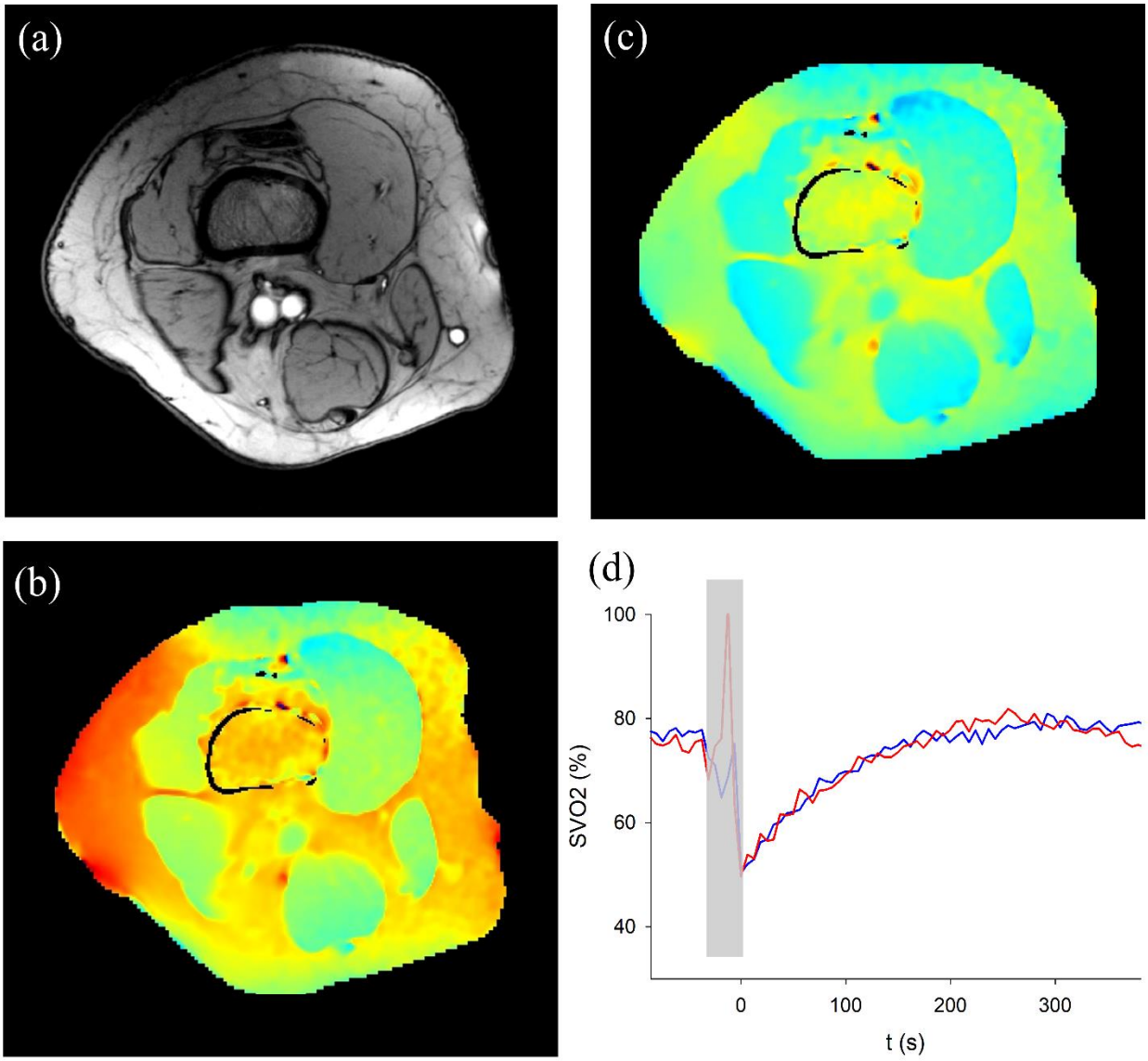

Figure 2.10: Illustration of the susceptometry-based oximetry imaging. (a) High-resolution scout image of SvO_2 slice. (b) Field map for SvO_2 quantification before field inhomogeneity correction. (c) Field map after field inhomogeneity correction that was used to calculate SvO_2. (d) Time course of SvO_2 in the popliteal vein where blue and red plots indicate test-retest repeatability at temporal resolution of ~ 6.5 sec.

2.3.4 ^{31}P Energetics

Typical ^{31}P MRS spectra are shown in Figure 2.11. PCr and Pi concentration at rest were 34 ± 2.4 mM and 2.8±0.6 mM respectively. Average τPCr was 34.5±7.5 s, V_{iPCr} = 0.36±0.11 mM/s and Q_{max} = 1.01±0.18 mM/s and are all within range of healthy individuals.

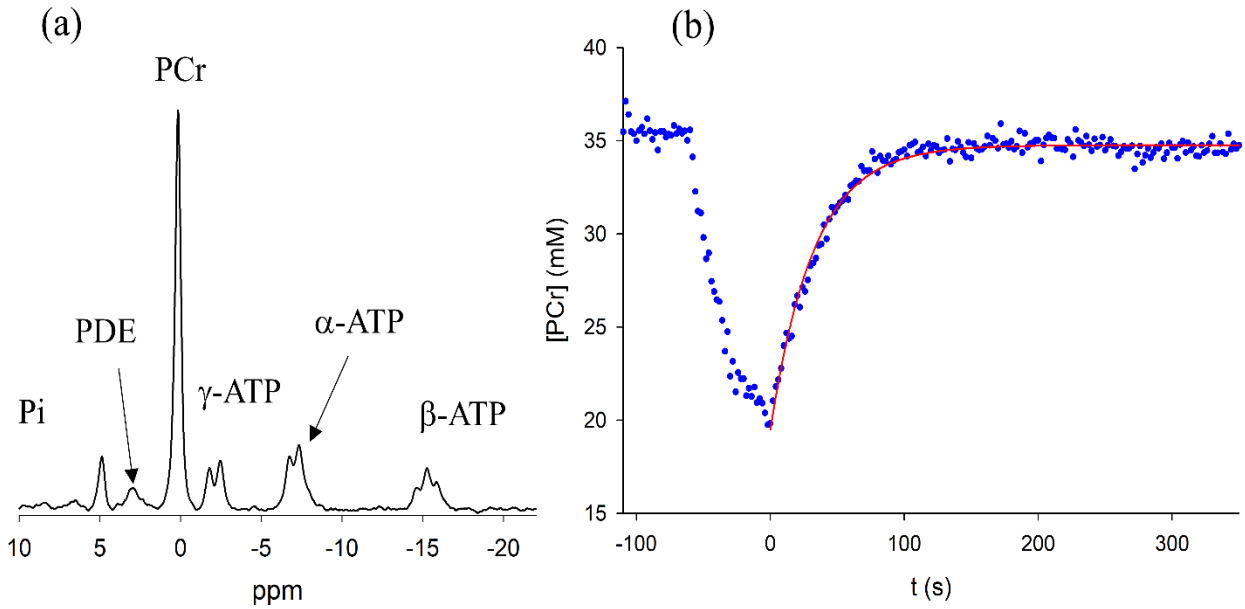

Figure 2.11: (a) Typical ^{31}P MR spectrum from a healthy control detailing the peaks of inorganic phosphates (Pi), phosphodiesters (PDE), phosphocreatine (PCr) and three adenosine triphosphate (γ-, α-, β-ATP). (b) Representative PCr magnitude from healthy control showing exponential fit.

2.3.5 BTHS Patient results

Clinical importance of multi-parametric mapping was demonstrated in two Barth syndrome subjects (Figure 2.12). Flow and relative perfusion displayed similar characteristics between healthy individuals and Barth patients. PCr recovery was significantly slower in Barth patients with τPCr = 92.5±23.6 s and Q_{max} = 0.41±0.13 mM/s, indicating severely impaired mitochondrial oxidative capacity. Resting SvO_2 was similar between patients and healthy controls; however, post

exercise results indicate higher SvO_2 (i.e. reduced oxygen extraction) and faster recovery (time constant ~ 20 s) in patients.

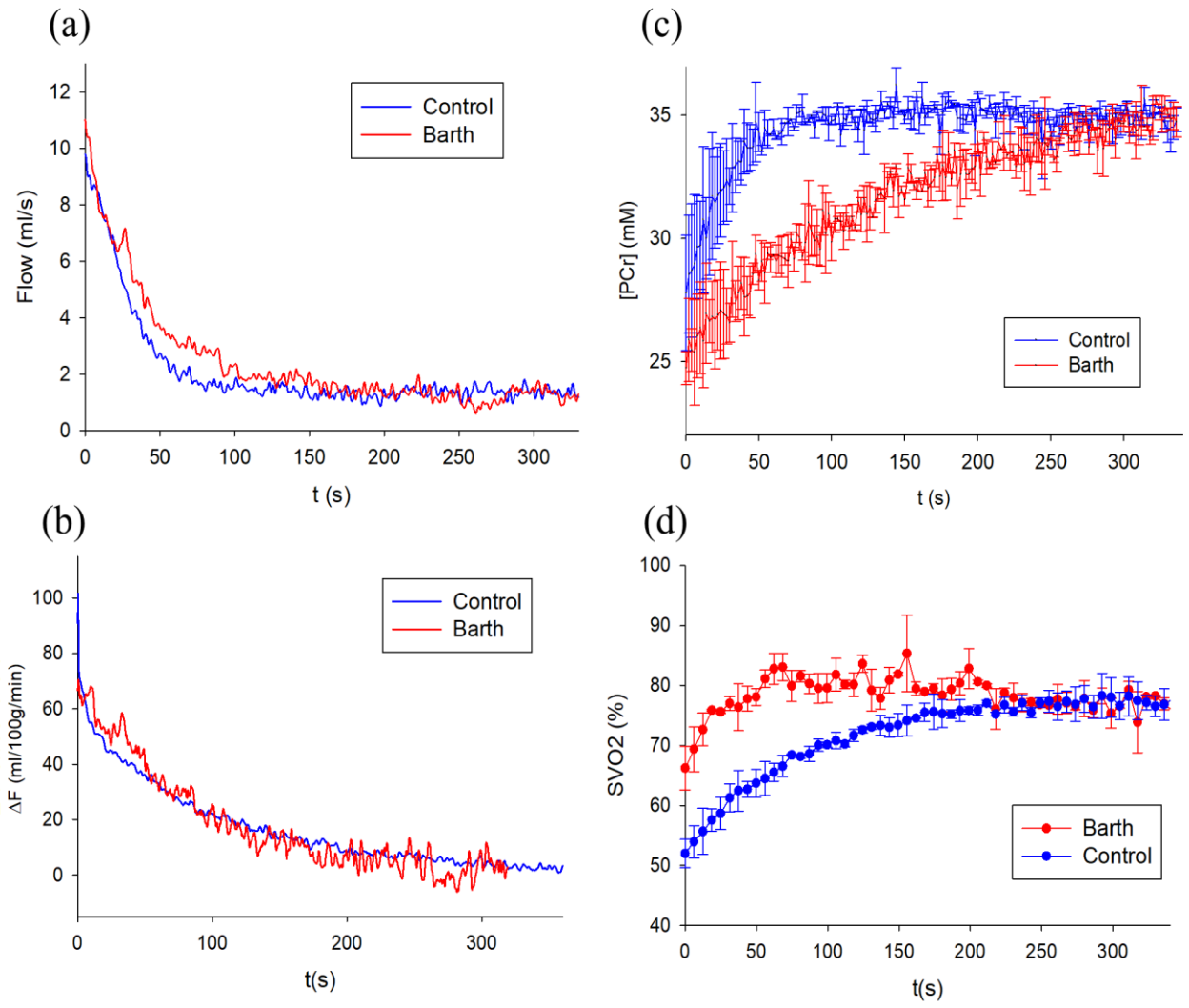

Figure 2.12: Comparison of recovery curves between healthy controls and BTHS patients following plantar flexion exercise. (a) Blood flow in the popliteal artery and (b) lower leg relative perfusion kinetics are similar between the two groups. Error bars are not displayed for clarity. (c) Kinetics of PCr signal intensity in Barth patients (red) are significantly slower than controls. (d)

SvO_2 drops in both groups immediately after exercise; however, SvO_2 drop in patients is much lower (low oxygen extraction from blood), and recovery is faster than controls.

2.3.6 Repeatability of measured variables

Figure 2.13 shows the Bland-Altman plots for different measured parameters: flow and SvO_2 at rest, immediately after the exercise and recovery time constant of flow and SvO_2. Figure 2.14 shows the Bland-Altman plot for relative perfusion. Bland-Altman plots demonstrate random variation across the sampling range, albeit with small bias. The mean differences were 0.04 for blood flow at rest, 1.179 for flow after exercise, 2.585 for flow recovery time constant, 1.394 for SvO_2 at rest, 0.4475 for SvO_2 after exercise and 3.004 for SvO_2 recovery time constant. Mean differences for post-exercise ΔF and area under the curve (AUC) were 1.572 and 14.05 respectively. In all cases, the line of zero bias was within the limits of agreement.

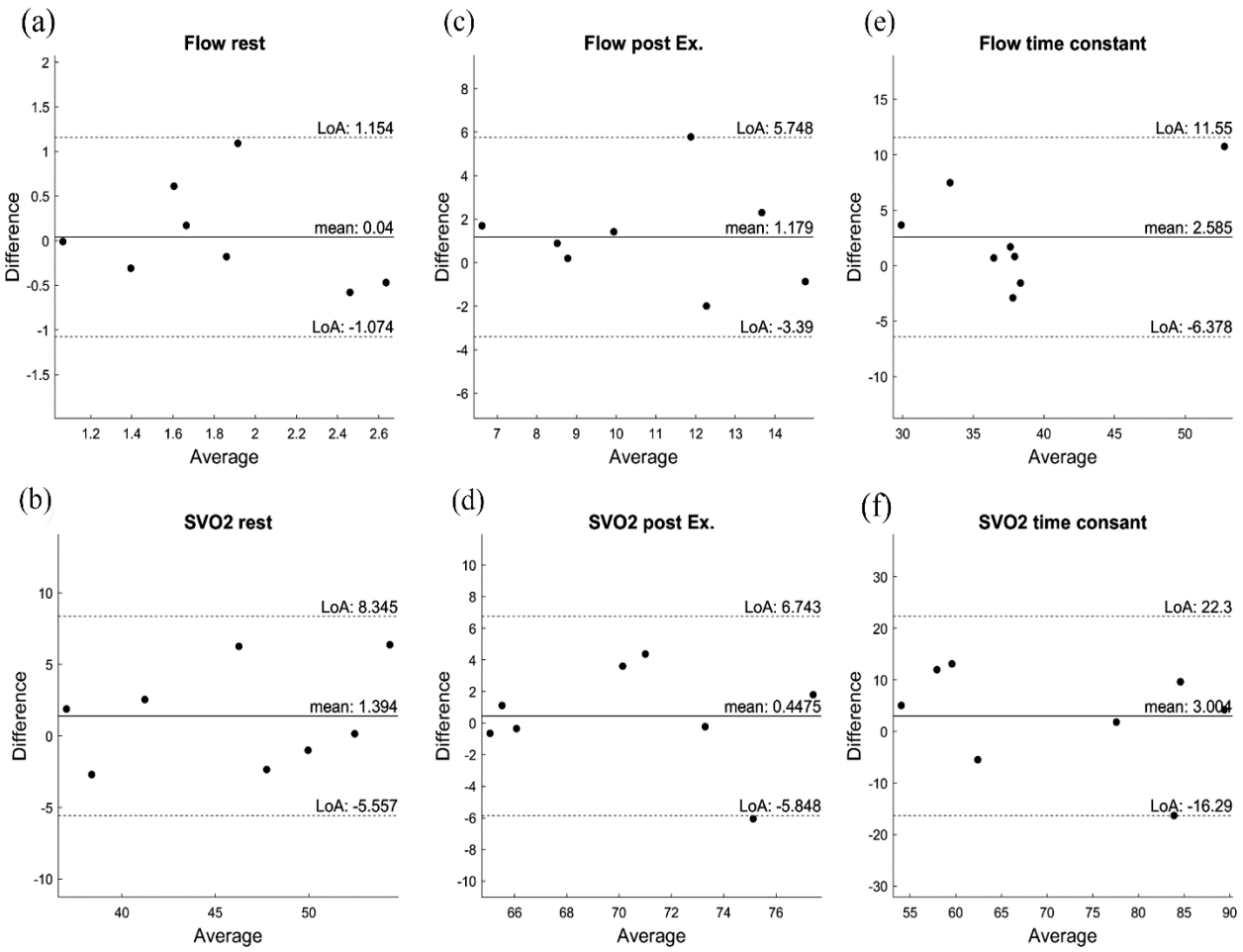

Figure 2.13: Test–retest Bland–Altman plots for flow and SvO_2 at rest (a, b), immediately following exercise (c, d), and time constant of recovery from exercise (e, f).

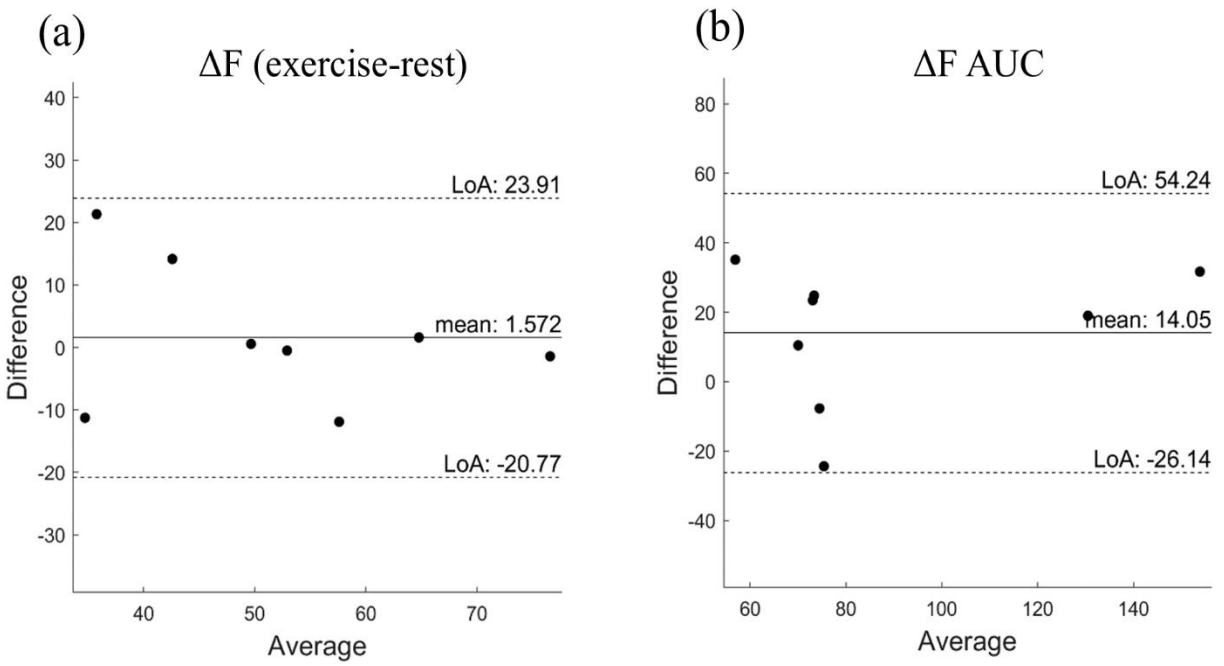

Figure 2.14: Test–retest Bland–Altman plots for relative perfusion following exercise (a) and area under the curve (AUC) during recovery (b).

Repeatability statistics (ICC, % CV, and correlation) for all variables measured are presented in Table 2.1. Relative repeatability of the hemodynamic variables measured by ICC ranged between 0.8 and 0.95 (lowest for resting flow). CV ranged from 2.23% to 19.5% with maximum CV for post-exercise AUC. Correlation plots (Figure 2.15) demonstrate very good linear relationship between test-retest for all measured variables and R ranged from 0.73 to 0.90.

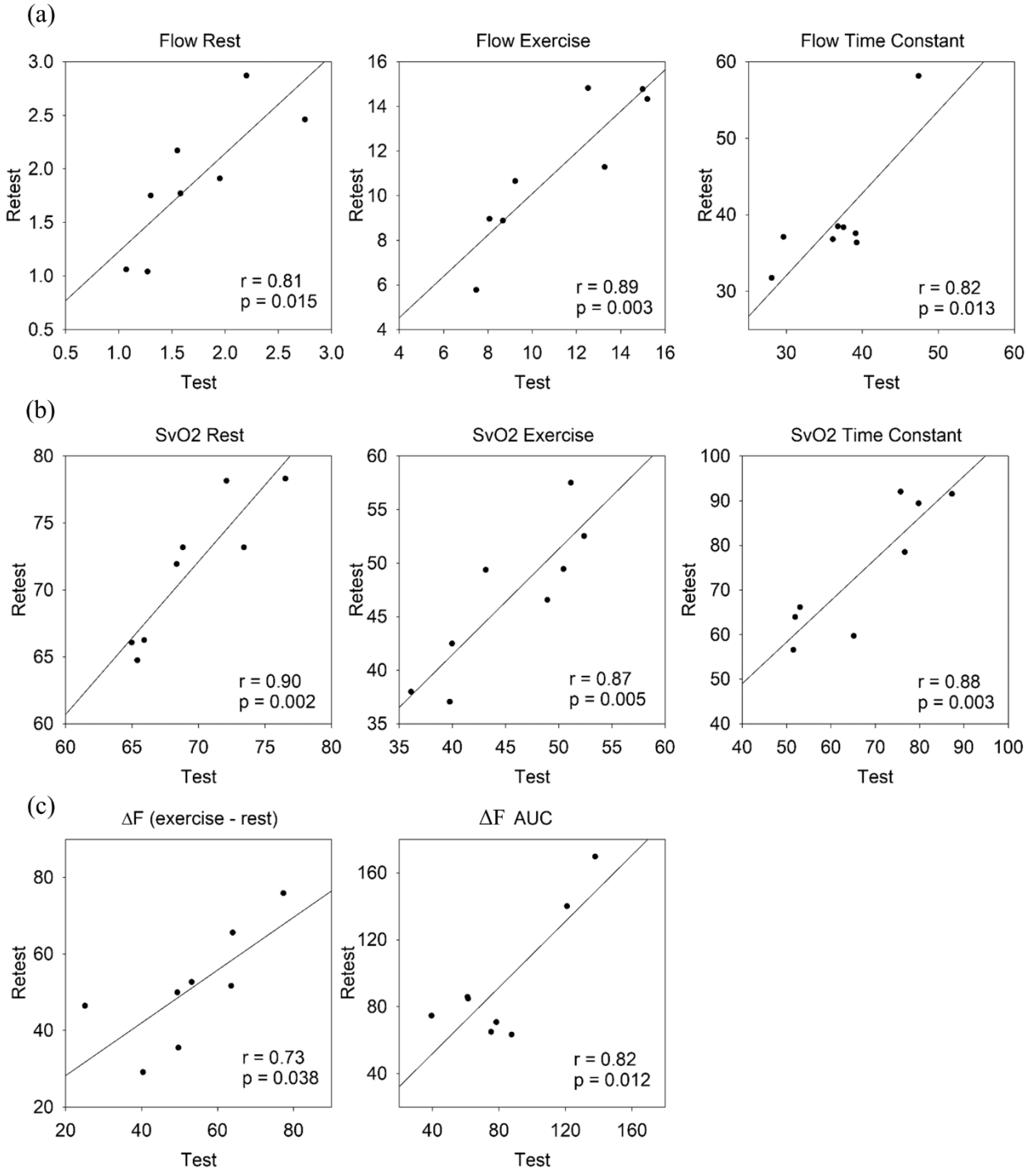

Figure 2.15: Test–retest correlations for all parameters: blood flow (a), venous oxygen saturation (SvO_2) (b), and relative perfusion (c).

2.4 Discussion

In this study, we addressed four things: 1) presented a theory to measure the relative perfusion (i.e., change from the resting perfusion) from the slice selective ASL acquisitions only; 2) demonstrated a pulse sequence for simultaneous time-resolved measurement of bulk arterial blood flow, venous oxygen saturation, and microvascular perfusion in activated muscle; 3) evaluated the repeatability of the measured parameters, and 4) measured bioenergetics parameters in the same study session under similar conditions. The sequence was designed such that temporal resolution enabled us to assess dynamic changes in blood flow, SvO_2, and relative perfusion following standardized exercise protocol. In addition, we demonstrate the importance of multi-parametric imaging of skeletal muscle in Barth syndrome, which affects mitochondria. Although several correlations can be determined from the measured data, we would like to emphasize that the purpose of this study is to demonstrate an easily implementable and repeatable protocol to measure these metabolic parameters. This study was not designed to determine physiological insights into flow, oxygen consumption, and energetics, which would require additional potentially invasive tests. The results illustrated in Table 2.1 and Figure 2.13, 2.14, and 2.15 demonstrate a high test–retest repeatability, signifying that the experimental procedures and acquisition protocol are feasible for larger research studies.

The repeatability measures of real-time muscle hemodynamic parameters have been scarcely investigated. Only two studies have investigated the repeatability of blood flow and SvO_2 in the femoral vein in conjunction with dynamic knee extensor exercise[72] and perfusion in the calf muscle with plantar flexion exercise[92]. The repeatability of simultaneous measurement of arterial blood flow, venous oxygen saturation, and muscle perfusion after dynamic plantar flexion exercise and its relationship to near simultaneous measurement of phosphocreatine (PCr) kinetics have never

been experimentally determined. This is the first report to demonstrate the repeatability of multi-parametric simultaneous measurement of several hemodynamics parameters in the calf muscle in response to plantar flexion. Calf muscle was chosen in this study because it is commonly preferred for ^{31}P bioenergetics studies and convenient for the subjects. Small muscle exercise also isolates the contributions from cardiac limitations and enables targeted skeletal muscle metabolic studies. Repeatability of ^{31}P parameters has been a topic of research in a large number of studies and, therefore, was not addressed in this study [93-96].

Exercise increased the macro-vascular blood flow and relative perfusion, while decreasing SvO_2 in exercise-stimulated lower leg region. Blood flow increased to 11.18 ± 3.02 mL/s from a resting value of 1.79 ± 0.58 ml/s, i.e., ~6 times over baseline in the popliteal artery in response to exercise. Prior studies with similar lower leg exercises reported a peak blood flow of approximately 5-37 mL/s from a baseline of approximately 1.33-5 mL/s [72, 81, 97]. Venous oxygen saturation dropped by ~35% as active muscle extracts O_2 from blood for metabolic needs. Comparison of the present metabolic changes with existing data is complicated due to differences in the muscle stimulation protocol, studies in different muscle groups, and subject characteristics. Nonetheless, the results presented here are within physiological range and comparable with the values reported in the literature [72, 81].

Table 2.1 and Figure 2.13, 2.14, and 2.15 show good test–retest repeatability in flow, SvO_2 and ΔF measurements. Poorest repeatability was seen in resting blood flow. High VENC (150 cm/s) was chosen to avoid the aliasing of velocity-dependent phase changes in peak blood velocity post exercise. This VENC is not optimal to measure blood velocity at rest, leading to low SNR, and might contribute to poor repeatability of resting flow.

ASL is used widely in skeletal muscle research with spatially and temporally resolved resolutions, and mismatch between perfusion and metabolism may lead to muscle dysfunction[66, 98]. High temporal resolution and excellent SNR is mandatory to characterize post-exercise perfusion time course. To improve the temporal resolution and for adequate sampling of the exercise-related changes in perfusion, we measured the relative perfusion with the slice selective acquisitions only. This approach can be very useful in such dynamic studies, and the error introduced by the proposed technique is expected to be <1% for the physiological range of perfusion values. To achieve the high temporal resolution and SNR reported in the present study, we also used projection imaging. This is a major limitation of the current study since post-exercise perfusion is expected to be heterogeneous with differences in the temporal response between different muscle groups. We admit that due to lack of specificity of the signal from metabolically active muscles, it would be difficult to draw conclusions about physiologically relevant information in these perfusion studies. Future sequence design could address this issue by replacing the projections with fast acquisition techniques to get full 2D images.

We found that exponential fit was not suitable to model post-exercise recovery of the perfusion signal and the time constant of such a model fit would convey no information. We measured post-exercise cumulative area under the curve (AUC, arbitrary units) for 5 minutes following the end of exercise. Previously AUC parameter has been successfully used to demonstrate diminished perfusion in the elderly population when compared to young [66]. In our study, the relative perfusion increased to ~52 mL/100g/min immediately after the exercise. Prior studies with similar kinds of exercise stimulation reported a peak value of perfusion in the range of 43-84 mL/100g/min [66, 79, 81, 92]. Both end-exercise peak relative perfusion and AUC demonstrate excellent repeatability (ICC > 0.85). RF excitation of the proximal slice (slice 1, Figure 2.2) might cause slight imperfection in

the perfusion weighting when some of the tagged blood spins from this proximal slice are delivered to the distal slice (slice 2, Figure 2.2). This effect is difficult to quantify without additional experiments. However, this bias would result in a slight underestimation of the perfusion and should have a minor impact on the results. A previous study has shown that near simultaneous excitation of adjacent slices does not appreciably affect the perfusion measurement [81].

Select few studies have explored perfusion and ^{31}P energetic studies in skeletal muscle simultaneously or in a single session[64-67]. We demonstrated that multi-parametric (i.e., bulk flow, SvO_2, relative perfusion (ΔF), and ^{31}P energetics) measurements in clinically feasible scan time (i.e., less than an hour), is possible. Fast acquisitions of different metabolic relevant parameters not only reduce experimental time but also provide several types of information for better assessment of muscle physiology. A comparison of our results from healthy subjects with the results from studies using similar exercise protocols shows very good agreement regarding bioenergetics parameters [62].

Clinical potential of the technique was demonstrated in Barth (BTHS) patients. BTHS is characterized by mutations in the gene encoding for tafazzin (TAZ) [70]. Mutations in TAZ results in an increase in monolysocardiolipin and reduction in tetralinoleoyl-cardiolipin, leading to smaller and fragmented mitochondria and markedly reduced respiratory capacity. Skeletal muscle bioenergetics, as determined from post-exercise PCr recovery kinetics (34.5 ± 7.5 s control, vs 92.5 ± 23.6 s patients) and oxidative capacity (1.01 ± 0.18 mM/s control vs 0.41 ± 0.13 mM/s patients) using ^{31}P MRS, were severely impaired in BTHS patients, and these results agree with previous reports[62]. A novel finding in this work is that the O_2 extraction from the blood was severely impaired (Figure 2.12d), and post-exercise recovery time constant of SvO_2 (~ 20 s) is significantly shorter than that of healthy control (~ 70 s). The physiological mechanism behind

this is beyond the scope of current study; however, it is interesting to consider parallels with excess post-exercise oxygen consumption (EPOC)[99, 100]. It is known that after exercise the body needs sustained oxygen consumption as it needs to replace the oxygen used by working muscles for replenishment of energy resources. In healthy individuals, the SvO_2 recovery time constant (70.46 ± 4.76 s) is ~ 2 times higher than that of the PCr recovery time constant (34.5 ± 7.5 s), which is consistent with whole-body elevated oxygen uptake in recovery. However, in patients, the SvO_2 dynamics recover faster than the PCr, indicating reduced oxygen availability for ATP production. In contrast to energetic and SvO_2 measurements, the blood flow and relative perfusion characteristic in the patients were not different from the healthy controls, which suggests that central (i.e., cardiac) impairment is not a limiting factor. The reasons behind this will be addressed in more targeted future studies.

There are several limitations that need to be addressed. A requirement for the repeatability of measured parameters is related to the muscle power output. We did not digitally record the output from the ergometer. However, monitoring increased pressure when the pedal was fully depressed ensured that the participants complied with the exercise protocol, and subject compliance was enforced with constant verbal feedback. To improve the repeatability of measurements, it is recommended that the power output and work performed by the subject should be recorded and used to normalize the effort. Another potential limitation is multiple exercise bouts with a relatively short rest period. Multiple exercise bouts have shown adaptation of muscle metabolic and energetic response, i.e., first exercise session may potentially alter the parameters measured in the following acquisitions[101, 102]. It is possible that the muscle hemodynamics did not return to baseline due to relatively short rest periods in this study. Low work load exercise was designed to reduce this complication. A limitation of the SvO_2 quantification method is the assumption of

cylindrical approximation for blood vessels and that they are oriented along the direction of magnetic fields. This has been studied previously, and the absolute error in SvO_2 was found to be less than 2% for elliptical cross-section with tilt correction [83]. Fick's principle can be used to calculate skeletal muscle oxygen consumption by combining bulk blood flow with arteriovenous oxygen difference and muscle mass [52]. This requires measurement of the muscle mass, which was not measured; hence, an estimate of muscle oxygen consumption is not available. Several factors can affect blood flow and mitochondrial function (i.e., physical activity levels, nutritional status, pathologies, lifestyle, etc.), which are highly varied and therefore difficult to control. All subjects in this study were recreationally physically active, i.e., no regular exercise, and free of overt disease, so the findings of this study might not apply in subjects with pathological conditions, unfit participants, or subjects with varying physical activity levels.

In summary, we demonstrated the feasibility and repeatability of noninvasive measurement of arterial blood flow, venous oxygen saturation, and bulk changes in relative perfusion after muscle stimulation. Our results are in close agreement with previous reports and within the physiological range. We further demonstrated the measurement of muscle energetics during the same session without lingering effects of multiple exercise bouts. Although further validation is required in patient populations, these techniques have great potential to enable the study of multiple related parameters. It can play a vital role in monitoring and management of patients with a broad range of diseases that directly or indirectly affect muscle hemodynamics and metabolism.

Chapter 3

Non-contrast Estimate of Blood-Brain Barrier Permeability in Humans using Arterial Spin Labeling and Magnetization Transfer

3.1 Background

The blood-brain barrier (BBB) plays the most important role in regulating water and nutrients delivery between vascular space and tissue space in the central nervous system (CNS) [24]. The BBB integrity is critical for the protection of the CNS as it restricts neurotoxins and macromolecules, providing a suitable functional environment for the nervous system [25]. Disruption in the BBB may cause the alteration of normal functional activity of the nervous system. CNS diseases, such as multiple sclerosis, Alzheimer's disease, Parkinson's disease, brain tumor, stroke, etc., are associated with compromised BBB [26-30].

Currently, the most widely used methods to evaluate BBB permeability are computed tomography (CT) and dynamic contrast-enhanced (DCE) MRI [103]. CT provides estimates of BBB permeability via passive transport of iodinated contrast agents [104]. DCE MRI uses an injection of gadolinium (Gd) based contrast agent such as Gd-DTPA and is sensitive to major BBB leakage, but its ability to detect subtle disruption of BBB at an early stage of disease is challenging [105-108]. CT exposes patients to radiation, and DCE is not feasible for patients with impaired kidney function and is associated with contrast agent deposition in the brain with potential neurotoxic side effects [109, 110].

Arterial spin labeling (ASL) MRI measures perfusion using magnetically labeled water as an endogenous tracer, which has been applied successfully in the brain and other organs[79, 111, 112]. The conventional ASL model assumes that water is freely diffusible between the intravascular and the extravascular compartment; however, this assumption is not valid in the brain and several studies have shown restricted water exchange between the vascular and the tissue space [15, 20-23] with the BBB playing a central role in restricting the water exchange between the two compartments. Modification to the ASL pulse sequence that can differentiate between the labeled water signal from vascular and tissue compartments will allow estimation of the water that leaves the vasculature and enters the brain tissue, enabling the determination of BBB permeability. The advantage of using endogenous water is that the small molecular weight of water potentially makes it more sensitive to the subtle changes of BBB permeability in the early stage of disease [113].

Several non-invasive MRI approaches have been demonstrated to estimate BBB permeability. Intra- and extravascular water exchange can be quantified using differences in T_1 or T_2 relaxation time constants. However, these techniques are prone to low SNR, and the effect of tissue oxygenation on relaxation times can cause errors in the measurement [16, 114-117]. Another approach is to use phase-contrast velocity-encoding to estimate the fraction of labeled arterial blood that drains directly into cerebral veins, but the measurements are limited to global (whole brain) estimates[117]. Estimation of BBB water exchange rate has been demonstrated with diffusion-weighted (DW) – ASL techniques[118-121]. DW-ASL approaches require complex signal models with regularizing algorithms to smooth and improve the signal-to-noise ratio, and involve difficult deconvolution approaches. Bulk motion in DW-ASL based approaches can further complicate the calculation.

Brain tissue and vascular water have different magnetization transfer (MT) effects due to the presence of macromolecules in the brain tissue. When macromolecules are saturated with additional off-resonance RF pulses during ASL signal acquisition, the vascular water experiences little or no MT compared to the tissue water [122, 123]. A comparison of perfusion signals measured with and without MT thus enables estimation of water extraction fraction (E) and permeability surface area product (PS). This MT-based ASL technique has been previously validated in rats by changing the cerebral blood flow and chemical disruption of the BBB [20].

This approach has not been demonstrated in human studies. The previous study on rodents used the CASL sequence, which is not preferred for human studies, especially at the ultra-high field due to the excessive amount of RF power deposition. The CASL approach also requires a two-coil setup with excellent RF isolation between the labeling coil and the detection coil to enable arterial spin labeling without saturation of brain macromolecular spins. This requires additional hardware and is not practical for a 7T human scanner. The purpose of this study was to develop a new pulse sequence to measure water extraction fraction, BBB permeability, and magnetization transfer ratio (MTR) in human subjects at 7T. We used a FAIR QUIPSS II ASL approach developed by Wong et al. [111] with additional MT saturation pulses turned ON/OFF in an interleaved fashion to acquire perfusion signals in the presence and absence of the macromolecular saturation. We demonstrate the first application of the MT-FAIR pulse sequence to measure BBB permeability in human subjects. We also present updated solutions to the Bloch equation that include the magnetization transfer effect. These solutions are similar to the ones previously presented for the CASL sequence but have been modified for the FAIR approach [124]. We evaluated the test-retest reproducibility and the sensitivity of the approach to measure changes in BBB permeability due to altered hemodynamics with caffeine challenge. The method also generates simultaneous estimates of co-

registered MTR images. MTR is sensitive to the density of macromolecules, such as protein and lipids in the myelin sheath, and can provide an estimate of the macromolecular density [125]. The results of this work have already been published [126].

3.2 Materials and Methods

3.2.1 Theory

In the FAIR-ASL technique, a slice selective (SS) inversion pulse is used to acquire the tag image where the incoming arterial blood spins are not inverted, but the imaging slice spins are inverted. In the control image, a non-slice selective (NS) inversion pulse is used, and both spins, i.e., the incoming arterial blood and the imaging slice, are inverted [124]. The difference between the tag image and the control image is a measure of the blood delivered to the tissue and is used to calculate perfusion. The FAIR-QUIPSS II technique uses additional saturation pulses to define the time width of the labeling bolus, and the post-labeling delay (PLD) is selected to make the acquisition insensitive to the transit delay [111, 127, 128]. The model used to calculate perfusion assumes that the labeled arterial water is freely diffusible between the vasculature and the tissue compartment. This assumption is not valid in the brain where the BBB restricts the free exchange of water between the vasculature and the tissue compartment[15, 20, 21, 23]. A modified model that includes the restricted exchange of the labeled water allows the estimation of the extraction fraction from ASL experiments. This can be achieved by techniques that can distinguish between the intravascular and the tissue water.

MT caused by the cross-relaxation between free water and tissue macromolecules can differentiate between the labeled vascular and tissue water because the water in vasculature has little or no magnetization transfer effect[20, 123]. Therefore, MT combined with ASL can be used to determine the fraction of labeled vascular water that is delivered to the tissue, allowing us to calculate the water extraction fraction. Modified Bloch equations incorporating the effect of perfusion and MT were previously developed for MT-CASL sequence [20]. In this work, we present updated equations based on the FAIR-MT pulse sequence and demonstrate the quantification of water extraction fraction and permeability surface area product in human subjects. The main difference between CASL and FAIR is that the imaging slice spins are relaxed for both control and tag images in the CASL experiment, whereas the imaging slice spins are inverted for both control and tag images in the FAIR approach.

A complete theory for the derivation of the water extraction fraction based on a FAIR QUIPSS II pulse sequence with MT saturation pulses is presented in section 3.2.1.1 (Detailed derivation for the water extraction fraction). Here we present the necessary relationships relevant to the measurement. The schematic demonstrating the blood water flow with the restricted exchange in a unit volume is shown in Figure 3.1. When tagged arterial water enters the imaging region, the main fraction of this water (*E*) diffuses into the tissue space, while the rest of the tagged water (*1-E*) flows into the venous region. In the tissue space, there is a cross-relaxation (magnetization transfer) between tissue water and tissue macromolecules. Modified Bloch equations that include magnetization transfer and restricted water exchange are given by [20]

$$\frac{dM_t(t)}{dt} = \frac{M_t^0 - M_t(t)}{T_{1t}} - k_f M_t(t) + k_r M_m(t) + fE(M_a(t) - M_v(t)) \qquad 3.1$$

$$\frac{dM_m(t)}{dt} = \frac{M_m^0 - M_m(t)}{T_{1m}} + k_f M_t(t) - k_r M_m(t) \qquad 3.2$$

where f = microvascular cerebral blood flow (CBF)/unit time/unit volume (or perfusion); E = water extraction fraction; $M_a(t)$, $M_v(t)$ = longitudinal magnetization of water in arterial blood and venous blood, respectively; k_f, k_r = the forward and reverse exchange rate constants for magnetization transfer; $M_t(t)$= tissue longitudinal magnetization; $M_m(t)$ = longitudinal magnetization of macromolecular protons; M_t^0, M_m^0 = equilibrium value of $M_t(t)$ and $M_m(t)$; T_{1t}, T_{1m} = relaxation time constants of brain water protons and macromolecular water protons.

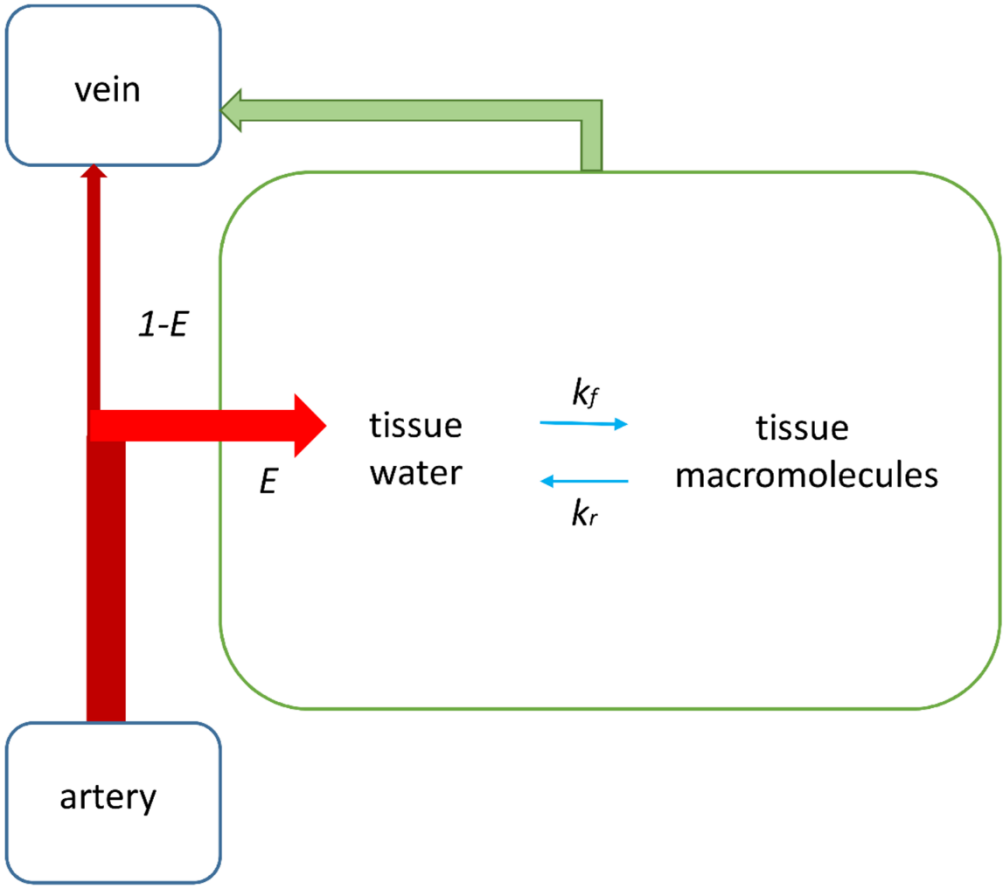

Figure 3.1: Schematic of the model of a unitary voxel for perfusion measurement including water extraction fraction and magnetization transfer (MT) effects due to the cross relaxation between tissue macromolecules and tissue water. The main fraction (*E*) of the labeled arterial water diffuses into the tissue space and exchanges with tissue water. The other non-exchangeable fraction (*1-E*) drains into the venous side. In the tissue space, the MT effect takes place between tissue water and tissue macromolecules with forward and reverse MT rate constants of k_f and k_r. Additionally, a portion of the arterial water that was extracted by the tissue exchanges back into the vein.

We make three modifications to the previously described theory: (i) a 90^0 pre-saturation pulse before the inversion pulse at *t=0* destroys any residual magnetization for both tag and control image acquisition in the FAIR technique (Figure 3.2); hence the initial condition for both cases is $M_t(t=0)= 0$; (ii) brain macromolecules are assumed to be partially saturated instead of complete saturation, i.e. $M_m(t)=nM_m^o$ for all *t* (where *n* is the fraction of unsaturated macromolecules); and (iii) the tagged blood has a T_1 decay during the arterial transit time (ATT). Incorporating these into Eqs. 3.1 & 3.2, the solution to the modified Bloch equation is given by

$$M_t(t) = \left(M_t^0 - T_1^{app} M_t^0 \left(k_f(1-n) + \frac{f}{\lambda} 2\varepsilon E \right) \right) - \left(M_t^0 - T_1^{app} M_t^0 \left(k_f(1-n) + \frac{f}{\lambda} 2\varepsilon E \right) \right) e^{-t/T_1^{app}} \quad 3.3$$

where $1/T_1^{app}$ = apparent relaxation rate constant, $\varepsilon = e^{-ATT/T_{1,blood}}$, $T_{1,\ blood}$ = longitudinal relaxation time of blood, and λ= brain-blood partition coefficient for water. ε = 0 for blood during slice selective acquisition. Mean arterial transit time is used as ATT, and its effect on the quantification of extraction fraction is addressed in the discussion. The mathematical form of ε

described here is similar to the arterial input function for CASL experiments [128, 129]. Although not completely accurate, we have assumed this form of ε to account for the mean signal decay of the tagged spins with the relaxation time constant of the blood during transit through arteries, before the tagged blood reaches the capillary site and starts exchanging with the tissue. More accurate assumptions can be made which is addressed in the discussion section.

The measured MRI signal (S) in a unit volume has contributions from both the vascular water and the tissue water ($M_t(t)$). The relative contributions depend on the volume fractions occupied by the two compartments and need to be included in perfusion model [20]. When macromolecules are saturated, Eqs 3.1 and 3.2 can be solved to determine the perfusion as given below (details in section 3.2.1.1)

$$f = \left(\frac{1}{T_{1t}} + nk_f\right)\left[\frac{\lambda}{E}\left(\frac{S_{SS1} - S_{NS1}}{S_{NS1} + (2\varepsilon - 1)S_{SS1}}\right) - \frac{2V\varepsilon(1-E)}{E}\left(\frac{S_{SS2}}{S_{NS1} + (2\varepsilon - 1)S_{SS1}}\right)\right] \qquad 3.4$$

$$= \left(\frac{1}{T_{1t}} + nk_f\right) f_m^0$$

where V = vascular volume fraction in a unit voxel; S_{SS1}, S_{NS1} = measured SS and NS signals with MT pulse on; f_m^0 = apparent perfusion with MT pulses ON and without accounting for the cross-relaxation between tissue water and tissue macromolecules. Similarly, perfusion without macromolecular saturation is given by

$$f = \left(\frac{1}{T_{1t}} + \frac{k_f}{1 + k_r T_{1m}}\right)\left[\frac{\lambda}{E}\left(\frac{S_{SS2} - S_{NS2}}{S_{NS2} + (2\varepsilon - 1)S_{SS2}}\right)\right. \qquad 3.5$$

$$\left. - \frac{2V\varepsilon(1-E)}{E}\left(\frac{S_{SS2}}{S_{NS2} + (2\varepsilon - 1)S_{SS2}}\right)\right]$$

$$= \left(\frac{1}{T_{1t}} + \frac{k_f}{1 + k_r T_{1m}}\right) f^0$$

where S_{SS2}, S_{NS2} are measured SS and NS signals with MT pulse off; f^0 is the apparent perfusion with MT pulses OFF and without accounting for the cross-relaxation between tissue water and tissue macromolecules. Here it is to be noted that Eqs. 3.3-3.5 are similar to those derived before [20] with the modification for the FAIR sequence as described above. Eq 3.4 and Eq 3.5 can be combined to calculate the water extraction fraction

$$E = 1 - \frac{1}{2V\varepsilon S_{SS2}} \left[\frac{\left(\frac{\frac{1}{T_{1t}} + nk_f}{\frac{1}{T_{1t}} + \frac{k_f}{1 + k_r T_{1m}}} \right) \frac{S_{SS1} - S_{NS1}}{S_{NS1} + (2\varepsilon - 1) S_{SS1}} - \frac{S_{SS2} - S_{NS2}}{S_{NS2} + (2\varepsilon - 1) S_{SS2}}}{\left(\frac{\frac{1}{T_{1t}} + nk_f}{\frac{1}{T_{1t}} + \frac{k_f}{1 + k_r T_{1m}}} \right) \frac{1}{S_{NS1} + (2\varepsilon - 1) S_{SS1}} - \frac{1}{S_{NS2} + (2\varepsilon - 1) S_{SS2}}} \right] \quad 3.6$$

The above equation can be used to calculate E, but it requires additional experiments to determine k_f, k_r, and T_{1m}. Alternately, Eq 3.6 can be simplified in terms of the ratio of apparent perfusion signals (f^0) measured with and without magnetization transfer. The conventional model for perfusion quantification using the QUIPSS II FAIR technique does not account for cross-relaxation between tissue water and macromolecules; hence, the apparent perfusion (f^0) is directly proportional to the difference of slice selective and non-selective acquisitions [111, 127]: $f^0 \propto (S_{SS} - S_{NS})$; where S_{SS}, S_{NS} are SS and NS acquisitions. Variable β can be calculated from the ratio of apparent perfusions measured under similar conditions with and without magnetization transfer from Eqs 3.4 and 3.5

$$\beta = \frac{S_{SS} - S_{NS}}{S_{SSm} - S_{NSm}} = \frac{\frac{1}{T_{1t}} + nk_f}{\frac{1}{T_{1t}} + \frac{k_f}{1 + k_r T_{1m}}} \quad 3.7$$

where S_{SSm}, S_{NSm} are SS and NS acquisitions with MT; S_{SS}, S_{NS} are SS and NS acquisitions without MT acquired by the QUIPSS II FAIR ASL technique.

Combining Eqs 3.6 and 3.7 the water extraction fraction can be determined from

$$E = 1 - \frac{1}{2 \,.\, V \,.\, \varepsilon \,.\, S_{SS}} \left[\frac{\beta \frac{S_{SSm} - S_{NSm}}{(2\varepsilon - 1)S_{SSm} + S_{NSm}} - \frac{S_{SS} - S_{NS}}{(2\varepsilon - 1)S_{SS} + S_{NS}}}{\frac{1}{\beta \frac{1}{(2\varepsilon - 1)S_{SSm} + S_{NSm}} - \frac{1}{(2\varepsilon - 1)S_{SS} + S_{NS}}}} \right] \quad 3.8$$

Perfusion can be quantified by either Eq 3.5 or using the conventional model, Eq 3.9

$$f = \frac{6000 \,.\, (S_{SS} - S_{NS}) . e^{TI_2 / T_{1,blood}}}{2 \,.\, \alpha \,.\, TI_1 \,.\, S_0} \quad 3.9$$

where $T_{1,\,blood}$ is the longitudinal relaxation time of blood, S_0 is the steady state reference signal, TI_1 is the time between the inversion pulse and the saturation pulse, α is the labeling efficiency, and factor 6000 is used to convert perfusion in units of mL/100g/min (assuming a tissue density of 1 g/mL [130]). In this work, we have used Eq 3.9 to determine perfusion to be consistent with the existing literature. Although Eq 3.5 accounts for cross-relaxation and restricted water exchange, it requires T_{1t}, T_{1m}, k_f, and k_r values. These can be measured in a separate experiment or used from previously published studies. Use of Eq 3.5 will yield perfusion within a few percent of the conventional model (comparison is provided in the results section).

Permeability surface area product is calculated according to Renkin-Crone Model [131, 132]

$$PS = -\ln(1 - E) \,.\, f \tag{3.10}$$

The magnetization transfer ratio is determined using [133]

$$MTR = 1 - \frac{S_{SSm}}{S_{SS}} \tag{3.11}$$

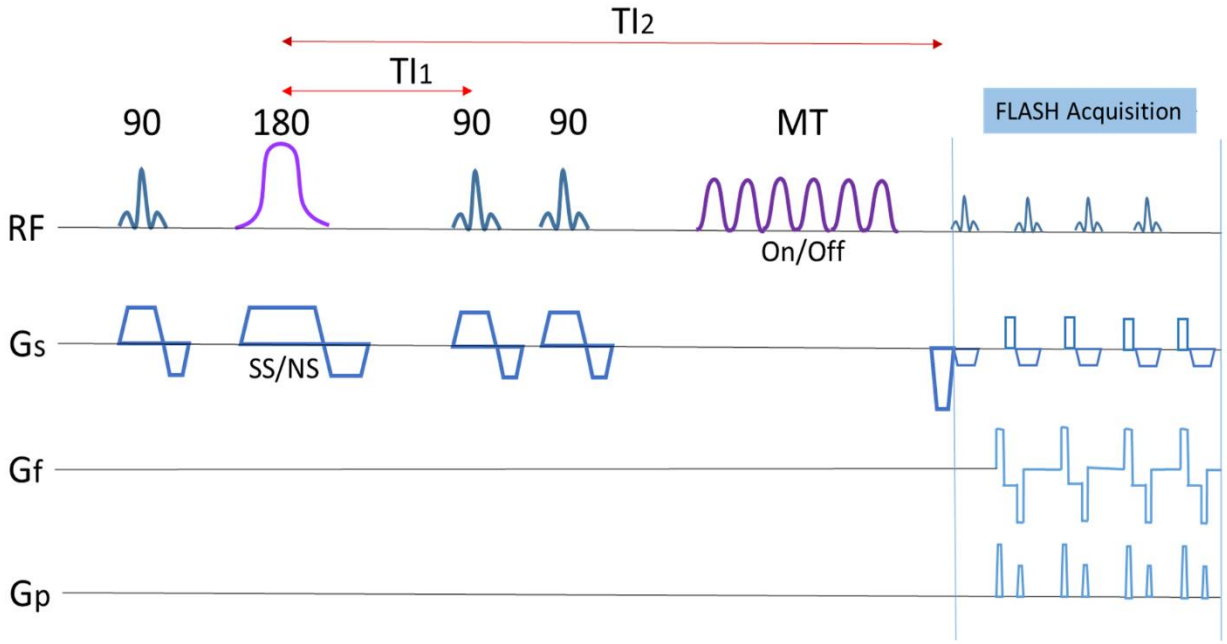

Figure 3.2: Schematic of the pulse sequence used for imaging. The sequence is composed of 90° pre-saturation pulse, followed by a slice selective (SS) or non-selective (NS) 180° inversion pulse for tag and control images, followed by two 90° saturation pulses. This whole sequence was followed by MT (on/off) pulses to acquire tag and control signals with and without macromolecular saturation, respectively, in an interleaved manner. FLASH readout was used for this data acquisition. Here, G_s is the slice gradient, G_f is the frequency gradient, and G_p is the phase

gradient. TI_1 is the time between inversion and saturation pulses, and TI_2 is the time between inversion pulse and data acquisition.

3.2.1.1 Detailed derivation for the water extraction fraction

Detailed derivation for the water extraction fraction is presented in this section. According to the proposed model, the modified Bloch equations are

$$\frac{dM_t(t)}{dt} = \frac{M_t^0 - M_t(t)}{T_{1t}} - k_f M_t(t) + k_r M_m(t) + f(M_a(t) - M_v(t)) \quad 3.12$$

$$\frac{dM_m(t)}{dt} = \frac{M_m^0 - M_m(t)}{T_{1m}} + k_f M_t(t) - k_r M_m(t) \quad 3.13$$

Here, f = perfusion (mL/100g/min); E = water extraction fraction; $M_a(t)$, $M_v(t)$ = longitudinal magnetization of water in arterial blood and venous blood, respectively; k_f, k_r = the forward and reverse exchange rate constants for magnetization transfer; $M_t(t)$= tissue longitudinal magnetization; $M_m(t)$ = longitudinal magnetization of macromolecular protons; M_t^0, M_m^0 = equilibrium value of $M_t(t)$ and $M_m(t)$; T_{1t}, T_{1m} = relaxation time constants of brain water protons and macromolecular water protons.

Venous water magnetization can be expressed as

$$M_v(t) = \frac{M_t(t)}{\lambda} \quad 3.14$$

Here, λ= brain-blood partition coefficient.

In the case of diffusion limited tracer, including the water extraction fraction E, the term ($M_a(t)$-$M_v(t)$) in Eq. 3.12 should be replaced with $E(M_a(t)-M_v(t))$.

The inflow and outflow should be equal at steady state,

$$M_a^0 = \frac{M_t^0}{\lambda} \tag{3.15}$$

MT in tissue is assumed to be in equilibrium so that

$$k_f M_t^0 = k_r M_m^0 \tag{3.16}$$

The tagged blood has a T_1 decay during arterial transit time (ATT). Thus, the arterial spin can expressed as

$$M_a(t) = (1 - 2\varepsilon)M_a^0 \tag{3.17}$$

where $\varepsilon = e^{-ATT/T_{1,blood}}$, $T_{1,\,blood}$ = longitudinal relaxation time of blood. ε = 0 for blood during slice selective acquisition.

Using these assumptions, Eqs. 3.12 and 3.13 become

$$\frac{dM_t(t)}{dt} = \frac{M_t^0 - M_t(t)}{T_{1t}} - k_f M_t(t) + k_r M_m(t) + \frac{f}{\lambda} E(1 - 2\varepsilon)M_t^0 - \frac{f}{\lambda} E M_t(t) \tag{3.18}$$

$$\frac{dM_m(t)}{dt} = \frac{\frac{k_f}{k_r} M_t^0 - M_m(t)}{T_{1m}} + k_f M_t(t) - k_r M_m(t) \tag{3.19}$$

In practice, there is a 90^0 pre-saturation pulse before the inversion pulse at *t=0* for both tag and control image acquisition; hence, the initial condition for both cases is $M_t(t=0) = 0$. Also, brain macromolecules are assumed to be partially saturated instead of complete saturation, i.e., $M_m(t) = nM_m^o$ for all *t* (where *n* is the saturated macromolecule fraction). The solution to the modified Bloch equation is

$$M_t(t) = \left(M_t^0 - T_1^{app} M_t^0 \left(k_f(1-n) + \frac{f}{\lambda} 2\varepsilon E \right) \right) - \left(M_t^0 - T_1^{app} M_t^0 \left(k_f(1-n) + \frac{f}{\lambda} 2\varepsilon E \right) \right) e^{-t/T_1^{app}} \quad 3.20$$

where $1/T_1^{app}$ is the apparent relaxation rate constant given by

$$\frac{1}{T_1^{app}} = \frac{1}{T_{1t}} + k_f + \frac{f}{\lambda} E \quad 3.21$$

At steady state, the non-selective (NS) and slice selective (SS) magnetizations are given by

$$M_{NS1} = M_t^0 \left(\frac{\frac{1}{T_{1t}} + nk_f + \frac{fE}{\lambda}(1-2\varepsilon)}{\frac{1}{T_{1t}} + k_f + \frac{fE}{\lambda}} \right) \quad 3.22$$

$$M_{SS1} = M_t^0 \left(\frac{\frac{1}{T_{1t}} + nk_f + \frac{fE}{\lambda}}{\frac{1}{T_{1t}} + k_f + \frac{fE}{\lambda}} \right) = M_{NS1} \left(\frac{\frac{1}{T_{1t}} + nk_f + \frac{fE}{\lambda}}{\frac{1}{T_{1t}} + nk_f + \frac{fE}{\lambda}(1-2\varepsilon)} \right) \quad 3.23$$

The perfusion can be quantified by the following equation that accounts for MT:

$$f = \frac{\lambda}{E} \left(\frac{1}{T_{1t}} + nk_f \right) \left(\frac{M_{SS1} - M_{NS1}}{M_{NS1} + (2\varepsilon - 1) M_{SS1}} \right) \quad 3.24$$

When macromolecules are not saturated (MT pulse off), the steady state magnetizations for NS and SS acquisitions are then given by

$$M_{NS2} = M_t^0 \left(\frac{\frac{1}{T_{1t}} + \frac{k_f}{1 + k_r T_{1m}} + \frac{fE}{\lambda}(1 - 2\varepsilon)}{\frac{1}{T_{1t}} + \frac{k_f}{1 + k_r T_{1m}} + \frac{fE}{\lambda}} \right) \quad 3.25$$

$$M_{SS2} = M_t^0 = M_{NS2} \left(\frac{\frac{1}{T_{1t}} + \frac{k_f}{1 + k_r T_{1m}} + \frac{fE}{\lambda}}{\frac{1}{T_{1t}} + \frac{k_f}{1 + k_r T_{1m}} + \frac{fE}{\lambda}(1 - 2\varepsilon)} \right) \quad 3.26$$

The perfusion when the MT pulses are off is given by:

$$f = \frac{\lambda}{E} \left(\frac{1}{T_{1t}} + \frac{k_f}{1 + k_r T_{1m}} \right) \left(\frac{M_{SS2} - M_{NS2}}{M_{NS2} + (2\varepsilon - 1) M_{SS2}} \right) \quad 3.27$$

These equations are valid when the vascular signal is suppressed by the crusher gradient. If no crusher gradient is applied and the signal contains contributions from both tissue and vascular compartments, the signal can be expressed as

$$S = \frac{M_t(t)}{\lambda}(1 - V) + M_V(t)V \quad 3.28$$

where $M_V(t)$ = magnetization of water in the vasculature and V = vascular volume fraction in a unit voxel. $M_V(t)$ will have contribution from the fraction of the arterial water that does not diffuse into the tissue and from the water that diffuses back to the vasculature from the tissue.

$$M_V(t) = (1 - E) M_a(t) + E \frac{M_t(t)}{\lambda} \quad 3.29$$

Using Eqs. 3.17, 3.26, 3.28 and 3.29, the voxel signal can be written as

$$S(t) = (1 - (1 - E)V)\frac{M_t(t)}{\lambda} + (1 - E)V(1 - 2\varepsilon)\frac{M_{SS2}}{\lambda} \quad 3.30$$

The NS and SS signals with macromolecular saturation are given by

$$S_{NS1} = (1 - (1 - E)V)\frac{M_{NS1}}{\lambda} + (1 - E)V(1 - 2\varepsilon)\frac{M_{SS2}}{\lambda} \quad 3.31$$

$$S_{SS1} = (1 - (1 - E)V)\frac{M_{SS1}}{\lambda} + (1 - E)V\frac{M_{SS2}}{\lambda} \quad 3.32$$

Perfusion with macromolecular saturation is given by

$$f = \left(\frac{1}{T_{1t}} + nk_f\right)\left[\frac{\lambda}{E}\left(\frac{S_{SS1} - S_{NS1}}{S_{NS1} + (2\varepsilon - 1)S_{SS1}}\right) - \frac{2V\varepsilon(1 - E)}{E}\left(\frac{S_{SS2}}{S_{NS1} + (2\varepsilon - 1)S_{SS1}}\right)\right] \quad 3.33$$

$$= \left(\frac{1}{T_{1t}} + nk_f\right)f_m^0$$

where f_m^0 = apparent perfusion - the subscript represents that MT pulse is ON and the superscript means without accounting for the cross relaxation between tissue water and tissue macromolecules.

Similarly NS and SS signals in absence of macromolecular saturation are given by

$$S_{NS2} = (1 - (1 - E)V)\frac{M_{NS2}}{\lambda} + (1 - E)V(1 - 2\varepsilon)\frac{M_{SS2}}{\lambda} \quad 3.34$$

$$S_{SS2} = (1 - (1 - E)V)\frac{M_{SS2}}{\lambda} + (1 - E)V\frac{M_{SS2}}{\lambda} = \frac{M_{SS2}}{\lambda} \quad 3.35$$

Perfusion without macromolecular saturation can be written as

$$f = \left(\frac{1}{T_{1t}} + \frac{k_f}{1 + k_r T_{1m}}\right)\left[\frac{\lambda}{E}\left(\frac{S_{SS2} - S_{NS2}}{S_{NS2} + (2\varepsilon - 1)S_{SS2}}\right)\right. \quad 3.36$$

$$\left. - \frac{2V\varepsilon(1-E)}{E}\left(\frac{S_{SS2}}{S_{NS2} + (2\varepsilon - 1)S_{SS2}}\right)\right] = \left(\frac{1}{T_{1t}} + \frac{k_f}{1 + k_r T_{1m}}\right) f^0$$

where f^0 = apparent perfusion with MT pulses OFF and without accounting for the cross relaxation between tissue water and tissue macromolecules. From Eqs. 3.33 and 3.36 water extraction fraction can be calculated as

$$E = 1 - \frac{1}{2V\varepsilon S_{SS2}}\left[\frac{\left(\frac{\frac{1}{T_{1t}} + nk_f}{\frac{1}{T_{1t}} + \frac{k_f}{1 + k_r T_{1m}}}\right)\frac{S_{SS1} - S_{NS1}}{S_{NS1} + (2\varepsilon - 1)S_{SS1}} - \frac{S_{SS2} - S_{NS2}}{S_{NS2} + (2\varepsilon - 1)S_{SS2}}}{\left(\frac{\frac{1}{T_{1t}} + nk_f}{\frac{1}{T_{1t}} + \frac{k_f}{1 + k_r T_{1m}}}\right)\frac{1}{S_{NS1} + (2\varepsilon - 1)S_{SS1}} - \frac{1}{S_{NS2} + (2\varepsilon - 1)S_{SS2}}}\right] \quad 3.37$$

Conventional model for perfusion quantification using the QUIPSS II FAIR technique does not account for cross relaxation between tissue water and macromolecules; hence, the apparent perfusion (f^0) is directly proportional to the difference of slice selective and non-selective acquisitions

$$f^0 \; \alpha \; (S_{SS} - S_{NS}) \quad 3.38$$

where S_{SS}, S_{NS}= SS and NS acquisitions. The ratio of apparent perfusion signals acquired with and without MT (β) can be expressed using Eqs 3.33, 3.36 and 3.38

$$\beta = \frac{S_{SS} - S_{NS}}{S_{SSm} - S_{NSm}} = \frac{\frac{1}{T_{1t}} + nk_f}{\frac{1}{T_{1t}} + \frac{k_f}{1 + k_r T_{1m}}} \quad 3.39$$

where S_{SSm}, S_{NSm}= SS and NS acquisitions with MT; S_{SS}, S_{NS} = SS and NS acquisitions without MT acquired by the QUIPSS II FAIR ASL technique.

Combining Eqs 3.37 and 3.39, the water extraction fraction can be determined from

$$E = 1 - \frac{1}{2 \,.\, V \,.\, \varepsilon \,.\, S_{SS}} \left[\frac{\beta \frac{S_{SSm} - S_{NSm}}{(2\varepsilon - 1)S_{SSm} + S_{NSm}} - \frac{S_{SS} - S_{NS}}{(2\varepsilon - 1)S_{SS} + S_{NS}}}{\beta \frac{1}{(2\varepsilon - 1)S_{SSm} + S_{NSm}} - \frac{1}{(2\varepsilon - 1)S_{SS} + S_{NS}}} \right] \quad 3.40$$

This shows that perfusion and water extraction fraction can be measured from two ASL perfusion measurements with and without saturation of macromolecules.

3.2.2 Sensitivity to macromolecule saturation

The model developed here is based on the assumption that data is acquired in presence of macromolecular saturation; however, 100% macromolecular saturation is difficult to achieve in vivo and has SAR implications at 7T. MT pulse power or offset frequency can lead to a different amount of macromolecular saturation. Simulations and experiments were performed to examine the effect of the degree of macromolecular saturation on the calculations. The macromolecular saturation was varied from 5% to 90% (i.e., n=0.95 to 0.1 in Eqs. 3.3 and 3.7), and its effects on magnetization transfer contrast, β, and water extraction fraction were determined using Eqs. 3.1−3.3 and 3.7. For these simulations, perfusion and extraction fraction were assumed to be 50

mL/100g/min and 0.9, respectively. Previously published values T_{1t}=2.4 s, T_{1m}=0.5 s, k_f=2.04 s^{-1}, and k_r=5.6 s^{-1} at 7T were used for the simulations [134, 135].

3.2.3 Recruitment

Auburn University institutional review board (IRB) approved the study, and all experiments were performed in accordance with the IRB guidelines and regulations. All the subjects provided informed consent before participating in the study.

Experiments were performed on a Siemens 7T Magnetom (Erlangen, Germany) using a 32-channel head coil. Eighteen healthy volunteers (seven females), age= 27±11 years and weight= 65±9 kg, participated in the study. Eight subjects were scanned twice on the same day to evaluate the test-retest reproducibility. The feasibility and sensitivity of this method were evaluated in four healthy subjects with caffeine challenge, which causes cerebral vasoconstriction[121, 136]. The subjects were scanned at baseline, then removed from the scanner and given a 200 mg caffeine pill. The subjects were immediately repositioned in the scanner, and post-caffeine images were obtained approximately 20 minutes after the caffeine intake. The subjects who participated in the caffeine challenge were asked to abstain from any caffeine consumption 1 day prior to the study. All the other participants were instructed to refrain from caffeine on the day of the scan.

3.2.4 Protocol parameter optimization

To ensure that the labeled blood is delivered to the target tissue, post-labeling delay TI_2 (Figure 3.2) needs to be selected so that the TI_2 >ATT, possibly on the decaying part of ASL difference signal with respect to time [112, 137]. It has been shown that the ATT in FAIR is shorter than pCASL and is expected to be < 1 second [138]. To verify this, ASL signals were acquired for TI_2 values of

1.5, 1.8, 2.3, and 2.8 s in three subjects; and TI_2 = 1.8 s for TI_1 = 0.8 s was chosen for the BBB experiments[112] (details are provided in Results and Discussion sections).

3.2.5 CBF and CBV

Using Poiseuille's law, a simple relationship between CBF and CBV can be expressed as: $CBV\ \alpha\ \sqrt{CBF}$, which has been found to be in good agreement for vasodilation, vasoconstriction, and visual stimulation studies [139-141]. This relationship was used to calculate CBV for the perfusion data after caffeine intake.

3.2.6 Imaging pulse sequence

The pulse sequence used for perfusion data acquisition is shown in Figure 3.2. An in-plane pre-saturation pulse with a duration of 2.56 ms was used before the inversion pulse to suppress any residual signal. An 8 ms long hyperbolic secant adiabatic inversion pulse was used for SS (control image) and NS (tag image) inversion of spins in an interleaved manner. Before in vivo studies, the efficiency of the labeling of the pulse was tested in a phantom [79]. Two post-labeling saturation pulses with a pulse duration of 2.56 ms were used at TI_1 to saturate the labeled blood, where the gap between the proximal edge of the imaging slice and the distal edge of the saturation slice was 10 mm. Six MT pulses, each with a duration of 16.64 ms (bandwidth = 80 Hz), were used to saturate the macromolecules. Saturation pulse ON and OFF frequencies were 500 Hz and 100000 Hz with a flip angle of 500^o to acquire MT ON and MT OFF images, respectively. The data were acquired in an interleaved fashion in this order: SS (MT on)/NS (MT on)/SS (MT off)/NS (MT off). To test how the degree of macromolecule saturation affects the results, additional scans were performed in a subset of subjects by changing the MT pulse angle to 750^o.

A single slice FLASH readout was used with the following imaging parameters: FOV=256 mm, TE=1.39 ms, flip angle=10^{o}, slice thickness=8 mm, base resolution=128, bandwidth=800Hz/pixel with TI_1 = 0.8 s and TI_2 = 1.8 s for the FAIR ASL module. The TR for FLASH readout was 3.1 ms with readout time= ~0.4 s. A total of 120 measurements were acquired (30 for each of SS (MT on), NS (MT on), SS (MT off), and NS (MT off)) with a total acquisition time=4.8 min. A reference proton density image with TR = 2 s was acquired to normalize the perfusion [112].

3.2.7 Data processing

FSL (FMRIB's Software Library, Oxford, UK) and SPM 12 (Spatial Parametric Mapping, London, UK) were used for image preprocessing. First, the bias field was estimated from the reference images and used for bias field correction (with FWHM=20 mm for bias field smoothing; the number of iterations=4 for bias field removal; the number of classes=3) using FSL (Figure 3.3). Then, the images were realigned and co-registered to the reference image and segmented into gray matter (GM) and white matter (WM) using SPM 12 to calculate perfusion, water extraction fraction, permeability surface area product, and magnetization transfer ratio in the GM and the WM. All the rest of the data processing and simulations were performed using MATLAB. The labeling efficiency (α) for PASL at 7T was used as 0.98 [142, 143], which is very close to the value measured from the phantom experiment (0.984). T_1 = 2.1s for blood [143], blood/ brain partition coefficient= 0.9 mL/g [144], and cerebral blood volume (V)= 4.25% [145] were used for the calculations. ε was calculated using ATT = 0.4 s [138].

Two-tailed t-tests were performed on perfusion, extraction fraction, permeability surface area product, and magnetization transfer ratio results from all the subjects to evaluate the differences. Correlations between perfusion, extraction fraction, and permeability surface area product were

assessed using Pearson's coefficient. Bland-Altman analysis was performed to determine the agreement between test-retest results. In all cases $p<0.05$ was accepted as the significance level.

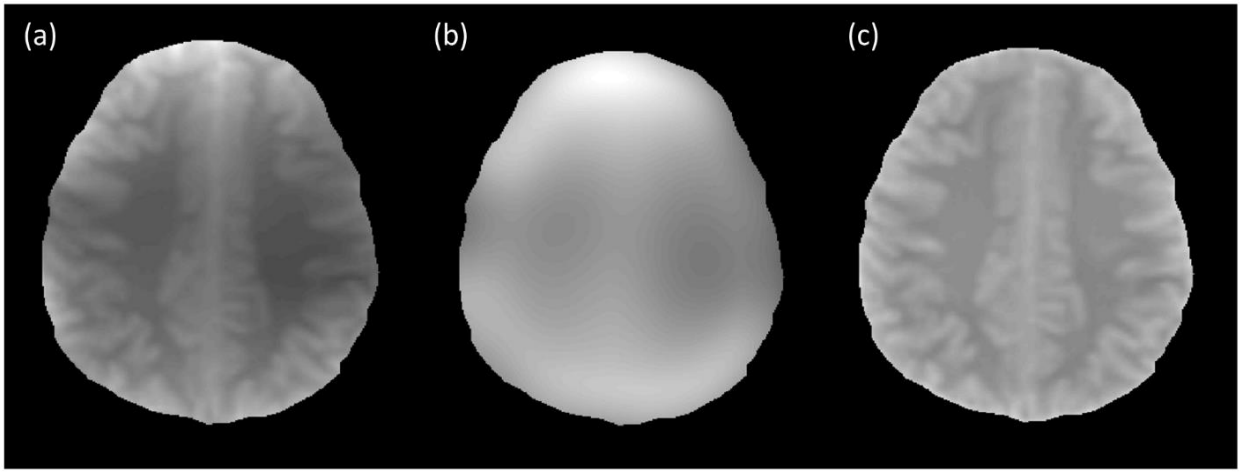

Figure 3.3: Representative example of field inhomogeneity correction. Reference image before bias field correction (a), estimated bias field (b) and image after field inhomogeneity correction (c). The bias field was estimated using FAST (FMRIB's Automated Segmentation Tool) in FSL (FMRIB's Software Library, Oxford, UK) with FWHM=20 mm for bias field smoothing, number of iterations=4 for bias field removal and number of classes=3.

3.3 Results

Simulations show that increased macromolecular saturation results in a lower steady-state tissue magnetization with the same recovery rate constant as expected (Figure 3.4a). As macromolecular saturation increases from 5 % to 90 %, the value of β changes from ~2.46 to ~0.65 (Figure 3.4b). The results demonstrate that if macromolecular saturation is above 15%, the error in calculating the water extraction fraction will be less than ~1.4% (Figure 3.4c). However, for lower

macromolecular saturation, especially if the saturation is <10%, the error in calculating the water extraction fraction starts to increase exponentially.

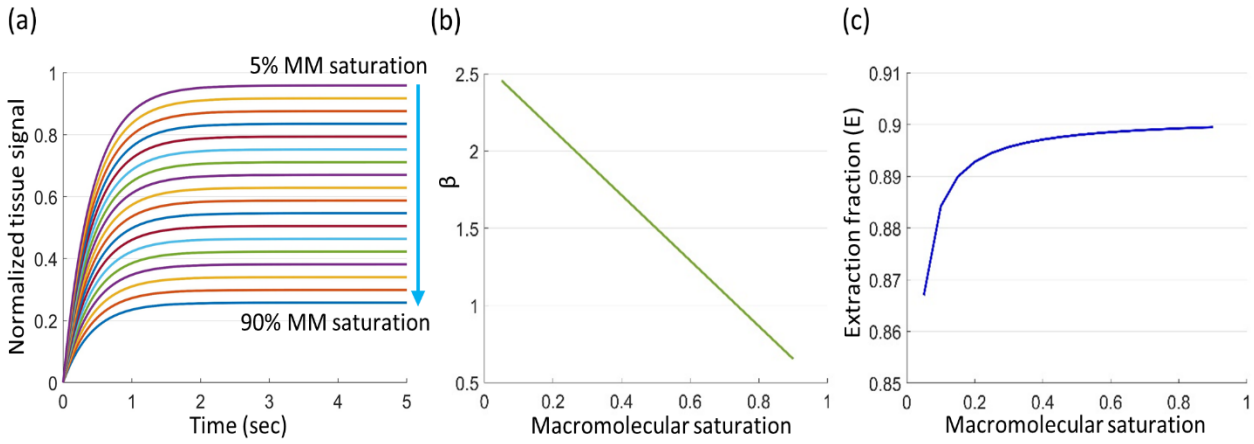

Figure 3.4: Simulation result showing the effect of 5% to 90% macromolecular (MM) saturation on the tissue longitudinal magnetization (a), where the input value of extraction fraction (E) for the simulation was 0.9. Effect of different levels of macromolecular saturation on β (b) and water extraction fraction (c) estimation. These simulations show that when the MM saturation is above 15%, the expected error in water extraction fraction estimation is < 1.4 %. For smaller saturation than this, especially for macromolecular saturation <10%, error in extraction fraction and PS will increase significantly.

The direct spillover effect of the MT pulse was measured to be <2% (Figure 3.5c). The TR (2.4s) used in this study was sufficient to refresh the labeled spins with the FAIR ASL pulse sequence. This was confirmed by repeating the experiment (n = 4) at multiple TRs ranging from 2.4 – 5 s (by increasing the post-acquisition delay). All other acquisition parameters were kept the same. Calculated perfusion both in the GM and the WM was approximately the same for this range of TR (Figure 3.5d). We evaluated the water extraction fraction at multiple TI_2 values ranging from

1 – 3 s (resulting in a TR of 1.6 – 3.6 s) in three subjects (Figure 3.5e). For a short TI_2 (i.e., 1 s), the average extraction fraction was lower. This is expected because short TI_2 does not allow the tagged blood to reach the capillary exchange site and fully exchange with the tissue. For TI_2 >1.5 s (corresponding TR>2.1 s), the average extraction fraction did not change and was in the range of experimental variations (Figure 3.5e).

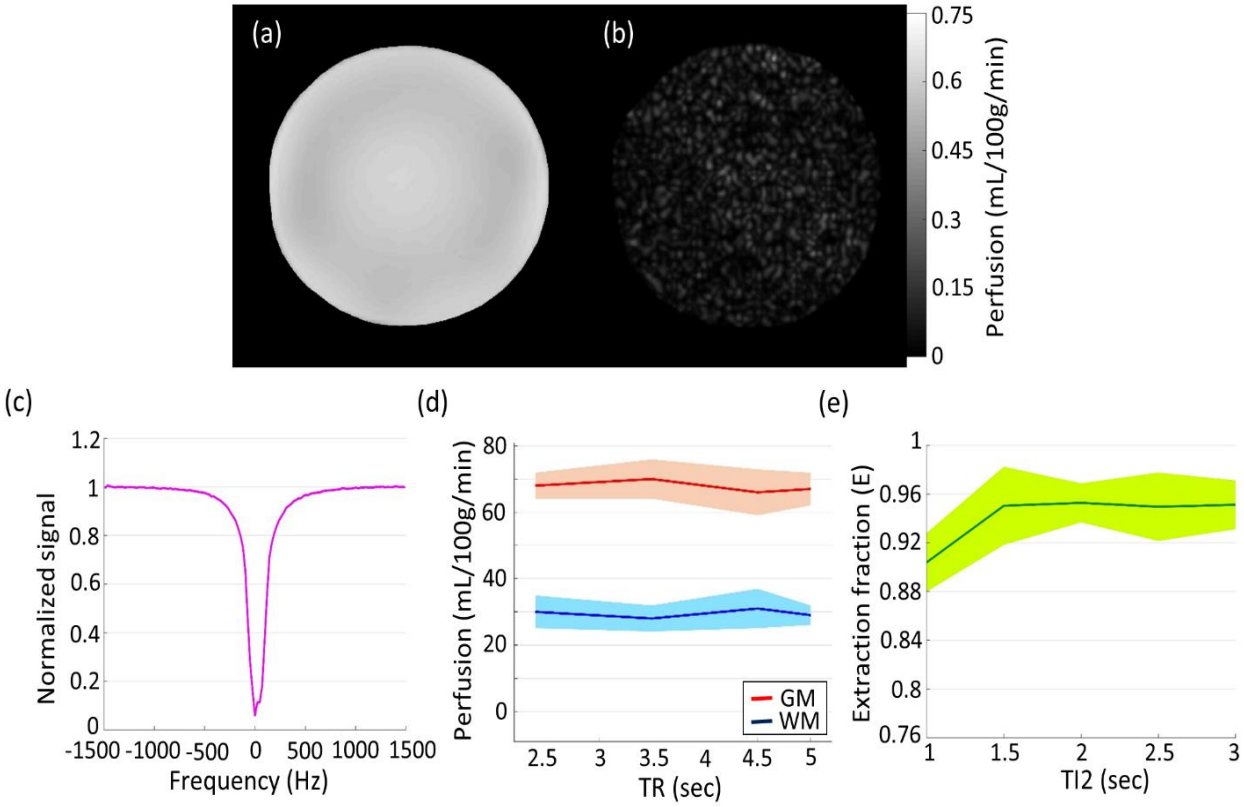

Figure 3.5: Static spherical phantom with diameter =110 mm and T_1=1s (a). Average perfusion on the phantom was 0.15±0.006 mL/100g/min using the same protocol as in vivo experiments demonstrating good subtraction (b). The effect of the off-resonance Gauss MT pulses on the water resonance frequency is illustrated with single voxel spectroscopy in (c). The offset frequency of the MT pulse was varied from -1500Hz to 1500 Hz with the parameters: acquisitions=125,

sampling points=2048, average=1, TR=2 s, TE=16 ms, spectral bandwidth=4000 Hz and voxel size=10×10×10 mm^3. The duration, number of pulses, and flip angle of the MT pulse were the same as the in vivo experiments (16.64 ms, 6 and 500^0 respectively). The signal attenuation at resonance frequency due to the MT pulse with offset frequency=500 Hz was approximately 2%. Perfusion (n=4) for multiple TRs ranging from 2.4-5 s (TR is increased by increasing the post-acquisition delay) was approximately the same (d). This shows that TR=2.4s was sufficient to refill the labeling region. The water extraction fraction for multiple TI_2 values (n=3) is shown in (e). The average extraction fraction was lower for TI_2=1 s and was almost unchanged for TI_2 >1.5 s.

Representative difference images (control (SS) – tag (NS)) without and with macromolecular saturation at TI_2 = 1.8 s are shown in Figure 3.6. Multi TI_2 ASL difference signals from the GM and the WM confirms that TI_2=1.8 s corresponds to the decaying part of the signals (Figure 3.6c) and is an appropriate choice for the protocol. A longer delay would cause a signal decay due to T_1 and reduce the SNR. Representative quantitative perfusion maps calculated using the QUIPSS II equation (Eq. 3.9) and the equation incorporating the restricted exchange and cross-relaxation (Eq. 3.5) from one subject are shown in Figure 3.6d and 3.6e, respectively. Perfusion calculation using Eq. 3.5 requires additional information, i.e., E, V, ε, T_{1t}, T_{1m}, k_f, and k_r. Previously published values E = 0.94, V=4.25%, ε=0.83 (for ATT=0.4 s), T_{1t}=2.4 s, T_{1m}=0.5 s, k_f =2.04 s^{-1}, and k_r=5.6 s^{-1} were used for this calculation[134, 135, 138, 145]. Perfusion in the GM and the WM using the QUIPSS II equation was 68 ± 7 mL/100g/min and 30 ± 5 mL/100g/min, respectively, in one representative subject. Perfusion in the GM and the WM using Eq. 3.5 was 66 ± 8 mL/100g/min and 28 ± 6 mL/100g/min, respectively, in the same subject. Eq 3.9 was used to calculate the perfusion for all the results presented below.

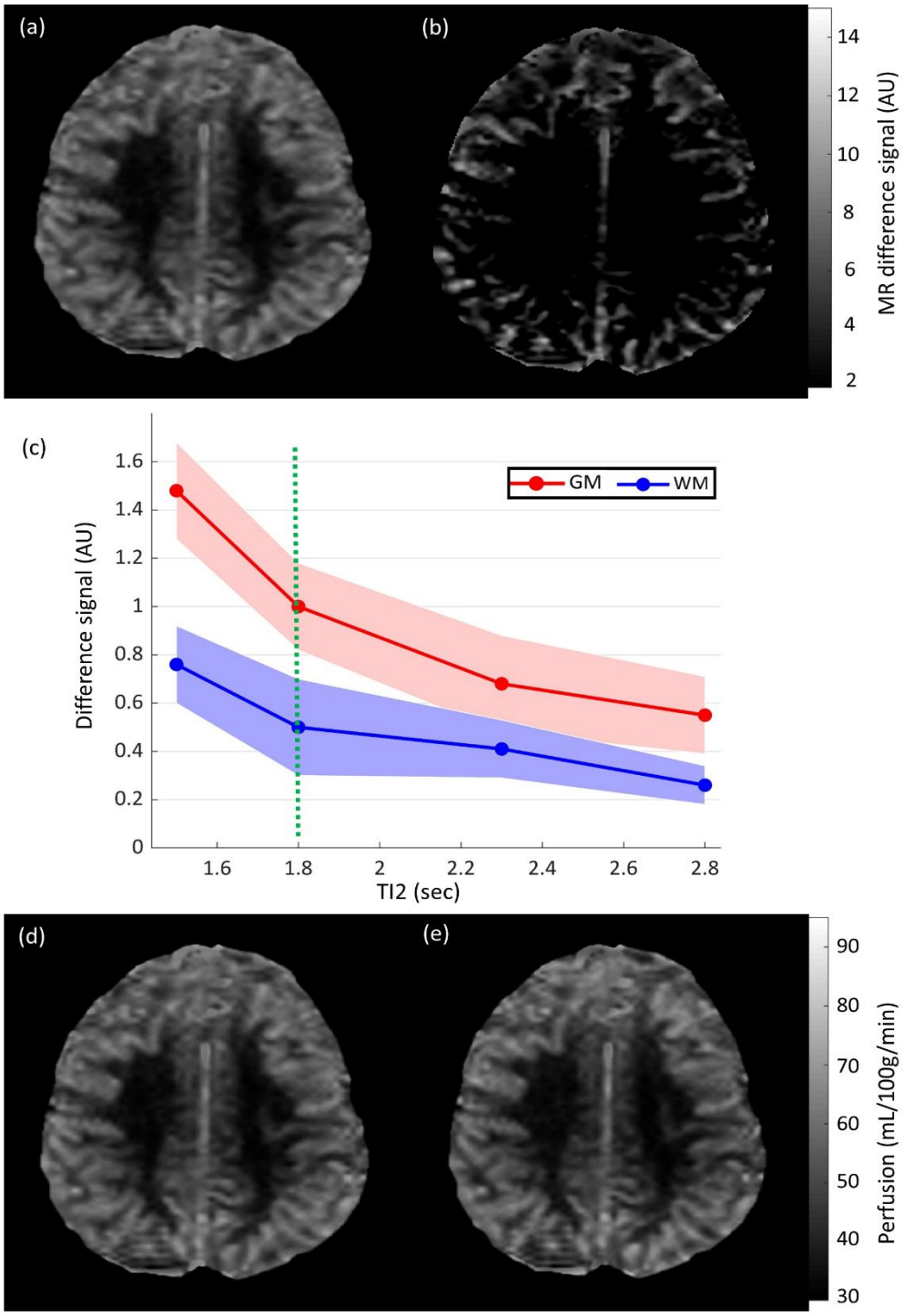

Figure 3.6: Representative ASL difference signal (SS-NS) from one subject without (a) and with (b) macromolecular saturation at TI_2=1.8 s. ASL difference signals from the GM and the WM measured at different TI_2 (c). The green dotted line corresponds to TI_2=1.8 s. All the signal values

in (c) are normalized to the GM signal at TI_2=1.8 s. Perfusion maps calculated using QUIPSS II equation (Eq. 3.9) (d) and the equation incorporating the restricted exchange and cross relaxation (Eq. 3.5) (e) from the same subject. Average GM and WM perfusion values using the two equations are very similar, suggesting the validation of Eq. 3.7 for β estimation.

We evaluated the magnetization transfer effect on the vascular blood signal (Figure 3.7), confirming that the vascular blood remains unaffected while the tissue signal experiences a significant MT effect due to the saturation of the macromolecules [122, 123].

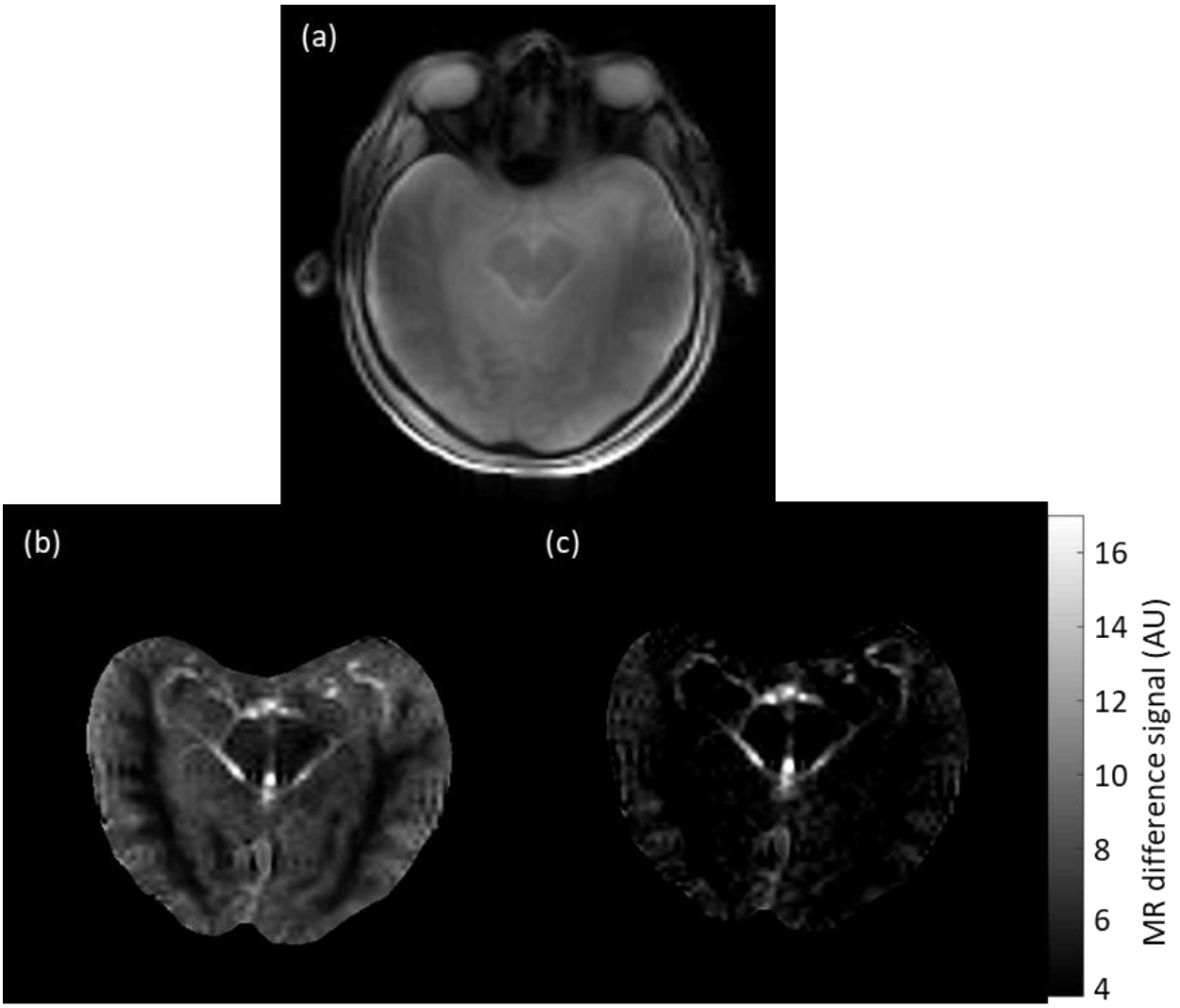

Figure 3.7: Evaluation of magnetization transfer effect on vascular blood signal due to the saturation of the macromolecules. Reference image of a slice in close proximity to the circle of Willis from a representative subject (a). Bright vascular blood signal is visible in the ASL difference signal (SS-NS) without the macromolecular saturation (b). The ASL difference signal with the saturation of the macromolecules is shown in (c). Although the tissue blood signal is reduced due to the saturation of the macromolecules, the vascular blood remains almost unaffected.

The quantitative perfusion map shows higher perfusion in the GM and lower perfusion in the WM (Figure 3.8a). Average perfusion in the GM and the WM was 67 ± 5 mL/100g/min and 29 ± 4 mL/100g/min, respectively (averaged over all healthy subjects). The water extraction fraction map shows a relatively lower fraction in the GM and higher in the WM (Figure 3.8b). Extraction fraction (E) in the WM was 0.962 ± 0.015, and extraction fraction in the GM was 0.921 ± 0.025. Permeability surface area product (PS) was 95 ± 18 mL/100g/min in the WM and 171 ± 20 mL/100g/min in the GM (Figure 3.8c). Magnetization transfer ratio (MTR) map shows higher MTR in the WM and lower in the GM (Figure 3.8d) with values of 0.17 ± 0.005 and 0.13 ± 0.015, respectively. Representative perfusion, extraction fraction, PS, and MTR maps from several additional subjects are shown in Figure 3.9.

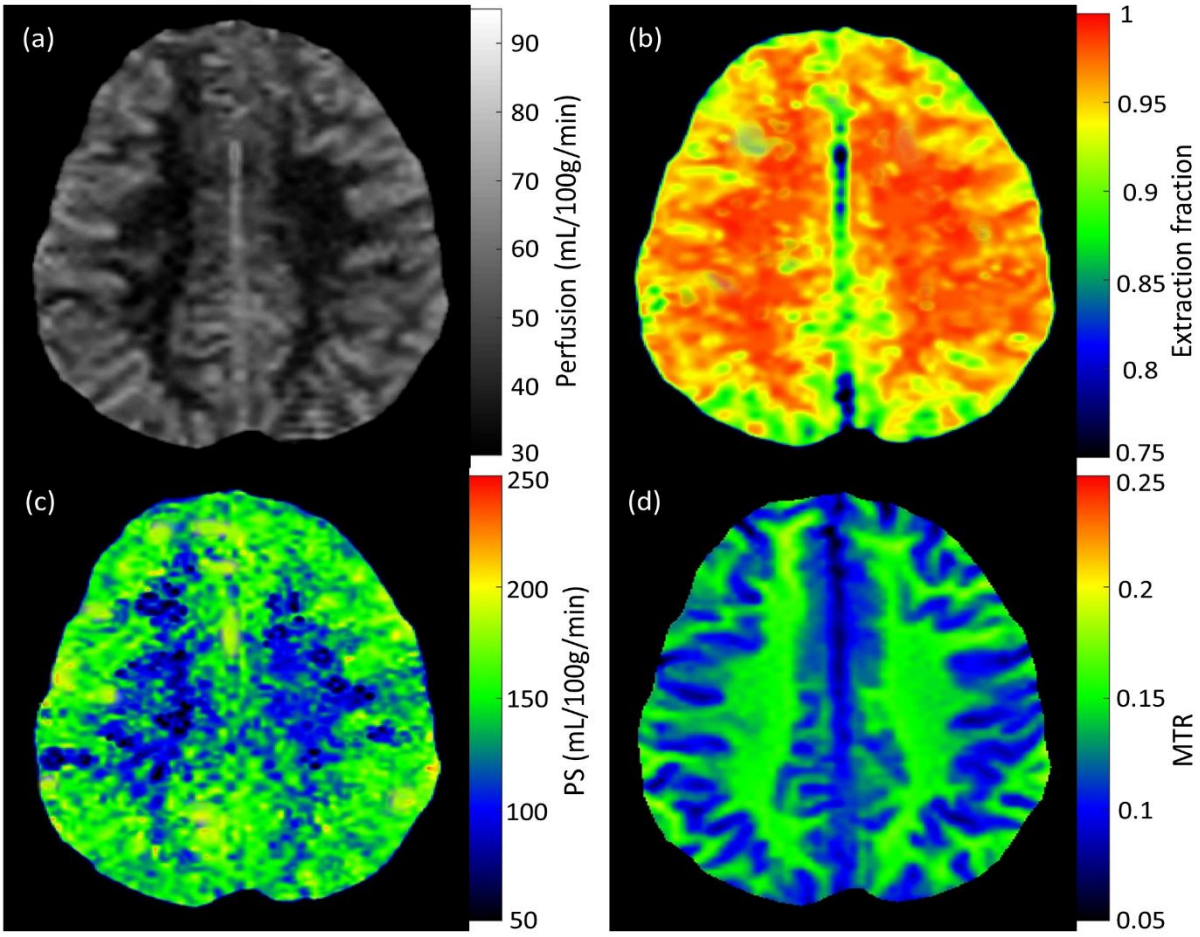

Figure 3.8: Representative (a) perfusion, (b) water extraction fraction, (c) permeability surface area product (*PS*), and (d) magnetization transfer ratio (*MTR*) maps from one subject.

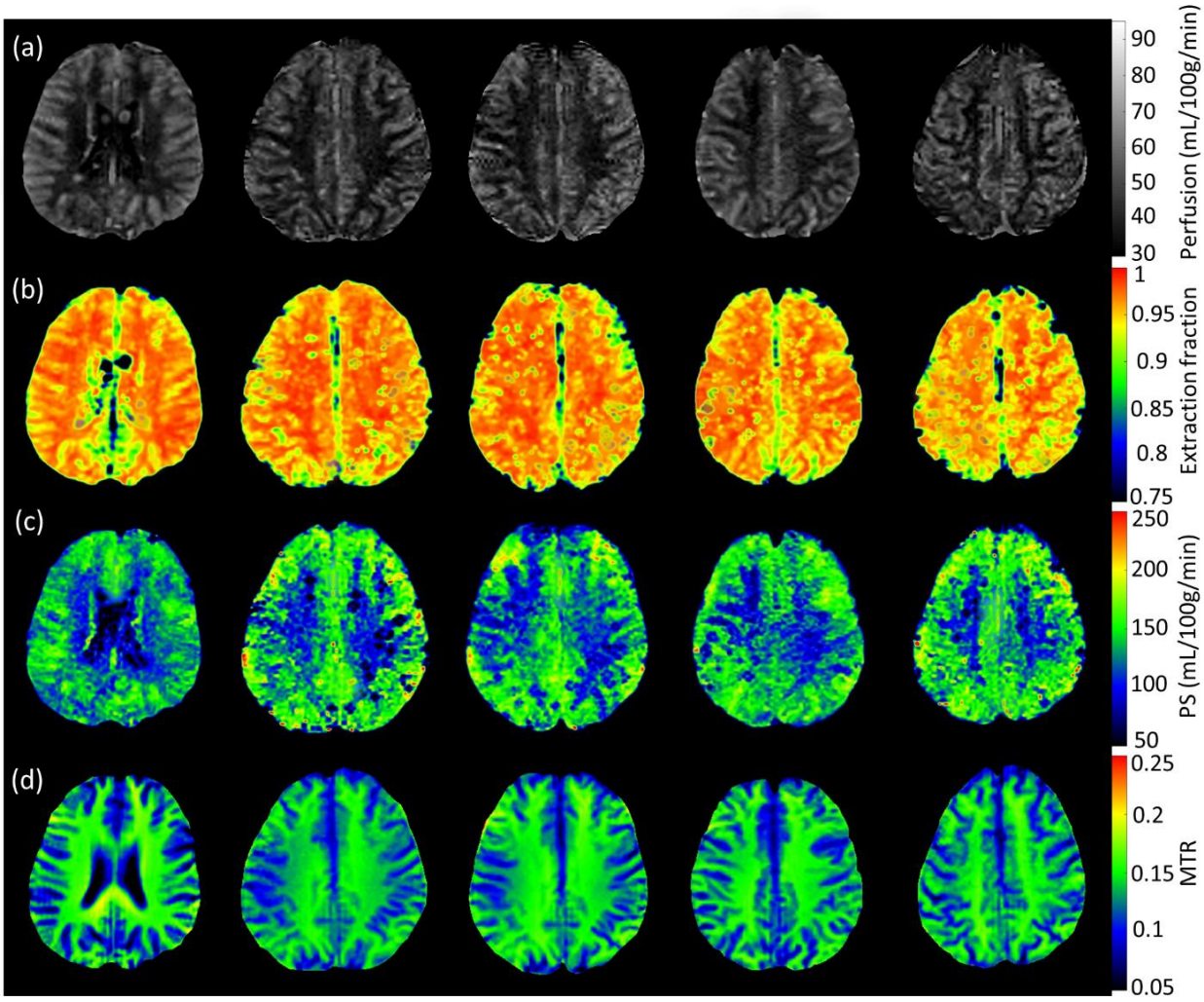

Figure 3.9: Perfusion (a), extraction fraction (b), permeability surface area product (c), and magnetization transfer ratio (d) maps from five subjects.

Bland-Altman plots for perfusion and water extraction fraction demonstrate very good agreement between test-retest results (Figure 3.10). Mean biases for perfusion and water extraction fraction were 0.62 (with a coefficient of variation=6%) and 0.009 (with a coefficient of variation=4%), respectively. Figure 3.10c shows very high correlations between perfusion and PS for the GM and the WM regions from all subject scans (r= 0.86 and 0.92 for the GM and the WM respectively). Correlations between perfusion and water extraction fraction for the GM and the WM were

relatively lower (r=-0.35 and -0.28 for the GM and the WM, respectively) (Figure 3.10d). Correlations between perfusion and PS and between perfusion and extraction fraction found in this study are consistent with previous PET and MRI studies [121, 146].

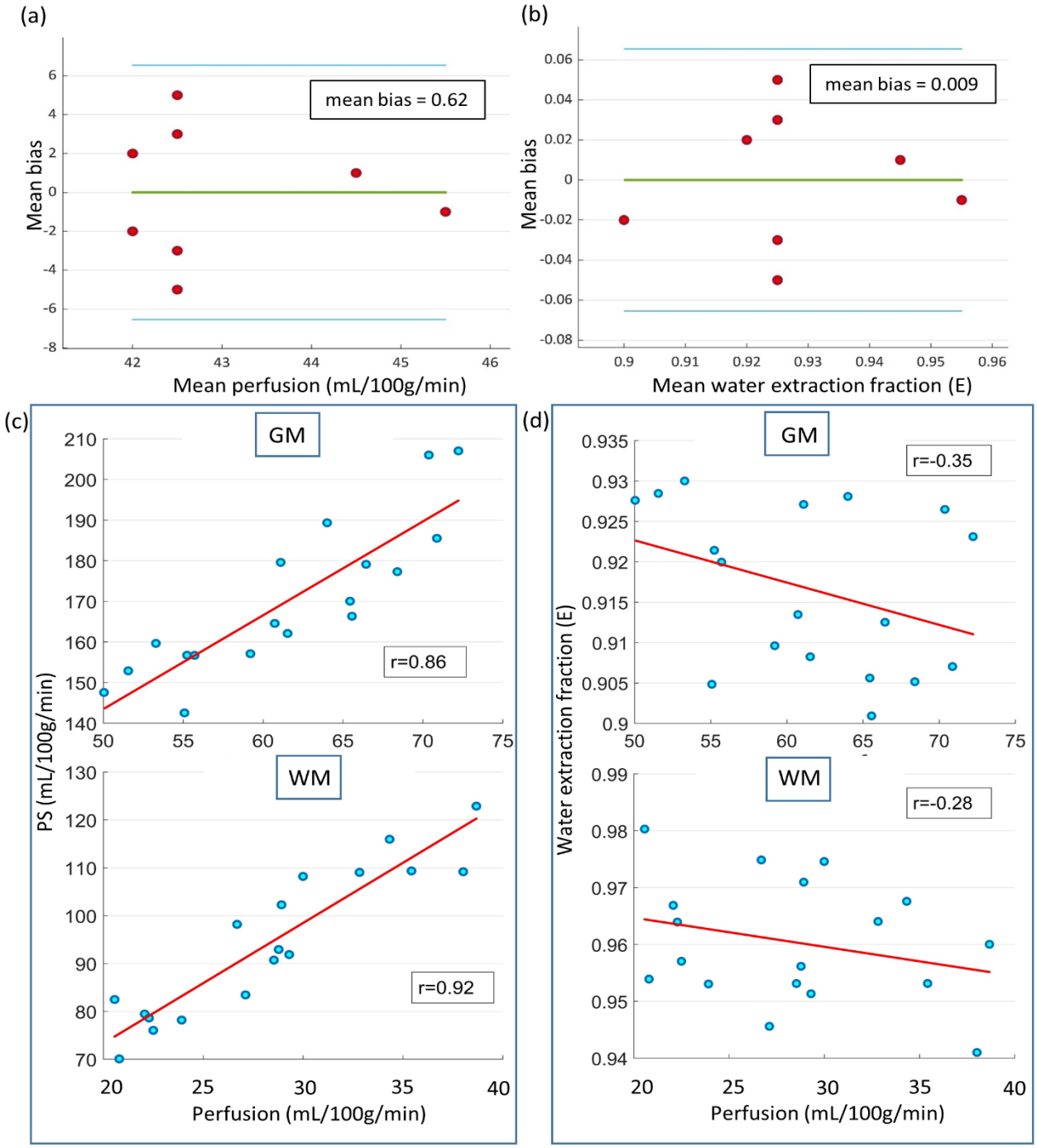

Figure 3.10: Bland-Altman plots of test-retest results for perfusion (a) and water extraction fraction (b). Correlation plots between perfusion-permeability surface area product (*PS*) (c) and perfusion-water extraction fraction (*E*) (d) for the GM and the WM regions.

Changes in perfusion, water extraction fraction, and permeability surface area product were observed due to caffeine intake (Figure 3.11). Perfusion decreased from 67±6 mL/100g/min to 50±8 mL/100g/min in the GM (p=0.007, t=3.4, df=6) and 26±7 mL/100g/min to 21±5 mL/100g/min in the WM (p=0.01, t=1.16, df=6) following caffeine intake. Extraction fraction was also reduced from 0.924±0.025 to 0.91±0.011 in the GM (p=0.08, t=1.02, df=6) and 0.958±0.016 to 0.921±0.013 in the WM (p=0.03, t=3.58, df=6) due to caffeine consumption. Permeability surface area product decreased from 172±15 mL/100g/min to 121±12 mL/100g/min in the GM (p=0.06, t=5.3, df=6) and 83±7 mL/100g/min to 54±8 mL/100g/min in the WM (p=0.02, t=5.45, df=6) following caffeine intake.

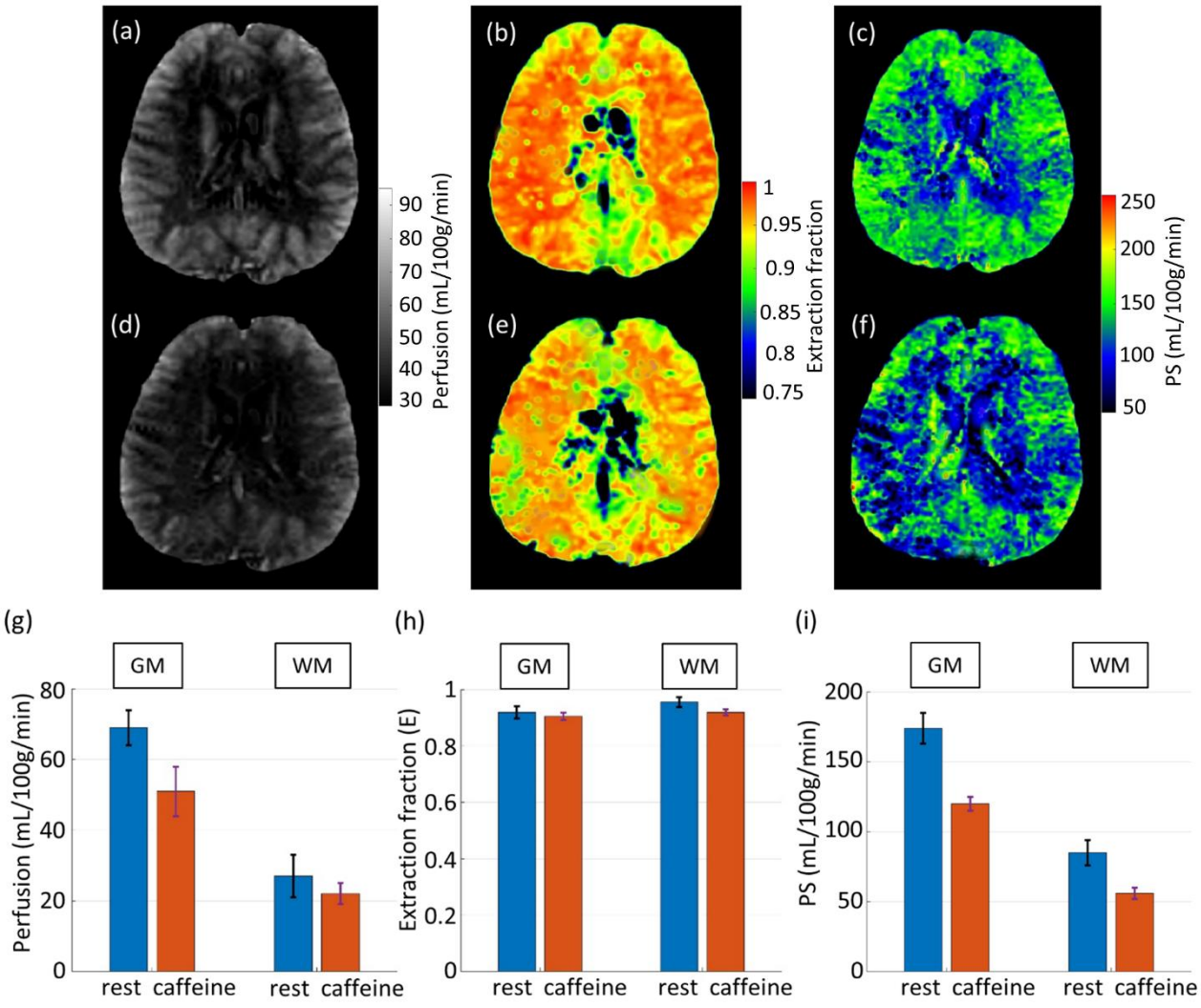

Figure 3.11: Perfusion (a), extraction fraction (b), and permeability surface area product (c) maps from a representative subject before caffeine intake. Reduced perfusion, extraction fraction, and PS were observed following caffeine intake ((d), (e), and (f), respectively). Bar plots showing the comparisons of perfusion (g), water extraction fraction (h), and permeability surface area product (i) in the GM and the WM before and after caffeine intake.

The effect of macromolecule saturation power on the water extraction fraction was verified experimentally by increasing the macromolecule saturation power, resulting in a measured MTR

of 0.23 (change of 53%), whereas the water extraction fraction only changed by 0.6%, i.e., within experimental variations (Figure 3.12).

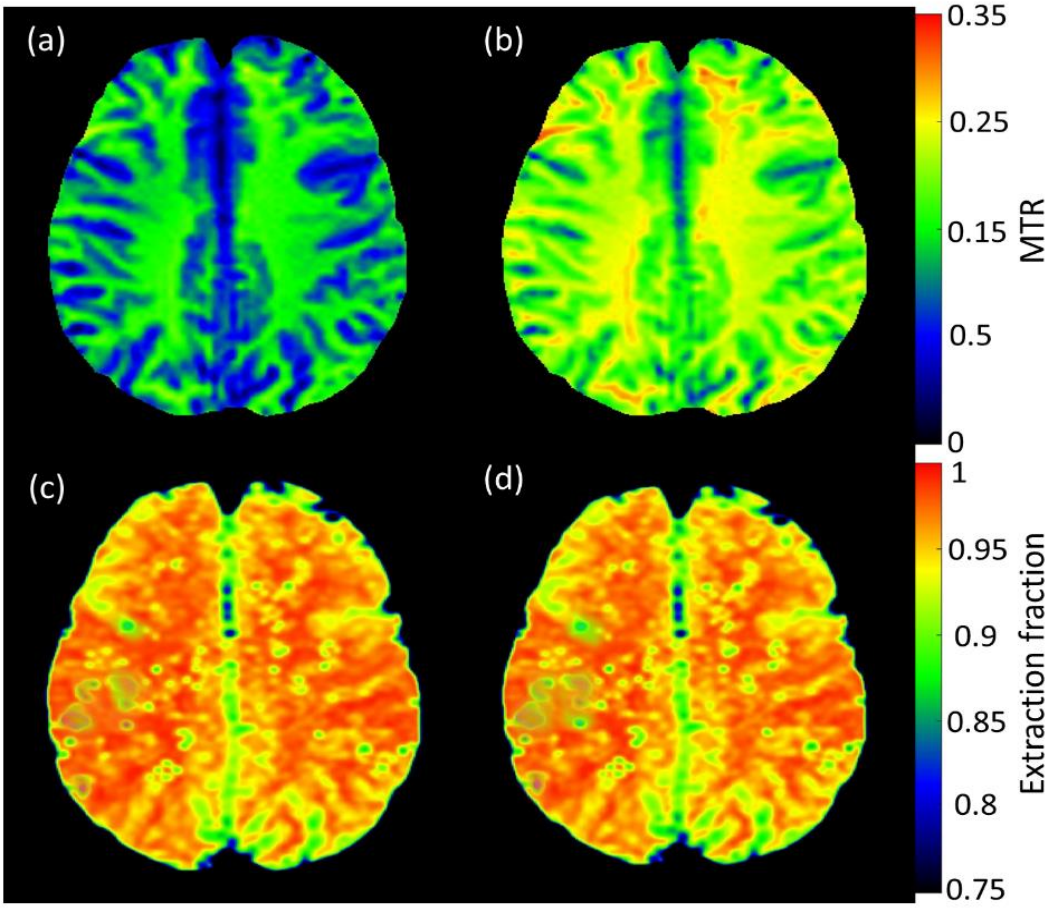

Figure 3.12: Magnetization transfer ratio maps from representative subject with MT pulse angle=500^0 (a) and 750^0 (b), showing a variation of approximately 53%. Corresponding extraction fraction maps ((c) and (d), respectively) resulted in a variation of <1%.

3.4 Discussion

In this study, we presented the theory and experimental demonstration of a non-contrast method to measure BBB permeability using the differential effect of magnetization transfer on tissue and vascular water. The feasibility and the test–retest reproducibility of the method to determine perfusion, permeability surface area product (PS), and magnetization transfer ratio (MTR) simultaneously were demonstrated in human subjects at 7T. The method was able to detect changes in perfusion due to caffeine intake (with p=0.007, t=3.4, df=6; and p=0.01, t=1.16, df=6 in the GM and the WM respectively). The ability of this method to detect changes in extraction fraction and PS following caffeine intake was also promising (with p=0.08, t=1.02, df=6 and p=0.03, t=3.58, df=6 for extraction fraction in the GM and WM, respectively; and p=0.06, t=5.3, df=6 and p=0.02, t=5.45, df=6 for PS in the GM and the WM, respectively). The measurements of the relationship between perfusion, PS, and MTR may be clinically relevant in investigating a variety of CNS disease.

The average MTR of 0.15 (i.e., ~15% saturation of the tissue signal) in this study corresponds to ~23% saturation of the macromolecules (Figure 3.4a), which corresponds to a β value of ~2.15 at 7T (Figure 3.4b). Average β measured in this study using Eq. 3.7 was ~2.21 and is in close agreement with the predicted value. The small difference in β may be attributed to systematic effects in the MRI study. The direct spillover effect of the MT pulse was measured to be <2% (Figure 3.5). Simulations (Fig. 3.4c) show that macromolecular saturation from ~90% down to ~15% should affect the calculation of extraction fraction by less than 1.4%. As macromolecular saturation increases (i.e., n decreases), the terms $\frac{S_{SSm}-S_{NSm}}{(2\varepsilon-1)S_{SSm}+S_{NSm}}$ and $\frac{1}{(2\varepsilon-1)S_{SSm}+S_{NSm}}$ increase (Eqs. 3.31, 3.32, and 3.33), whereas $\frac{S_{SS}-S_{NS}}{(2\varepsilon-1)S_{SS}+S_{NS}}$ and $\frac{1}{(2\varepsilon-1)S_{SS}+S_{NS}}$ remain unaffected in Eq. 3.8. At the same time, the scaling factor β in Eq. 3.8 decreases as macromolecular saturation increases

(i.e., *n* decreases in Eq. 3.7) to account for the increase in $\frac{S_{SSm}-S_{NSm}}{(2\varepsilon-1)S_{SSm}+S_{NSm}}$ and $\frac{1}{(2\varepsilon-1)S_{SSm}+S_{NSm}}$. Combined, these effects are somewhat compensatory and lead to accurate determination of the extraction fraction for a reasonable range of macromolecular saturation. This was also verified experimentally by increasing the macromolecule saturation power, resulting in a measured MTR of 0.23 (change of 53%), whereas the water extraction fraction only changed by 0.6%, i.e., within experimental variations (Figure 3.12). However, our simulations also demonstrate that, when macromolecular saturation decreases below 10%, the error increases exponentially. This is because the model developed here relies on the fact that macromolecules are saturated, and as the saturation approaches zero, the model is no longer valid. One advantage of selecting higher macromolecular saturation is that the difference signal $S_{SSm} - S_{NSm}$ (Eq 3.7) increases with higher macromolecular saturation, thus improving the signal to noise ratio. Our results show that it is advisable to keep macromolecular saturation above 15-20%. However, increased power of MT pulses can lead to SAR limitations, especially at 7T.

Several experimental protocol parameters can affect the calculations and need careful consideration. We evaluated the magnetization transfer effect on the vascular blood signal (Figure 3.7), confirming that the vascular blood remains unaffected while the tissue signal experiences a significant MT effect due to the saturation of the macromolecules [122, 123]. The TR (2.4s) used in this study was sufficient to refresh the labeled spins with the FAIR ASL pulse sequence. This was confirmed by repeating the experiment (n = 4) at multiple TRs ranging from 2.4 – 5 s (by increasing the post-acquisition delay). All other acquisition parameters were kept the same. The calculated perfusion both in the GM and the WM was approximately the same for this range of TR (Figure 3.5).

RF inhomogeneities in the labeling pulse can impact the perfusion measurements, and it has been recommended to use adiabatic RF pulses, which are insensitive to B_1 inhomogeneities [147, 148]. We used a hyperbolic secant adiabatic inversion pulse, which is insensitive to the B_1 field inhomogeneity and provides good inversion efficiency. We have previously measured the experimental slice profile and inversion efficiency of this pulse at 7T [79]. In addition, a proton density-weighted reference image is used for the scaling of the perfusion signal in the ASL experiment. Both these effects largely correct RF field inhomogeneities[112] during excitation and acquisition and in general does not need additional correction. Parallel transmission can further help reduce any RF field inhomogeneities, but it was not used in this study.

Another important experimental concern is the appropriate choice of TI_2 so that the labeled blood is exchanged with the tissue. We evaluated the water extraction fraction at multiple TI_2 values ranging from 1 – 3 s (resulting in a TR of 1.6 – 3.6 s) in three subjects (Figure 3.5). For a short TI_2 (i.e., 1 s), the average extraction fraction was lower. This is expected because short TI_2 does not allow the tagged blood to reach the capillary exchange site and fully exchange with the tissue. For TI_2 >1.5 s (corresponding TR>2.1 s), the average extraction fraction did not change and was in the range of experimental variations (Figure 3.5).

Arterial transit time (ATT) may vary depending on the distance between the labeling region and the imaging region in different ASL approaches (i.e., CASL/pCASL, PASL) and due to physiological reasons (i.e., diseases), which, in turn, will affect the quantification of the extraction fraction. ATT = 0.4 s was used for FAIR to calculate the factor ε in this study. Typical transit times for blood in capillaries are ~1 s. The fact that the extraction fraction in our multi-TI_2 experiments did not change for TI_2 >1.5 s confirms that the ATT was ~0.5 s, which is very close to the assumed ATT (0.4s). Any value in the expected ATT range for FAIR (0.4-0.9 s) results in a variation of

~1% for the extraction fraction as long as TI_2 is selected in the appropriate range. If there is no reason to expect a drastic change in the ATT, using the expected value of ATT should be sufficient by selecting TI_2 in the reasonable range [112, 137]. However, in cases where a large change in ATT is expected or a very precise calculation is required, ATT can be determined from multi-TI_2 ASL acquisitions at the cost of additional acquisition time.

The perfusion values measured in this study for the GM and the WM are in good agreement with previous studies [111, 124, 149-151]. Water extraction fractions for the GM and the WM are also consistent with the numbers reported previously ranging between 90-96% [21, 117, 146, 152]. The average permeability surface area product is also in agreement with the previously reported values ranging between 133-199 mL/100g/min [18, 21, 117, 153]. Test-retest analysis showed a very good agreement, validating the consistency of the developed technique.

Reductions in perfusion following caffeine intake are consistent with previous studies [136, 154]. Changes in the BBB permeability due to caffeine intake are also in close agreement with previous reports [121, 155-159]. Caffeine is an adenosine receptor antagonist and inhibits phosphodiesterases (PDEs) [160]. A_{2A} adenosine receptor antagonist administration reduces the BBB permeability to dextrans and Evan's blue dye in the rat chronic sleep restriction model [161]. Inhibition of cyclic adenosine monophosphate (cAMP) PDE in the collecting duct of kidneys has been shown to reduce water permeability [162]. Caffeine has been shown to attenuate the BBB permeability through the blockade of adenosine receptors and cAMP PDE inhibition [157]. In other studies, it was shown that caffeine ingestion can decrease the tight junction protein level and mitigate the BBB leakage to Evan's blue dye [156, 158]. It has also been demonstrated that caffeine causes upregulation of P-glycoprotein (P-GP) at the BBB and reduces the BBB leakage [159]. Reduced BBB permeability to harmine due to caffeine was reported in rats [155]. A decrease in K^+/Na^+-ATPase in rat kidneys

following caffeine administration has been reported previously [163], which is linked to the transmembrane water exchange [164, 165]. Reduced BBB permeability surface area product was also found in human studies following caffeine challenge [121]. These studies support our observation of reduced PS. The decrease in perfusion observed in this study was significant both in the GM and the WM. Although the change in extraction fraction and PS in the WM was significant, it was not significant at $p<0.05$ level in the GM. Caffeine causes vasoconstriction and hence changes the CBF and the CBV, which can complicate calculations. We used a simple relationship to calculate the CBV due to a change in the perfusion following caffeine intake. Although this relationship has been found to provide good results for hypocapnia (vasoconstriction), hypercapnia (vasodilation), and visual stimulation [139-141], a more accurate relationship between the perfusion and the CBV might improve the accuracy of the quantification of water extraction fraction. A change of 2% in the ATT has been reported following caffeine intake [121], which should not affect the quantification of the extraction fraction, as discussed above.

The restricted movement of water between the vascular blood and the tissue in the central nervous system, as measured in this study, also supports previous physiological reports [18, 19]. The permeability of the capillary wall to water molecules is affected by two physiological processes: water filtration and water diffusion. While diffusion refers to the passage of water molecules across the capillary wall because of Brownian motion, filtration refers to the motion due to the osmotic pressure gradient. Slits and pores between endothelial cells play an important role in water filtration in capillaries outside the central nervous system because bulk flow can take place across the capillary wall through these slits and pores. However, they have very little contribution to water diffusion because the total surface area of these pores and slits is very small compared to the total capillary surface area. The water channels (aquaporin) have a diameter on the order of a single

water molecule in the central nervous system. Therefore, these channels only permit water diffusion but not water filtration. While the ratio between the filtration and the diffusion is fifty or more outside the central nervous system (i.e., muscle), it is close to unity in the nervous system.

There are very few existing clinically applicable techniques to measure BBB water permeability non-invasively. PET imaging relies on the infusion of a tracer, which is assumed to be freely diffusible across vasculature. [^{11}C] butanol and [^{15}O] water radiotracers have been used with PET imaging to measure BBB permeability [146, 153]. Intravascular T_1 contrast agent has been used with MRI to estimate vasculature water permeability [105, 166, 167]. However, these methods have not been used widely in clinical applications due to model and methodological complexities.

Few non-contrast MRI techniques to estimate BBB permeability and water exchange rate have been recently demonstrated. The water exchange rate constant can be measured by applying a two-compartment model to ASL signals at multiple post-labeling delays [16, 115]. However, the intrinsic SNR of this method is limited as it depends on the T_1 relaxation difference before and after the exchange of water molecules [168]. Another approach used T_2 relaxation time to differentiate the blood and the tissue ASL signal [114, 116]. The oxygenation changes due to the flow of spins from the artery to the capillary to the vein can also lead to alteration in T_2 and confound the results. A variable flip angle method in combination with contrast agent administration was demonstrated to measure a water exchange index in mice [169], which used protected graft copolymer bearing covalently linked Gd-DTPA residues (Gd-PGC) as the contrast agent.

Diffusion-weighted ASL signal acquisition has shown promising results to separate the fast-moving spin and the slow-moving spin, corresponding to the vascular and the tissue water signal, respectively [118-121]. This method assumes that the diffusion gradient can fully suppress the vascular

signal while having no effect on the tissue signal. This technique also assumes that the vascular water signal has no slow-moving component, but some studies have shown the presence of slow-moving components in the vascular water in rat brains [170, 171]. Another approach to measure the BBB permeability is phase contrast arterial spin tagging [172]. This technique can only measure the global permeability without any spatial information.

Besides perfusion and PS, the effect of MTR in CNS WM diseases, such as multiple sclerosis, has been reported [173], and therefore, MTR can be a valuable non-invasive biomarker in WM diseases. WM lesions in CNS diseases, such as MS, are characterized by a large drop in the MTR due to demyelination [125]. MTR depends on the macromolecular concentration and is usually higher in the WM due to the high concentration of macromolecules like protein and lipids present in the myelin sheath. Demyelination causes this macromolecular concentration to drop and consequently decreases the MTR. Although MTR is very useful in assessing such diseases, there is no standard value for MTR since it depends on the degree of macromolecular saturation. However, using the same MT protocol for control subjects and patient populations would be an effective way to assess the difference.

There are several limitations to our approach. Currently, we have demonstrated only 2D imaging, but this approach can be extended to 3D imaging for full brain coverage. Although we have shown that the approach is sensitive to changes in perfusion and water exchange using caffeine challenge, it needs to be determined if this can detect subtle focal changes in blood-brain barrier disruption in diseases without much CBF change. Another limitation of the model presented here is the choice of the arterial input function. Although accurate for the CASL experiment, the input function is not exact for the PASL FAIR experiment [129]. We have used the mean ATT to approximately scale the arterial bolus; however, this approach may lead to a bias in the calculated parameters. An

advantage of this simplified approach is that it allows us to use the simple Bloch-equation approach to demonstrate the feasibility of the technique. A more complete model would include exponentially decaying input function, residue function, the effect of the dispersion, and other confounding factors [129, 174]. These refinements can improve the accuracy of the measurements, and more work is required in this area. Future studies can relax the assumptions made here and improve the accuracy of the technique. Another limitation is that the QUIPSS II approach was employed to define the bolus duration. An alternate approach, such as Q2TIPS [175], may be used to improve the saturation of the labeled spins. Careful optimization of the MT pulse can further improve the quantification. Although the test-retest results demonstrated excellent reproducibility, a limitation was that the subjects were not removed from the scanner between the test-retest scans. Hence, it does not account for all sources such as shimming, B_1, etc. when determining the reproducibility measures. This approach was demonstrated at 7T, but it should be very similar for lower field MRIs, such as 1.5T or 3T with optimization of the imaging parameters, such as inversion and saturation pulses, MT pulse, PLD, etc.

In summary, in this study, we demonstrated that measurement of ASL signal with and without magnetization transfer effect can be used to estimate permeability surface area product along with perfusion and MTR. Measurement of BBB permeability can provide valuable information about BBB disruptions in pathology, and simultaneous co-registered MTR measurements can provide information about the tissue structural damage, such as demyelination.

Chapter 4

High-Resolution ^{1}H FID Rosette Spectroscopic Imaging (RSI) of the Human Brain at 7T

4.1 Background

Magnetic resonance spectroscopic imaging (MRSI) is a powerful technique to evaluate the spatial distribution of brain metabolites. The metabolic maps can provide important information in diagnosing central nervous system (CNS) pathology such as Alzheimer's disease, schizophrenia, frontotemporal dementia, etc. [36, 37].

MRSI can greatly benefit from ultra-high field (UHF) strength (≥7T) with higher chemical shift dispersion, SNR, and spectral resolution [176-178]. Among the common ^{1}H MRSI sequences, slice-selective ultra-short TE ^{1}H free induction decay (FID) MRSI is fast, offers a high signal-to-noise ratio (SNR), has low chemical shift displacement, and can detect metabolites with short T_2* [177, 179-181]. However, for traditional MRSI methods, which use only the phase encoding (PE) technique, the total acquisition time can be very lengthy as it samples a single k-space position per repetition time (TR). Several approaches have been demonstrated to accelerate MRSI at UHF using parallel imaging (PI), such as GRAPPA, SENSE, or CAIPIRINHA [181-184]. However, the acceleration factors for PI techniques are limited by the SNR of the spectra and the g-factor-related noise amplification. Additionally, the acquisition of the calibration data can also increase the scan time, thus reducing the actual acceleration factor. Compressed sensing (CS) is another approach to accelerate MRSI by recovering the missing data from an undersampled k-space using the sparsity

property of MR signals [185, 186]. For ^{1}H MRSI, CS has mostly been applied to accelerate localized and lipid-suppressed sequences [187-189]. However, for non-lipid suppressed ^{1}H FID MRSI, CS reconstruction is extremely challenging because of the low SNR of the metabolite signals compared to the high SNR of the lipid signal [179, 190].

High acceleration for MRSI can also be achieved using the spatial-spectral encoding (SSE). Along with Cartesian SSE techniques, such as echo-planar spectroscopic imaging (EPSI), non-Cartesian SSE techniques to accelerate MRSI using spiral spectroscopic imaging (SSI) and rosette spectroscopic imaging (RSI) have been developed [47, 191, 192]. Compared to EPSI and SSI, RSI can achieve higher spectral bandwidth (SBW) under similar slew rate and gradient strength constraints [48, 193]. In addition, unlike flyback EPSI and spiral-out-only SSI, RSI does not suffer from loss of sensitivity as data is collected and used for the entire signal decay readout [48, 193, 194]. RSI is also preferred over SSI and EPSI at UHF (≥7T) [195]. Rosette trajectories are compelling because of smoothly varying gradient waveforms and flexible trajectory design [46-48]. Another benefit of the rosette trajectory is that it can be more incoherently undersampled compared to other non-Cartesian trajectories, which makes it a perfect candidate for CS applications [195, 196].

Although in vivo brain ^{1}H RSI has been demonstrated at lower field strength (≤3T) [48, 197, 198], to our knowledge, only one previous study demonstrated ^{1}H RSI on the human brain at 7T with 4mm in-plane resolution using LASER excitation and outer volume suppression targeting the skin/skull for lipid suppression [193], which can potentially increase the TR and specific absorption rate (SAR), especially at UHF [176, 195]. At UHF, ^{1}H FID MRSI can overcome the limitations of SAR, B_1 inhomogeneity, chemical shift displacement error (CSDE), and T_2-weighting [179, 195]. The purpose of this study was, therefore, to demonstrate the feasibility of non-lipid suppressed ^{1}H FID RSI on the brain with 2 mm in-plane resolution at 7T.

4.2 Materials and Methods

4.2.1 Rosette trajectory design

Rosette trajectories oscillate in the radial direction about the origin of k-space with angular frequency $\omega_1 = 2\pi f_1$, simultaneously rotating in the k_x-k_y plane with angular oscillation frequency $\omega_2 = 2\pi f_2$. The k-space trajectory is given by [46-48]

$$k(t) = k_{max}\sin(\omega_1 t)e^{i\omega_2 t} \quad 4.1$$

where $k_{max}=N_x/(2.FOV)$ is the highest spatial frequency sampled, N_x is the matrix size and FOV is the field of view. The angular frequency can be written as $\omega_1 = \pi\frac{SBW}{n_{TI}}$, where SBW is the spectral bandwidth and n_{TI} is the number of temporal interleaves. The oscillation frequency ω_2 can have any value between 0 and ω_2^{max}, where ω_2^{max} is limited by the maximum slew rate (S_{max}), maximum gradient (G_{max}), or the Nyquist constraint along the readout trajectory: $\gamma.FOV.G_{max} + SBW \leq 1/dt$, where dt is the data sampling rate, and γ =42.57 MHz/T is the ^{1}H gyromagnetic ratio [47, 48]. Maximum gradient and slew rate for the rosette trajectory can be calculated from [47, 48]

$$G_{max} = k_{max}\frac{\max(\omega_1, \omega_2)}{\gamma} \quad 4.2$$

$$S_{max} = k_{max}\frac{(\omega_1^2 + \omega_2^2)}{\gamma}$$

We chose $\omega_1 = \omega_2$ for constant maximum gradient strength throughout the readout, which results in a circular trajectory for a single shot [48] (Figure 4.1). The corresponding gradient was calculated

using $G(t) = \frac{2\pi}{\gamma}\frac{dk(t)}{dt}$ [46-48]. Total number of shots to fully sample the k-space based on the intended image resolution was [48]

$$N_{sh} = \frac{\pi N_x}{2} \tag{4.3}$$

The rosette trajectory for optimum number of shots using Eq 4.3 for the 1st interleave is shown in Figure 4.1.

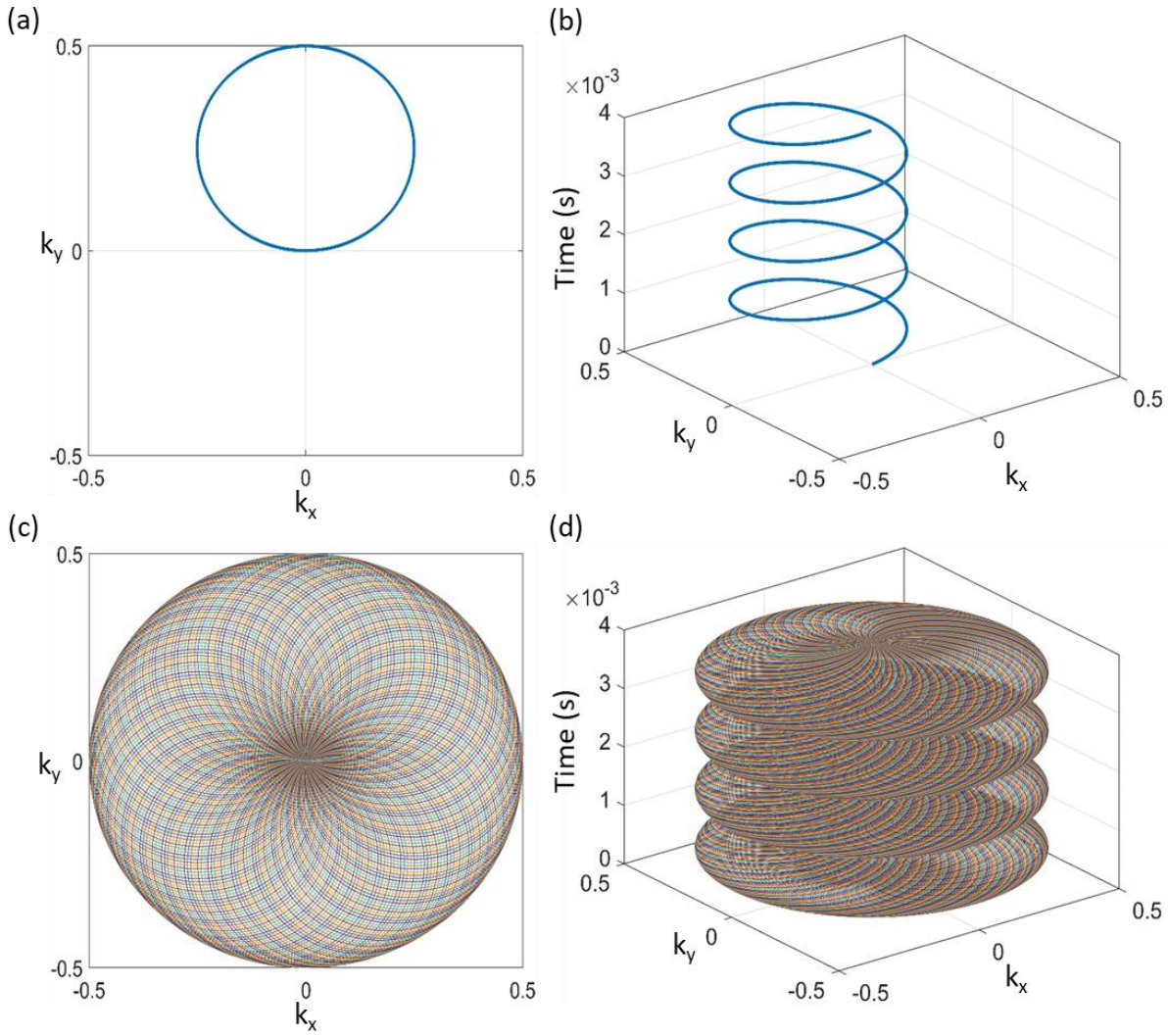

Figure 4.1: Rosette k-space trajectory (a) and k-t-space trajectory (b) for a single shot with FOV=256×256 mm^2, matrix size=128, in-plane resolution=2×2 mm^2, $\omega_1 = \omega_2 = 1000\pi$ rad/s, SBW=3000Hz and n_{TI}=3. Only the 1st interleave is shown in (a) and (b). The effective spectral dwell time for (a) and (b) is n_{TI}/SBW=1 ms. Corresponding k-space (c) and k-t-space (d) trajectories for 202 rosette shots (number of shots calculated by Eq 4.3).

4.2.2 Recruitment

The study was approved by the Auburn University Institutional Review Board (IRB). All experiments were performed according to the IRB guidelines and regulations. In vivo ^{1}H FID RSI data were collected from brains of 5 healthy volunteers (age=41±13 years, weight=73±11 kg). All participants provided informed consent prior to participation in the study. None of the participants had any history of neurological disease.

4.2.3 Imaging protocol

All the experiments were performed using a Siemens 7T Magnetom (Erlangen, Germany) using 32 channel head coil. The peak gradient and slew rate of the scanner were 70 mT/m and 200 mT/m/ms, respectively.

Suppression of the water signal is necessary for ^{1}H MRSI as the water signal is orders of magnitudes higher than the metabolite signals. Water suppression enhanced through T_1 effects (WET) is a common approach to diminish the water signal [199]. WET has been adapted for ^{1}H FID MRSI at UHF in previous studies [200]. We optimized the three-pulse water suppression scheme for water suppression in our study, similar to the previously reported scheme [200]. Three pulses, each with bandwidth of 120 Hz, duration of 8 ms, and flip angles of 90^0, 79.5^0 and 159^0, respectively,

were used for water suppression. Inter-pulse delay between the three water suppression pulses and the delay between the last water suppression pulse and the excitation pulse were all 20 ms.

Standard second-order B_0 shimming has been successfully used for ^{1}H MRSI at UHF [177, 182, 200], which was also used on a rectangular shimming volume (with dimensions similar to the imaging volume) iteratively using the vendor provided B_0 shim routine in this study. The schematic of the RSI pulse sequence is shown in Figure 4.2. Following three WET water suppression pulses as described above, a slice-selective sinc excitation pulse with duration=0.6 ms and flip angle=45^0 was applied. The single-slice ^{1}H FID RSI acquisition parameters were: FOV=256×256 mm^2; matrix size, N_x=128; in-plane resolution= 2×2 mm^2; slice thickness=10 mm; number of rosette shots, N_{sh}=202; acquisition delay, TE=1.5 ms; TR=500 ms; SBW=3000 Hz; number of temporal interleaves, n_{TI}=3; rosette oscillation frequencies, $\omega_1 = \omega_2 = 1000\pi$ rad/s; data sampling rate, dt=2μs; spectral data points=732. This entire RSI data acquisition time was approximately 6 min. Following the RSI data acquisition, a water reference was acquired with the same acquisition protocol as the RSI with the water suppression pulses turned off for eddy current correction and multichannel spectroscopic data combination by matching image calibration data (MUSICAL) [201, 202].

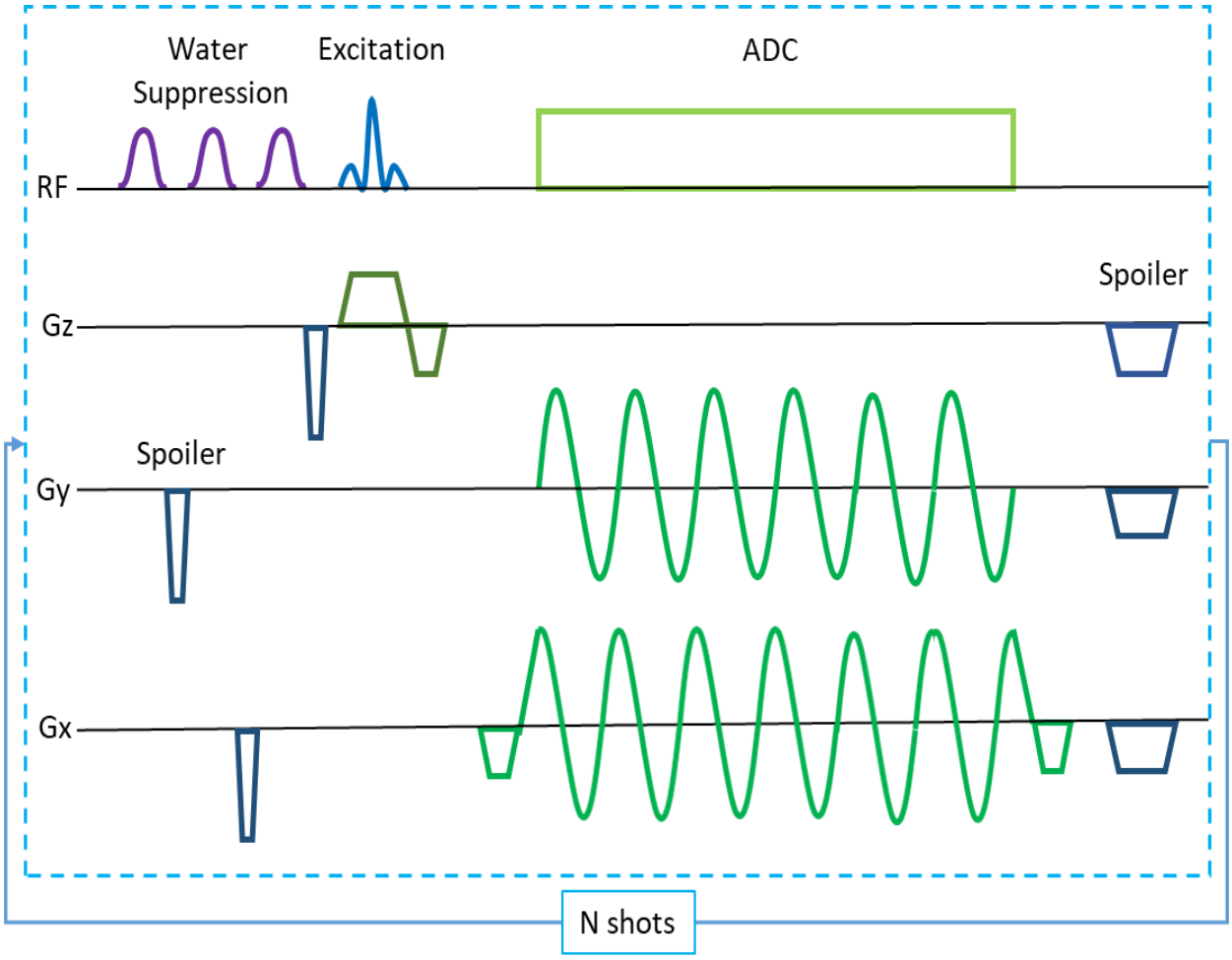

Figure 4.2: Schematic of the pulse sequence for rosette spectroscopic imaging. Three WET water suppression pulses were applied to suppress the water signal. Following the water suppression pulses, a slice selective sinc excitation pulse was used to excite the imaging slice. Gy and Gx are the rosette gradients in the phase encoding and readout directions, respectively. Note that Gy starts from zero and ends at zero, while Gx starts from the maximum value and ends at the same value. Therefore, ramp-up and ramp-down were used at the beginning and end of Gx. After the acquisition of RSI data for each shot for each interleave, spoiler gradients were applied in slice encoding, phase encoding, and readout directions. This sequence was repeated for N number of rosette shots to fill up the k-space.

4.2.4 Data processing

Data processing was performed offline using MATLAB (MathWorks, Natick, MA) and LCModel [203]. Variation in the rosette trajectory due to the magnetic field inhomogeneity was corrected using an estimated linear field map [204]. A linear phase correction was applied to compensate for the different acquisition times of each sample along circular rosette trajectory [205, 206]. Then the RSI data for each channel was reconstructed using gridding on a two-fold oversampled grid with a Kaiser-Bessel kernel window W=4 [207] and density compensation was applied [208]. A 2D Hamming filter was applied in the xy direction and a 1D Hamming filter was applied to the z (time) direction, which improves the SNR and increases the accuracy of LCModel quantification [48]. Data from individual channels were combined using the MUSICAL approach [201, 202]. Channel combined RSI data from all the voxels were then fed to the LCModel for automatic quantification of the metabolites in the range of 1.8-4.2 ppm [203]. Possible lipid contamination of the RSI data was removed using L_2-regularisation [209].

As a result of an acquisition delay (i.e., TE=1.5 ms), the first points of the FID were lost, which introduced a first-order phase error. To account for this, an acquisition delay of 1.5 ms was also incorporated in the simulation of the LCModel basis set. Using this technique, the LCModel is able to quantify metabolites even if the phase of the spectrum is negative [176, 177]. The basis set for the LCModel quantification was created with the FID-A toolbox using the same parameters as in vivo ^{1}H FID RSI protocol [210]. The basis set contained these brain metabolites: N-acetyl-aspartate (NAA), N-acetyl-aspartyl glutamate (NAAG), creatine (Cr), phosphocreatine (PCr), phosphorylcholine (PCh), glycerophosphorylcholine (GPC), γ-aminobutyric acid (GABA), glutamine (Gln), glutamate (Glu), myo-inositol (mI), scyllo-inositol (Scyllo), taurine (Tau), aspartate (Asp), and glutathione (GSH) (Figure 4.3). For the fitting of the metabolites by LCModel,

Cramer-Rao lower bounds (CRLB) <20% were considered acceptable. Metabolite maps obtained by the LCModel were displayed using custom written MATLAB software.

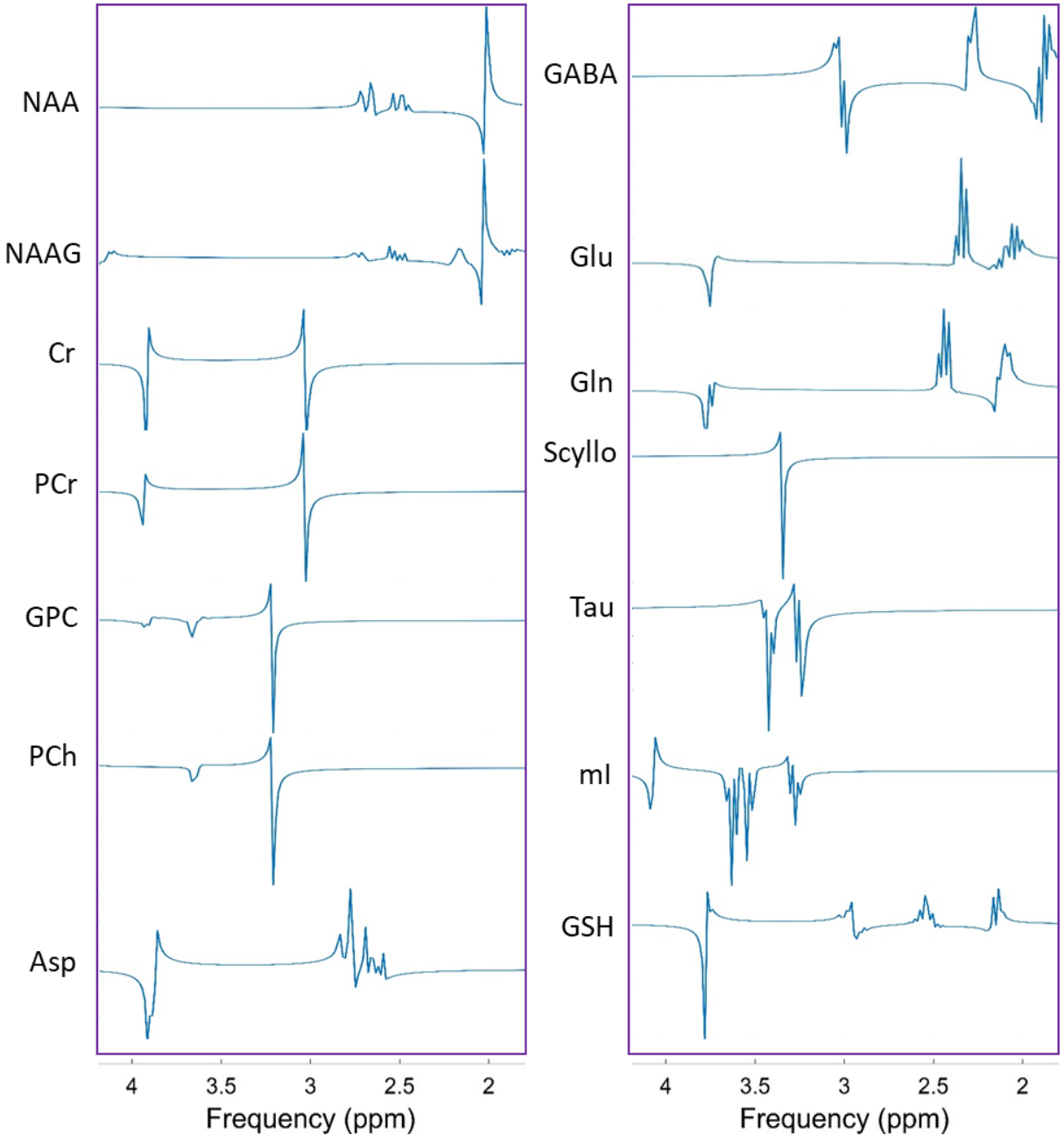

Figure 4.3: Brain metabolites simulated using FID-A with acquisition delay (TE)=1.5 ms for the basis set of LCModel are shown in the frequency range of 1.8-4.2 ppm. N-acetyl-aspartate (NAA), N-acetyl-aspartyl glutamate (NAAG), creatine (Cr), phosphocreatine (PCr),

glycerophosphorylcholine (GPC), phosphorylcholine (PCh), aspartate (Asp), γ-aminobutyric acid (GABA), glutamate (Glu), glutamine (Gln), scyllo-inositol (Scyllo), taurine (Tau), myo-inositol (mI), and glutathione (GSH) metabolites were included in the basis set.

4.3 Results

The maximum gradient and slew rate for the rosette trajectory were 18.45 mT/m and 115.9 mT/m/ms, respectively. Our design for the rosette trajectory resulted in this constant maximum gradient and slew rate throughout the entire readout.

The non-water suppressed image quality of the rosette sequence compared to Cartesian (FLASH) sequence is shown in Figure 4.4. Both images were acquired with same in-plane resolution (2×2 mm^2, with FOV=256×256 mm^2 and matrix size=128×128) on the same slice location from the same subject. The magnetic field inhomogeneity is less severe in the rosette image compared to the Cartesian image. The rosette image also shows improved contrast between the GM and the WM compared to the Cartesian image.

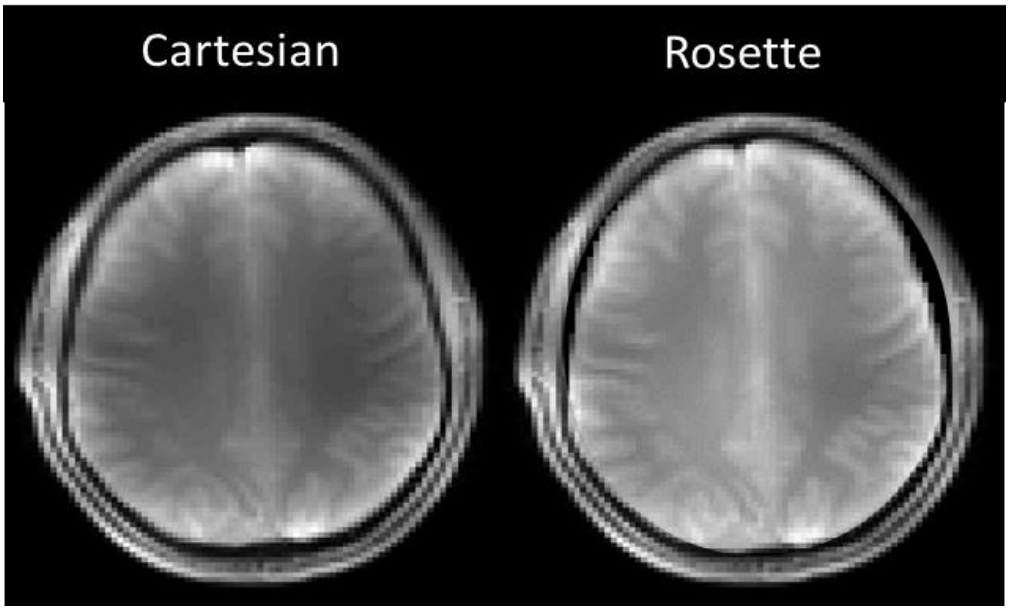

Figure 4.4: Comparison of a representative non-water suppressed rosette image with a Cartesian (FLASH) image. Both images were acquired from the same slice location of the same subject with in-plane resolution=2×2 mm^2 (FOV=256×256 mm^2 and matrix size=128).

The water suppression scheme achieved an average suppression of 98.87% of the original peak. Figure 4.5 shows representative spectra and corresponding LCModel fittings in two voxels from the white matter (WM) and the gray matter (GM) regions from a subject. Spectra from the GM voxel, which is very close to the skull/skin, demonstrates that the L_2-regularized lipid removal resulted in an effective lipid suppression.

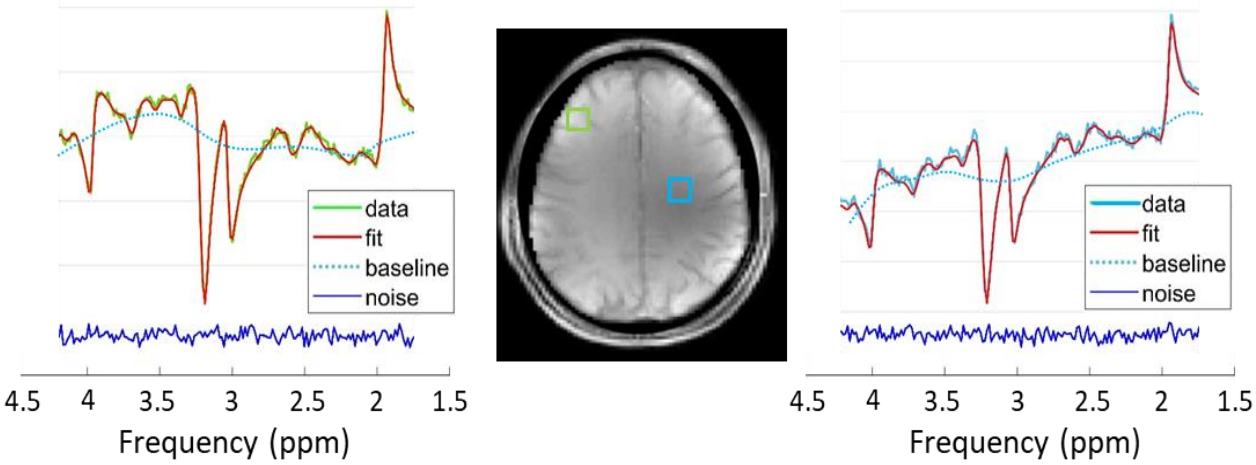

Figure 4.5: Representative example of ^{1}H FID RSI brain metabolite spectra and corresponding LCModel fitting from two voxel locations in the GM (green, on the left) and the WM (blue, on the right) shown in the frequency range of 1.8-4.2 ppm.

Metabolic maps of six major metabolites NAA, Cr, tCho (total choline), mI, NAAG, and Glu are shown in Figure 4.6. The metabolite maps demonstrate spatial pattern for each metabolite distribution. Although relatively evenly distributed, slightly higher NAA concentration was found in the GM compared to the WM. An increased amount of Cr was found in the GM compared to the WM. mI concentration was also higher in the GM compared to the WM. A very high amount of Glu was found in the GM compared to the WM. Higher concentration of NAAG was found in the WM compared to the GM. tCho was also higher in the WM compared to the GM. The average CRLB ranged from 5.3-12.6 % for these brain metabolites in the GM and the WM. GM to WM concentration ratios and CRLB for each brain metabolite in the GM and the WM are presented in Table 4.1.

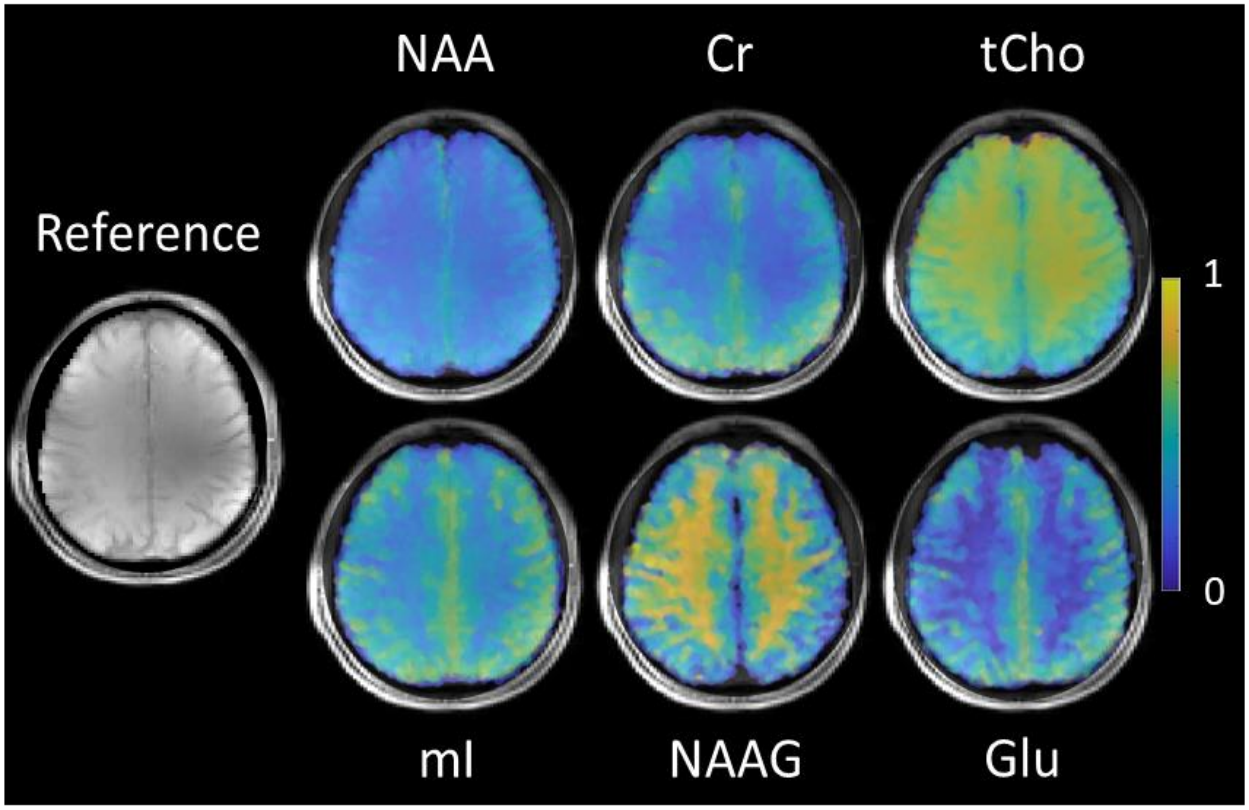

Figure 4.6: High-resolution ^{1}H FID RSI metabolic maps of six major brain metabolites with the reference image of the slice from a representative subject. N-acetyl-aspartate (NAA), creatine (Cr), total choline (tCho), myo-inositol (mI), N-acetyl-aspartyl glutamate (NAAG), and glutamate (Glu) maps are shown with CRLB<20%.

Table 4.1: GM to WM concentration ratios (Conc (GM/WM)) and CRLB (in the GM and the WM) for brain metabolites from all subject scans. All results are presented as mean±SD.

	Brain metabolites					
	NAA	Cr	tCho	mI	NAAG	Glu
Conc(GM/WM)	1.1±0.04	1.26±0.15	0.81±0.08	1.28±0.09	0.59±0.11	1.43±0.06

CRLB(GM)(%)	6.2±0.1	5.3±0.3	7.1±0.5	9.4±0.8	12.6±1.2	8.7±0.7
CRLB(WM)(%)	8.1±0.6	7.2±0.5	6.8±0.8	11.6±1.1	10.4±0.9	9.3±0.6

Metabolite concentration ratio normalized to tCr (Cr+PCr) for each metabolite in the GM and the WM is presented in Table 4.2. NAA concentration was found higher than tCr both in the GM and the WM. tCho was lower than tCr both in the GM and the WM. mI concentration was slightly lower than tCr both in the GM and the WM. NAAG was lower both in the GM and the WM compared to tCr. While Glu was higher in the GM compared to tCr, it was approximately the same as tCr in the WM.

Table 4.2: Metabolic concentration ratio to tCr (total Creatine: Cr+PCr) in the GM and the WM.

	Cr+PCr normalized brain metabolite concentration ratio				
	NAA/tCr	tCho/tCr	mI/tCr	NAAG/tCr	Glu/tCr
GM	1.64±0.06	0.21±0.02	0.93±0.07	0.16±0.01	1.17±0.09
WM	1.86±0.13	0.32±0.04	0.91±0.06	0.36±0.02	0.98±0.08

4.4 Discussion

In this study, we demonstrated the feasibility of non-lipid suppressed high-resolution single-slice ^{1}H FID rosette spectroscopic imaging at 7T, which is fast and within clinically relevant time. The

high spectral resolution and SNR offered by UHF strength of 7T and the advantages of FID sequences, such as low signal loss and negligible chemical shift displacement, enabled reliable quantification of spectra from a large number of voxels. ^{1}H FID RSI provided similar spectral information as the conventional PE and other MRSI methods in the literature. The in-plane resolution of 2×2 mm^2 of the RSI provided similar spatial patterns for major metabolic distributions in the brain as demonstrated by other MRSI methods.

The rosette trajectory used in this study (with $\omega_1 = \omega_2$) has been successfully used in pervious human brain MRSI studies [48, 193]. For this rosette design, the k-space trajectory is circular, which is somewhat similar to the concentric circle trajectory [211]. The main difference between the techniques is, unlike the concentric circle trajectory, which uses circles concentric with the center of the k-space, the circular rosette trajectory starts from and ends at the center of the k-space. This inherently makes the k-space sampling more densely weighted near the center of the k-space, which can make the RSI technique more robust to motion. Additionally, the most peripheral concentric circle (with maximum radius) trajectory needs twice the maximum gradient and maximum slew rate compared to the rosette trajectory [48]. Compared to other SSE techniques such as EPSI and SSI, RSI also uses lower maximum gradient and slew rate for similar acquisition parameters, which can be easily traded for higher spectral bandwidth [48, 193]. Therefore, especially at UHF, RSI is preferred over EPSI and SSI [193, 195].

The acquisition and reconstruction protocols used in this study for rosette trajectory did a good job in terms of image quality and minimizing the variation in the image intensity due to the magnetic field inhomogeneity compared to the Cartesian images (Figure 4.4). Variation in image intensity due to magnetic field inhomogeneity can affect the metabolite quantification and the metabolic

maps. As seen from Figure 4.4, the effect of magnetic field inhomogeneity is expected to be less severe in the metabolite quantification in this study.

Metabolite T_2 relaxation times decrease as B_0 increases [212]. Therefore, shorter TE is required for UHF MRSI to compensate for faster T_2 decay. Our approach for ultra-short TE was similar to previous pulse-acquire FID schemes [177, 179, 182, 200, 205, 213]. This ultra-short TE and TR result in a MRSI scan within the clinically feasible time. The optimized WET water suppression scheme was able to achieve ~99 % suppression of the water peak. Previous MRSI studies at UHF also used similar water suppression using three or four pulse WET scheme [182, 200, 205]. Due to the first-order phase error introduced by the acquisition delay (i.e., TE=1.5 ms), a delay was introduced in the simulation of the basis set for the LCModel. This approach can reliably quantify the metabolites even if the phase of the spectrum is negative [176, 177]. Our metabolite spectra and LCModel fitting was similar to the spectra without the first-order phase correction [177, 205]. L_2-regularization was found to provide good suppression of the lipid signal, which is consistent with the previous MRSI studies at UHF [182, 200, 205].

In this study, NAA concentration was found to be mostly homogeneous in the brain with slightly higher concentration in the GM. Cr and mI concentrations were higher in the GM compared to the WM. A very high amount of Glu was found in the GM compared to the WM. On the other hand, tCho and NAAG concentrations were found to be lower in the GM compared to the WM. Spatial distributions of metabolic concentrations for these brain metabolites found in this study are consistent with previous MRSI studies [176, 179, 190, 200, 205, 213]. GM to WM ratios of these metabolic concentrations are also in agreement with the previous MRSI reports [190, 200]. Compared to tCr, higher NAA concentration was found both in the GM and the WM. On the other hand, tCho and NAAG were lower than tCr both in the GM and the WM. mI concentration was slightly lower than

tCr both in the GM and the WM. While Glu was higher in the GM compared to tCr, it was approximately the same as tCr in the WM. These tCr normalized metabolite ratios are also consistent with previous studies [177, 190].

There are several limitations to our study. Even though the vendor-provided second-order shimming routine was found to provide good performance and has been used in previous MRSI studies[177, 182, 200], the water suppression performance can still be affected by the B_0 field inhomogeneity. This problem can be mitigated by using higher order and higher degree shimming or shimming the lipid region as a region of less interest (ROLI) [180, 214, 215]. Better B_0 shimming can also result in better separation of the metabolites [215]. B_1 inhomogeneity can also affect the metabolite quantification. B_1 insensitive adiabatic refocusing pulses have been proposed to reduce the signal loss [178, 216, 217]. Further correction to B_1 inhomogeneity can be achieved by using parallel transmit pulses designed for B_1 inhomogeneity compensation or more complicated approaches, such as performing Bloch simulations to determine the excitation profile [180, 218]. L_2-regularization has been shown to effectively remove the lipid signal without reducing the SNR of the metabolites [209], which has been used for MRSI studies at UHF [182, 200, 205]. However, because of the alteration of the lipid range of the spectra, it can no longer be used to evaluate the macromolecules or lipid content alterations of the spectra. Additionally, the exact quantification of peaks close to this range, such as GABA, might be affected. As the TE for this study was very short (1.5 ms), T_1 weighting is expected due to the short TR. This can be solved using tissue segmentation followed by a voxel-wise relaxation correction that would account for the differences in the relaxation times across different tissues [218, 219]. In addition, due to the short TE and TR, including macromolecules in the basis set simulation can increase the reliability of the metabolite quantification [220, 221]. Fully sampled k-space was acquired in this study for RSI. Under-sampled k-space (with reduced number

of rosette shots) can also be implemented using compressed sensing to further reduce the imaging time. An alternative technique, such as parallel imaging, needs to be incorporated with RSI to increase the SNR of the metabolite signals compared to the lipid signals, or an additional lipid suppression pulse is needed to suppress the lipid signal [179, 190].

In summary, we have demonstrated the feasibility of non-lipid suppressed high-resolution ^{1}H FID rosette spectroscopic imaging of the human brain at 7T. This technique can be implemented within clinically feasible scan time and can provide information about spatial distribution of major metabolites in the human brain. This can be very useful in clinical application to diagnose central nervous system diseases.

Chapter 5

Feasibility of Spinal Cord Imaging at 7T using Rosette Trajectory with Magnetization Transfer Preparation and Compressed Sensing

5.1 Background

MRI is a valuable diagnostic tool to investigate spinal cord (SC) pathology, such as cervical spondylotic myelopathy, multiple sclerosis, amyotrophic lateral sclerosis, and neurodegenerative diseases [38-42]. However, the ability to detect subtle pathological features in SC MRI is limited by spatial resolution, contrast-to-noise ratio (CNR), and physiological motion [43-45].

High spatial resolution is essential for SC MRI to minimize the partial volume effect between the gray matter (GM) and the white matter (WM) due to the small diameter of the cord (~1 cm)[44]. Ultra-high field (UHF) MRI can potentially improve SC diagnosis using increased signal-to-noise ratio (SNR) and improved susceptibility contrast to support high spatial resolution. Previous studies have demonstrated the advantage of UHF MRI of the SC at 7T [222-225]. Routine Cartesian MRI of the SC is susceptible to image artifacts caused by physiological motion. The SC moves within the spinal canal together with the cerebrospinal fluid (CSF)[226]. Additionally, the entire spine is likely to move slightly with respiration, swallowing, and bulk motion. These motions can cause distortion, loss of contrast, decreased spatial resolution, and decreased SNR of the MR signal [43, 44]. Non-Cartesian acquisition technique, such as rosette, is inherently insensitive to bulk motion. Therefore, such non-Cartesian acquisition technique can greatly help reduce the motion-related

artifacts in SC MRI. The advantage of non-Cartesian acquisition has been demonstrated in diffusion, cardiac imaging, fMRI, and real-time imaging[227-230]. In spite of the potential advantage of the non-Cartesian trajectory, it has not been explored thoroughly for SC imaging. A recent study demonstrated the advantage of spiral imaging of the SC at 1.5T [231]. These advantages can be further enhanced at UHF MRI. The properties that make rosette imaging more compelling than spiral imaging are flexible trajectory design, smoothly varying gradient waveforms and self-correction of inhomogeneity [46-48]. Therefore, rosette imaging of the SC at UHF can potentially be of clinical interest.

Conventional SC MRI focuses on T_1 and T_2 weighted imaging as they can reflect changes in the tissue, such as lesions, atrophy etc. However, within the tissue, there are semi-solid protons associated with large macromolecules with very short T_2 relaxation times that are extremely difficult to be imaged with T_1 and T_2 weighted MRI. Magnetization transfer (MT) is an effective approach to evaluate these protons, as the MT effect is directly proportional to the water in tissue water and water associated with the macromolecules. The MT effect has been shown to be sensitive to the myelin concentration [232, 233]. Therefore, the magnetization transfer ratio (MTR) in the spinal cord can provide valuable information in assessing spinal cord pathology. In addition to the MTR, cerebrospinal fluid (CSF) normalized MT weighted signal (MTCSF) has also been demonstrated to be clinically relevant in patients with the proven biochemical defect of adrenomyeloneuropathy (AMN) [234]. MT-weighted rosette imaging of the SC can further improve the assessment of the SC with reduced motion artifacts and can be very useful in clinical applications.

Imaging speed can be very important in many MRI applications. The implicit sparsity in MR images can be used to undersample the k-space, which can significantly reduce the imaging time. Compressed sensing (CS) is a valuable tool to exploit the sparsity in MR images [185, 186, 235]. CS has

been evaluated in a number of MR applications, such as dynamic contrast enhanced MRI (DCE-MRI), MR spectroscopy, pediatric MRI, phase-contrast MRI for cardiac imaging, and multispectral imaging of the spine [189, 190, 236-239]. SC MRI can also benefit from CS, especially for long multi-slice/3D high resolution imaging sessions, by reducing the data size required to sample and decreasing the imaging time to a convenient limit for the patients. Reduced imaging time also makes it easier for the subjects to stay still inside the scanner, decreasing the possibility of motion-related artifacts in the image. Non-Cartesian acquisition techniques, such as rosette, can take the advantage of CS to improve SC imaging.

The goal of this study was threefold: (i) implement a technique for high-resolution SC imaging using rosette trajectory at 7T, (ii) demonstrate MT weighted high-resolution rosette imaging of the SC, and (iii) evaluate the application of CS for high-resolution rosette imaging of the SC. These techniques can be very useful in assessing SC pathology.

5.2 Materials and Methods

5.2.1 Rosette trajectory design

The rosette trajectories oscillate in the radial direction about the origin of k-space with angular frequency $\omega_1 = 2\pi f_1$, simultaneously rotating in the k_x-k_y plane with angular oscillation frequency $\omega_2 = 2\pi f_2$. The k-space trajectory is given by [46-48]

$$k(t) = k_{max}\sin(\omega_1 t)e^{i\omega_2 t} \quad 5.1$$

where $k_{max}=N_x/(2.FOV)$ is the highest spatial frequency sampled, N_x is the matrix size and FOV is the field of view. The value of f_1 and f_2 can be chosen based on the intended shape of the k-space trajectory. We chose $f_1=f_2$ for constant maximum gradient strength throughout the readout, which results in a circular trajectory for a single shot [48]. The corresponding gradient was calculated using $G(t) = \frac{2\pi}{\gamma}\frac{dk(t)}{dt}$, where γ is the ^{1}H gyromagnetic ratio [46-48]. The total number of shots to fill up the k-space based on the intended image resolution was [48]

$$N_{sh} = \frac{\pi N_x}{2} \qquad 5.2$$

Rosette images were acquired with and without the application of the MT pulses for multiple slices. The schematic of the pulse sequence is shown in Figure 5.1.

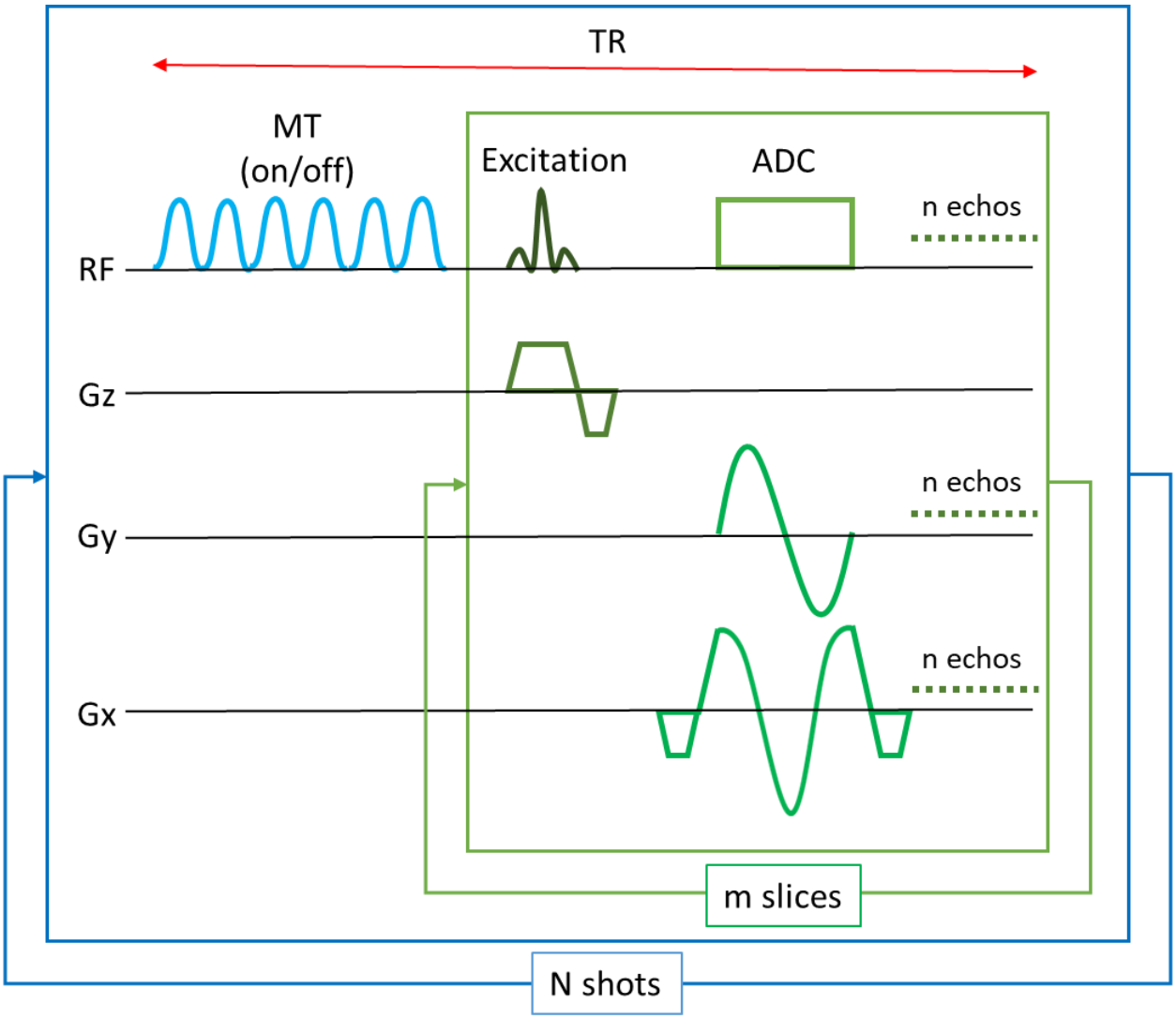

Figure 5.1: Schematic of the pulse sequence used for rosette imaging. The outer (blue) box represents the module for one rosette shot and the inner (green) box represents the module for a single slice. The sequence is composed of 6 MT pulses that can be turned on/off for acquiring rosette data with/without the saturation of the macromolecules, followed by an excitation RF pulse for each slice to acquire *n* echoes. *Gy* and *Gx* represent the rosette gradients along the phase encode and the readout axes, and *Gz* is the slice selective gradient. *Gy* starts from 0 and returns to 0 for each acquisition, while *Gx* starts from the maximum value and ends at the same maximum value.

Therefore, ramp up and ramp down were used at the beginning and end of *Gx*. The inner module (green box) was repeated to acquire *m* slices. After acquiring rosette data for all the echoes from all the slices for each shot, the outer module (blue box) was repeated to acquire *N* rosette shots.

5.2.2 SNR and CNR

SNR for the GM, the WM and the CSF can be calculated using [240]

$$SNR = \frac{S_{tissue,mean}}{S_{BG,SD}} \tag{5.3}$$

where $S_{tissue,mean}$ is the mean signal from tissue region of interest (ROI) and $S_{BG,SD}$ is the standard deviation of the noise (from background/air ROI).

CNR between different types of tissue can be calculated using [240]

$$CNR = \frac{S_{tissue1,mean} - S_{tissue2,mean}}{S_{BG,SD}} \tag{5.4}$$

where $S_{tissue1,mean}$ and $S_{tissue2,mean}$ are mean signals from the two tissues of interest.

5.2.3 MTR and MTCSF

MTR was calculated from the images acquired with and without the MT pulses using [241]

$$MTR = 1 - \frac{S_{MT}}{S_o} \tag{5.5}$$

where S_o and S_{MT} are signals acquired without and with the MT pulses respectively.

MTCSF was calculated from the images acquired with MT pulses only, from the ratio of signals from the tissue (gray matter (GM)/white matter (WM)) and the CSF using [234]

$$MTCSF = \frac{S_{MT}}{S_{CSF}} \quad 5.6$$

where S_{CSF} is the mean signal from CSF ROI.

5.2.4 Compressed sensing

The basis of CS is that the reconstructed image must be consistent with the Fourier transform of the acquired k-space data, having few large-valued coefficients when sparsely transformed. Essentially, this is an optimization problem (l_1 regularization) that minimizes this form [186]

$$\min_x(\| Y - Fx \|_2^2 + \lambda \| \psi x \|_1) \quad 5.7$$

where Y is the measured k-space data, x is the reconstructed image, F is the Fourier transform, ψ is a transform such that ψx becomes sparse, and λ is a regularization parameter weighting the relative importance of the two terms. The symbols $\| \cdots \|_1$ and $\| \cdots \|_2^2$ represent sums of absolute values and their squares, respectively. Eq 5.7 can be solved using a nonlinear conjugate gradient descent algorithm as demonstrated in [186]. Data were reconstructed from a reduced number of rosette shots using CS with total variation (TV) sparsifying transform and parameters similar to the GRASP technique [242] and compared with the images reconstructed with the required number of shots using Eq 5.2.

5.2.5 Recruitment

The study was approved by the Auburn University Institutional Review Board (IRB). All experiments were performed in accordance with the IRB guidelines and regulations. All the subjects provided informed consent prior to participation in the study. Five healthy subjects (age=41±13 years, weight=73±11 kg) participated in the study. All the participants were non-smokers and had no history of neuromuscular or metabolic disease.

5.2.6 Imaging pulse sequence

All the experiments were performed on a Siemens 7T Magnetom (Erlangen, Germany) using 8 channel spine coil. The peak gradient and slew rate of the scanner were 70 mT/m and 200 mT/m/ms, respectively.

The pulse sequence used for rosette imaging is shown in Figure 5.1. Six MT pulses, each with duration of 16.64 ms (bandwidth=80 Hz), were tuned on/off before the excitation pulse to acquire images with/without MT weighting. The MT pulse offset frequency was 500 Hz with flip angle of 500^{o} to saturate the macromolecules. The MT pulse train (6 MT pulses) was applied once for each TR, where the TR included the acquisition time for all the echoes in all the slices for each rosette shot. Then, it was repeated for all the rosette shots. Following the MT pulse train, a sinc excitation pulse with pulse duration of 1 ms was used to excite each slice.

The rosette acquisition parameters were: FOV=192 mm, matrix=384, in-plane resolution=0.5×0.5 mm^2, slice thickness=4mm, number of slices=7, $f_1=f_2=1500$ Hz, flip angle=39^0, sampling time=1 μs, and TR=500 ms. The total number of rosette shots acquired was 603 (using Eq 5.2). Combining multi-echo images can improve the contrast of the image[222]. For rosette imaging, multi-echo images were acquired at TE=3, 7.8 and 15 ms. To compare the rosette images, single echo FLASH images were also acquired with the same FOV, matrix size, in-plane resolution, slice thickness,

and number of slices. Other parameters for the FLASH acquisition were: TE=3 ms, TR=40 ms, and flip angle=10^0.

5.2.7 Data analysis

Data analysis was performed offline using MATLAB (MathWorks, Natick, MA). Discrepancy in the rosette trajectory due to the magnetic field inhomogeneity was corrected using an estimated linear field map from the 1st two rosette echo images [204]. Then the rosette images were reconstructed for each slice using 2D gridding on a two-fold oversampled grid with a Kaiser-Bessel kernel window W=4 [207] and density compensation was applied [208]. Images were reconstructed from 603 shots and a reduced number of shots using CS [186].

Reconstructed images were segmented using the spinal cord processing toolbox (SCT) [243], and SNR for the GM, the WM, and the CSF were calculated using Eq 5.3. The CNR for GM:WM and CSF:WM were calculated using Eq 5.4. MTR was calculated using Eq 5.5 from the images acquired with and without the MT pulses. MTCSF was calculated using Eq 5.6, where the mean signal from CSF ROI was used as $S_{CSF.}$ All results are reported as mean ± standard deviation.

5.3 Results

The maximum gradient amplitude was 35.23mT/m, and the maximum slew rate was 105.7 mT/m/ms for the chosen rosette design (Figure 5.2). Representative single echo rosette images (603 shots) from 7 slices on the spine at TE=3 ms are shown in Figure 5.3. Single echo rosette images (603 shots) show reduced blurring and sharper contrast among the GM, the WM and the CSF compared to single-echo FLASH images (TE=3 ms for both) (Figure 5.4). Slice 4-7 (SL 4-

SL 7 in Figure 5.3) show severe motion artifacts in the FLASH images, while the rosette images do an excellent job in reducing the motion artifacts (Figure 5.4). Rosette images also demonstrated overall higher SNR and CNR compared to the FLASH images. Comparisons of the SNR and CNR between rosette and FLASH images are provided in Table 5.1.

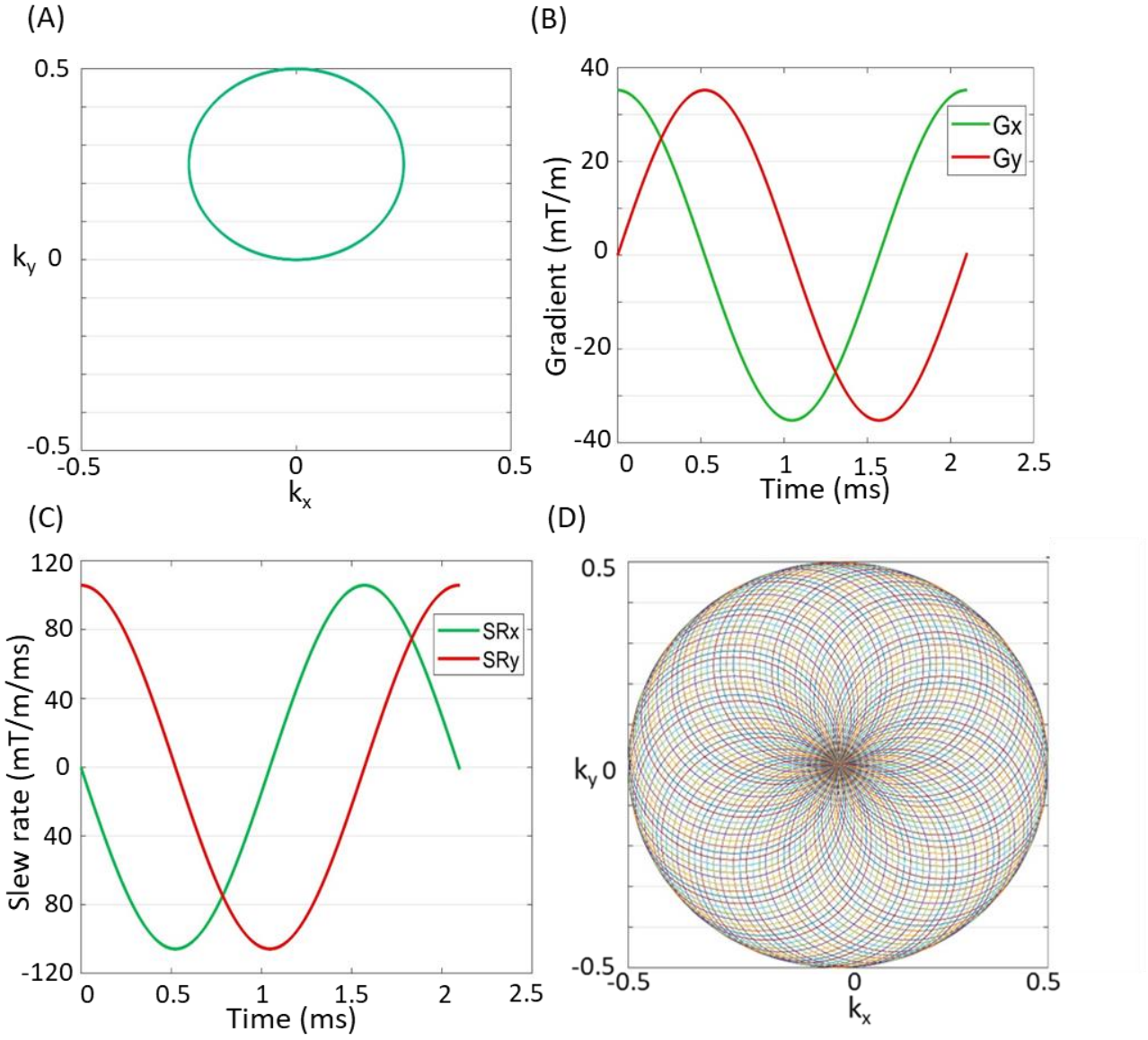

Figure 5.2: Rosette trajectory for a single shot (A), corresponding gradients (B), and slew rates (C) along *X* and *Y* axes for f_1=f_2=1500 Hz, *FOV*=192 mm, and matrix size=384. A total of 603 shots were needed to fill up the k-space with the intended image resolution (D).

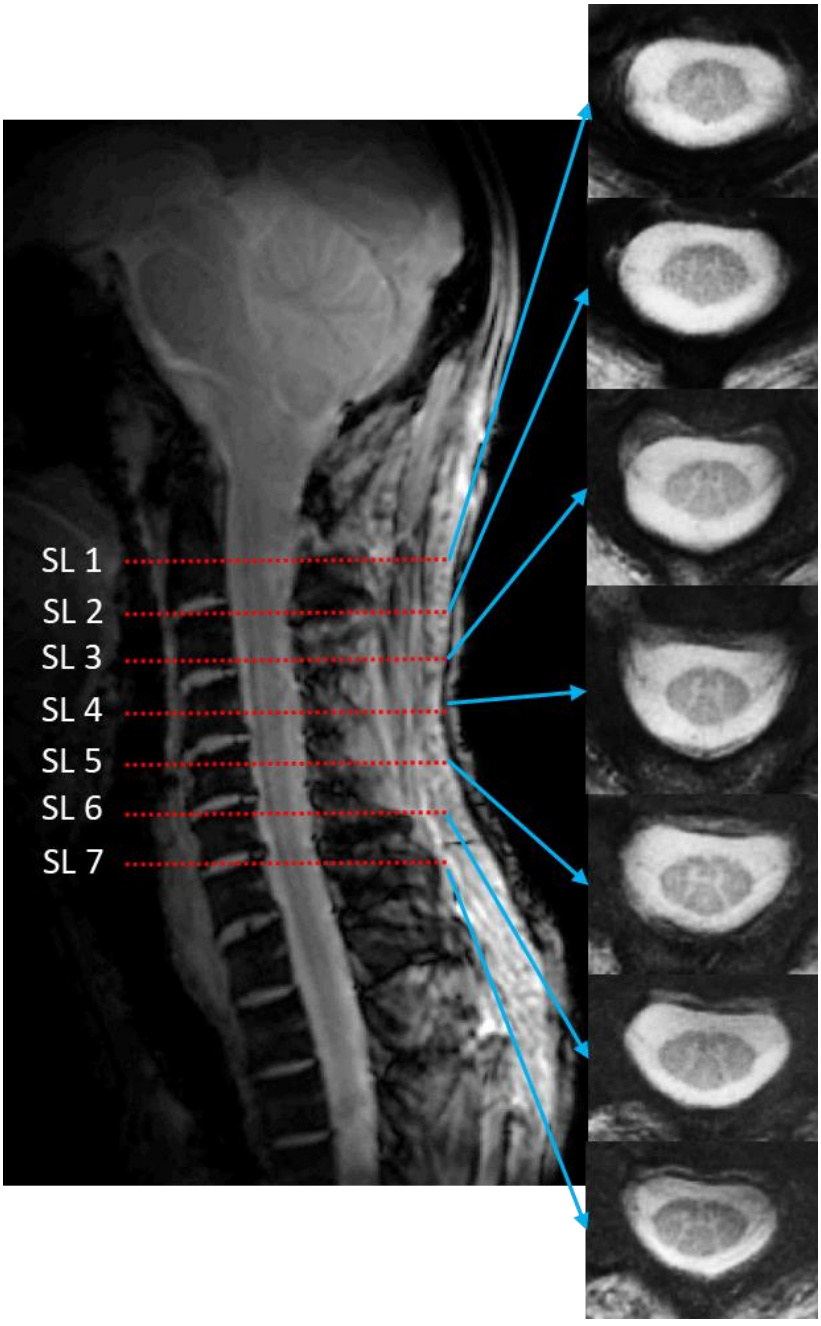

Figure 5.3: Slice locations on the SC (SL 1-SL 7) and corresponding rosette images from a representative subject.

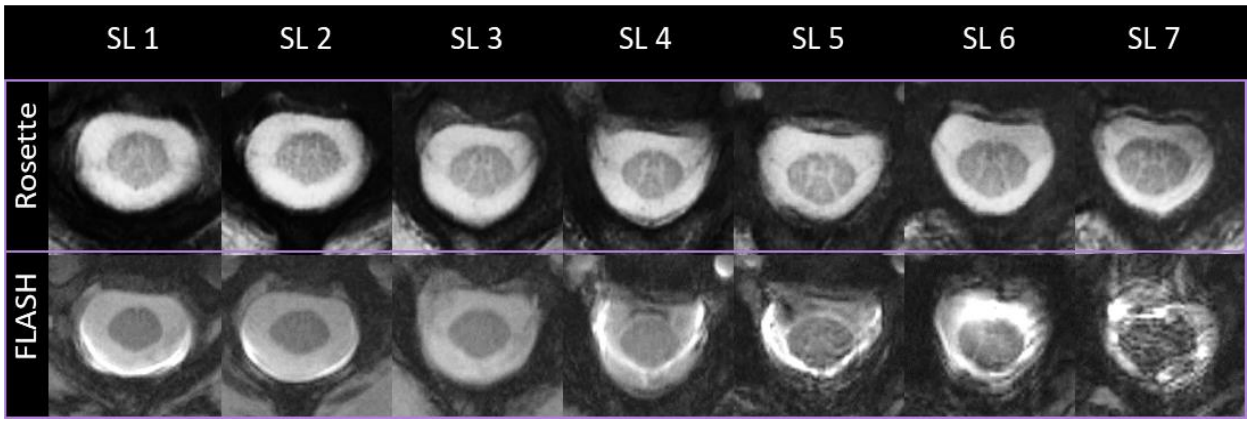

Figure 5.4: Comparison of rosette (top row) and Cartesian (FLASH, bottom row) images from seven slice locations (SL 1-SL 7) from a representative subject. Rosette images show higher contrast between different tissue types compared to the Cartesian images. Severe motion artifacts are visible in the Cartesian images (SL 4-SL 7), which are significantly improved in the rosette images.

Table 5.1: Comparison of the SNR (in the WM, the GM, and the CSF) and the CNR (GM:WM and CSF:WM) among single-echo Cartesian images, average of multi-echo fully sampled (603 shots) rosette images, single-echo fully sampled rosette images, and single-echo undersampled rosette images reconstructed using CS (201 shots-CS and 100 shots-CS) from all the subjects. TE=3 ms for all single-echo data, and TE=3, 7.8 and 15 ms for all multi-echo data.

	SNR			**CNR**	
	WM	GM	CSF	GM:WM	CSF:WM

Single echo Cartesian (FLASH)	25.3±3.7	26.7±4.1	57.4±6.3	1.3±0.3	31.8±5.7
603 shots multi-echo average rosette	51.8±7.3	57.3±6.2	121.6±8.4	7.2±1.7	67.1±6.3
603 shots single echo rosette	45.7±6.1	49.4±3.7	109.3±9.8	4.8±1.1	59.6±7.2
201 shots-CS single echo rosette	42.9±7.3	46.6±6.2	105.1±8.7	4.1±1.1	56.8±8.7
100 shots-CS single echo rosette	38.1±4.6	40.9±7.3	93.6±9.3	2.9±0.9	47.6±9.8

Averaging multiple echo time rosette images (TE=3, 7.8 and 15 ms) significantly improves the contrast among the GM, the WM, and the CSF in the spinal cord (Figure 5.5) compared to the single-echo images (TE=3 ms). SNR and CNR from multi-echo averaged images were also higher than the single-echo rosette images (Table 5.1).

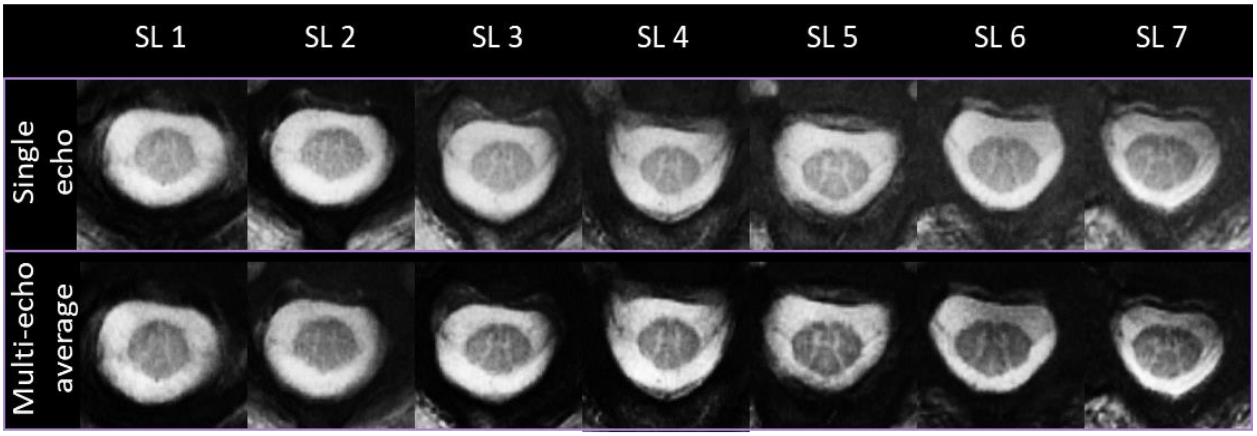

Figure 5.5: Comparison of single-echo rosette images (TE=3 ms, top row) and the average of multi-echo rosette images (TE=3, 7.8, and 15 ms, bottom row) from seven slice locations (SL 1-SL 7) from a representative subject. Multi-echo averaged rosette images show improved contrast between different types of tissues compared to the single-echo images.

MTR and MTCSF maps from a representative subject are shown in Figure 5.6. MTR was lower in the GM (0.12 ± 0.017) compared to the WM (0.18 ± 0.011), averaged across all the subjects. MTR in the CSF was approximately 0, as the CSF has little to no MT effect [43]. Due to the definition of MTCSF, the tissue contrast in MTCSF map is inverted from that of the MTR. MTCSF was higher in the GM (0.74±0.013) compared to the WM (0.58±0.009), averaged across all the subjects. Obviously, MTCSF in the CSF was approximately 1 as MTCSF is calculated by normalizing to the average CSF signal.

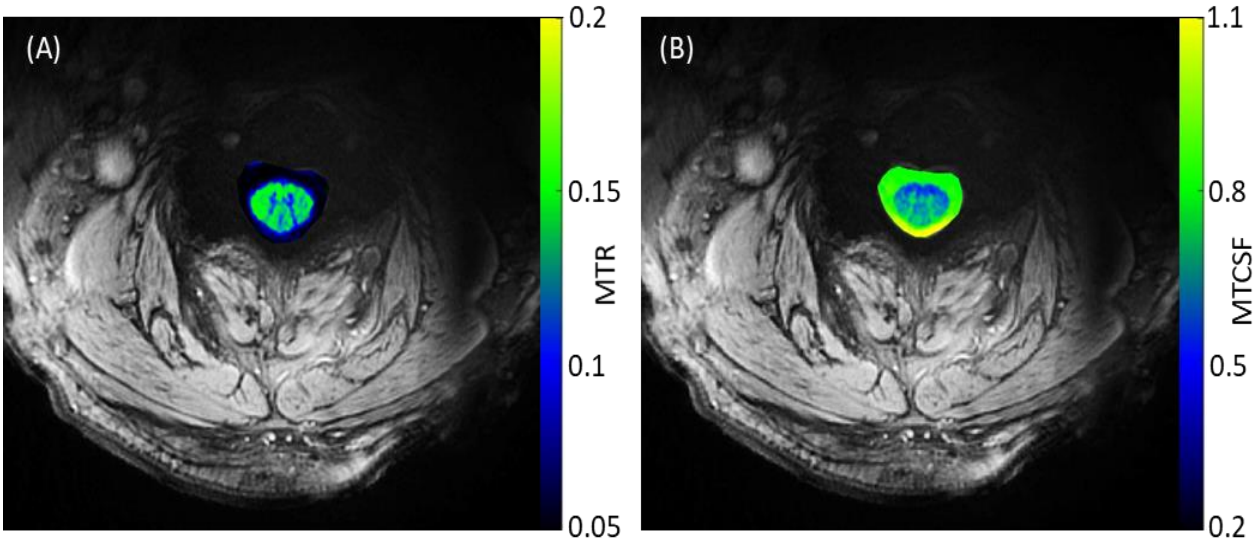

Figure 5.6: MTR and MTCSF maps ((A) and (B), respectively) from a representative subject. MTR and MTCSF show inverted contrast between different types of tissues.

CS reconstruction of undersampled data (100 and 201 shots) shows image quality comparable to the images reconstructed from fully sampled data (603 shots) (Figure 5.7). For 201 shots, images reconstructed with CS are almost identical to the images reconstructed from 603 shots. SNR and CNR from 201 shots-CS images were also very close to the 603 shots images (Table 5.1). While the images reconstructed from 100 shots with CS lose some minor details, it is still very comparable to the images reconstructed from 603 shots. SNR and CNR from 100 shots-CS images were slightly lower than the 603 shots images but still better than the Cartesian images (Table 5.1). Undersampled rosette acquisition with compressed sensing reconstruction allows us to reduce the acquisition time by up to 6x and potentially help with patient comfort and reduced motion blurring.

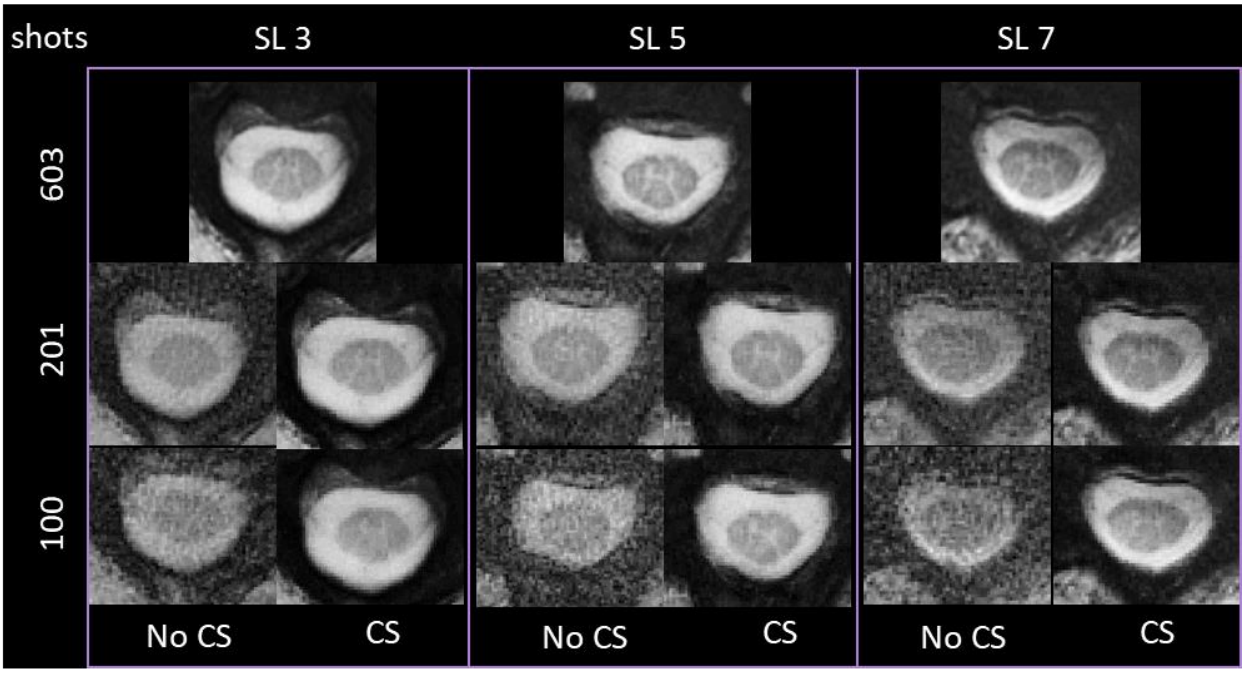

Figure 5.7: Evaluation of CS for rosette imaging of the SC. Rosette images reconstructed from fully sampled k-space (603 shots) from three representative slice locations (SL 3, SL 5, and SL 7). Rosette images reconstructed using CS from undersampled k-space (201 and 100 shots) show significant improvement over the same images reconstructed without CS and are very similar to the images reconstructed from fully sampled k-space.

5.4 Discussion

This study is the first report to demonstrate high-resolution rosette MRI of the SC at 7T. We also demonstrated high-resolution MT contrast and the application of CS for rosette imaging of the SC. The advantages of the rosette acquisition compared to the routine Cartesian acquisition, including low susceptibility to bulk motion and improved contrast, can greatly benefit the investigation of SC pathology in the clinical setup. MT-weighted rosette imaging can provide further valuable

information, such as MTR and MTCSF, which have added value to assess WM pathology. CS can be very useful for rapid SC rosette imaging, which can make the imaging time convenient for the patients and also help reduce the motion artifacts.

In spite of the obvious potential advantages of UHF MRI of the SC, there are still considerable challenges associated with 7T SC imaging that need to be overcome. Previous studies have demonstrated the advantage of UHF MRI of the SC at 7T, but they mostly concentrated on the coil design [222, 223, 225, 244, 245]. SNR, CNR, and motion artifacts are some of biggest issues that need to be addressed for high resolution SC imaging. In our study, rosette images of the SC showed significant improvement over Cartesian (FLASH) images. Enhanced contrast between different types of tissues were visible in rosette images compared to the Cartesian images (Figure 5.4). Averaging multiple echo rosette images further improves the contrast (Figure 5.5). Overall, SNR and CNR for different types of tissues were also higher in the rosette images (Table 5.1). Rosette images did an excellent job to reduce the physiological motion related artifacts in the images compared to the Cartesian images, especially at the locations of thoracic SC and towards the lower end of cervical SC that are more prone to respiratory motion (Figure 5.4). The rosette acquisition technique has already been used in a number of MR applications such as MR spectroscopic imaging (MRSI), fMRI, etc. [47, 48, 227]. These advantages of rosette imaging over Cartesian imaging can make it a potential candidate for routine SC imaging.

The effect of MT has been evaluated in diseases such as multiple sclerosis (MS), defect of adrenomyeloneuropathy (AMN), etc. [125, 173, 232, 234]. Therefore, MTR and MTCSF can be valuable non-invasive biomarkers in WM diseases. MTR and MTCSF depend on the macromolecular concentration. MTR is usually higher in the WM due to the high concentration of macromolecules, such as proteins and lipids, present in the myelin sheath. On the other hand, as per the definition

of MTCSF, the tissue contrast in MTCSF is opposite to that of MTR (i.e., higher in the GM and lower in the WM). WM pathology, such as demyelination causes the macromolecular concentration in the WM to drop and consequently affects the MTR and MTCSF. Although MTR and MTCSF are very useful in investigating such diseases, there are no standard values for MTR and MTCSF since they depend on the amount of the macromolecular saturation. However, using the same MT protocol for control subjects and patient populations would be an effective way to assess the difference. The average MTR in this study was relatively low (0.12 ± 0.017 and 0.18 ± 0.011 in the GM and the WM, respectively). This is because relatively low MT power was used in this study to keep the specific absorption rate (SAR) low. Nevertheless, this was sufficient to generate good MT contrast between the tissues (Figure 5.6). The corresponding MTCSF map also shows good contrast between the tissues (Figure 5.6). The direct spillover effect of the MT pulses was measured to be <2%. Although an offset frequency of 500 Hz for the MT pulses shows good MT contrast, higher offset frequencies can potentially improve the MT contrast further [234]. MT contrast with respect to different offset frequencies was not tested in this study.

CS reconstruction of the SC rosette images demonstrates that the k-space can be undersampled without severely compromising the image quality. The optimum number of shots for the intended resolution in this study was 603 (Eq 5.2). Images reconstructed from 201 shots with CS are very similar to the images reconstructed from 603 shots (Figure 5.7). The SNR and the CNR for 603 shots reconstruction and 201 shots-CS reconstruction are also very similar (Table 5.1). This can accelerate the imaging by a factor of 3. Rosette images reconstructed from 100 shots using CS have a minor downgrade in the image quality compared to the images reconstructed from 603 shots (Figure 5.7) but still have better image quality than the Cartesian images. The SNR and CNR for 100 shots-CS reconstructed rosette images were slightly lower than the 603 shots reconstructed

images but still higher than the Cartesian images (Table 5.1). This can accelerate the rosette imaging by a factor of 6. The application of CS has been evaluated in a number of MRI studies, such as chemical shift imaging (CSI), phase-contrast MRI for cardiac imaging, dynamic contrast enhanced MRI (DCE-MRI), pediatric MRI, and multispectral imaging of the spine [189, 190, 236-239]. SC rosette imaging can also benefit from the application of CS in disease diagnosis.

The imaging time for rosette acquisition depends on the number of shots and oscillation frequencies (f_1 and f_2). Choice of the oscillation frequencies are limited by the hardware of the scanner (i.e., maximum gradient and slew rate of the system). We chose $f_1=f_2$=1500 Hz to keep the maximum gradient and slew rate relatively low. The chosen design for the rosette trajectory in this study resulted in a maximum gradient of 35.23mT/m and maximum slew rate of 105.7 mT/m/ms, which are roughly half of the maximum capacity of the system (70 mT/m and 200 mT/m/ms, respectively). CS can reduce the number of shots required for imaging, as demonstrated in this study, which can reduce the imaging time significantly. The imaging can be made even faster by increasing the oscillation frequencies, but it would push the maximum gradient and slew rate limits of the system. We used an in-plane resolution of 0.5×0.5 mm^2 in this study. Even higher resolution rosette imaging is possible (i.e. 0.3×0.3 mm^2 in-plane resolution), but it was not the goal of this study. Our goal was to demonstrate the feasibility and advantages of rosette imaging of the SC at UHF MRI. Higher resolution rosette imaging is a goal of our future study.

In summary, we demonstrated the feasibility of a technique for high-resolution rosette imaging of the SC at 7T, with the addition of MT-weighted rosette imaging and the application of CS. This technique can be very useful to reduce motion artifacts and improve the SNR and the CNR compared to routine Cartesian imaging. Additionally, MT-weighted imaging and CS can help

diagnose WM pathology and reduce the imaging time, which can be beneficial for clinical applications.

Chapter 6

Conclusion

Quantitative MRI of hemodynamics, endothelial function, and metabolites can provide valuable information about blood and nutrition supply, oxygenation, vascular integrity, and metabolite concentrations in vivo. This information can be very crucial in the early diagnosis of CNS and musculoskeletal pathology. This work presents a comprehensive study for improved imaging techniques to measure hemodynamic, endothelial, and metabolite information in the CNS and skeletal muscle. In this work we have demonstrated an improved motion-robust non-Cartesian imaging technique for high-resolution SC imaging, a fast and motion-robust technique for high-resolution proton metabolic mapping in the human brain, a novel non-contrast technique for the measurement of blood-brain barrier permeability, and the feasibility and repeatability of a technique for the combined measurement of blood flow, perfusion, oxygen saturation, and oxidative metabolism in the skeletal muscle. Further work is required to improve and calibrate the techniques demonstrated in this work for routine clinical applications. Nevertheless, this work can be very useful for the investigation of different pathologies both in the CNS and skeletal muscle.

References

1. Bennett WM, McDonald WJ, Lawson RK, Porter GA. Posttransplant hypertension: studies of cortical blood flow and the renal pressor system. *Kidney Int.* 1974;6(2):99-108.

2. Pittman RN. *Regulation of Tissue Oxygenation*. San Rafael (CA); 2011.

3. Schmidt-Rohr K. Oxygen Is the High-Energy Molecule Powering Complex Multicellular Life: Fundamental Corrections to Traditional Bioenergetics. *Acs Omega.* 2020;5(5):2221-2233.

4. Marcy VR, Welsh FA. Correlation between Cerebral Blood-Flow and Atp Content Following Tourniquet-Induced Ischemia in Cat Brain. *Journal of Cerebral Blood Flow and Metabolism.* 1984;4(3):362-367.

5. Bonora M, Patergnani S, Rimessi A, De Marchi E, Suski JM, Bononi A, Giorgi C, Marchi S, Missiroli S, Poletti F, Wieckowski MR, Pinton P. ATP synthesis and storage. *Purinergic Signalling.* 2012;8(3):343-357.

6. Bakshi R. Fatigue associated with multiple sclerosis: diagnosis, impact and management. *Multiple Sclerosis Journal.* 2003;9(3):219-227.

7. Barth PG, Scholte HR, Berden JA, Van der Klei-Van Moorsel JM, Luyt-Houwen IE, Van 't Veer-Korthof ET, Van der Harten JJ, Sobotka-Plojhar MA. An X-linked mitochondrial disease affecting cardiac muscle, skeletal muscle and neutrophil leucocytes. *J Neurol Sci.* 1983;62(1-3):327-355.

8. Finsterer J, Mahjoub SZ. Fatigue in Healthy and Diseased Individuals. *American Journal of Hospice & Palliative Medicine.* 2014;31(5):562-575.

9. Kluger BM, Krupp LB, Enoka RM. Fatigue and fatigability in neurologic illnesses Proposal for a unified taxonomy. *Neurology.* 2013;80(4):409-416.

10. Tarnopolsky MA, Raha S. Mitochondrial myopathies: diagnosis, exercise intolerance, and treatment options. *Med Sci Sports Exerc.* 2005;37(12):2086-2093.

11. DeFronzo RA, Tripathy D. Skeletal muscle insulin resistance is the primary defect in type 2 diabetes. *Diabetes Care.* 2009;32 Suppl 2:S157-163.

12. Grevendonk L, Connell NJ, McCrum C, Fealy CE, Bilet L, Bruls YMH, Mevenkamp J, Schrauwen-Hinderling VB, Jorgensen JA, Moonen-Kornips E, Schaart G, Havekes B, de Vogel-van den Bosch J, Bragt MCE, Meijer K, Schrauwen P, Hoeks J. Impact of aging and exercise on skeletal muscle mitochondrial capacity, energy metabolism, and physical function. *Nat Commun.* 2021;12(1):4773.

13. Janssen I, Heymsfield SB, Ross R. Low relative skeletal muscle mass (sarcopenia) in older persons is associated with functional impairment and physical disability. *J Am Geriatr Soc.* 2002;50(5):889-896.

14. Gonzalez-Alonso J, Calbet JA. Reductions in systemic and skeletal muscle blood flow and oxygen delivery limit maximal aerobic capacity in humans. *Circulation.* 2003;107(6):824-830.

15. Ewing JR, Cao Y, Fenstermacher J. Single-coil arterial spin-tagging for estimating cerebral blood flow as viewed from the capillary: relative contributions of intra- and extravascular signal. *Magn Reson Med.* 2001;46(3):465-475.

16. Li KL, Zhu X, Hylton N, Jahng GH, Weiner MW, Schuff N. Four-phase single-capillary stepwise model for kinetics in arterial spin labeling MRI. *Magn Reson Med.* 2005;53(3):511-518.
17. Parkes LM, Tofts PS. Improved accuracy of human cerebral blood perfusion measurements using arterial spin labeling: accounting for capillary water permeability. *Magn Reson Med.* 2002;48(1):27-41.
18. Paulson OB, Hertz MM, Bolwig TG, Lassen NA. Filtration and Diffusion of Water across Blood-Brain-Barrier in Man. *Microvascular Research.* 1977;13(1):113-123.
19. Paulson OB. Blood-brain barrier, brain metabolism and cerebral blood flow. *European Neuropsychopharmacology.* 2002;12(6):495-501.
20. Silva AC, Zhang W, Williams DS, Koretsky AP. Estimation of water extraction fractions in rat brain using magnetic resonance measurement of perfusion with arterial spin labeling. *Magn Reson Med.* 1997;37(1):58-68.
21. Eichling JO, Raichle ME, Grubb RL, Jr., Ter-Pogossian MM. Evidence of the limitations of water as a freely diffusible tracer in brain of the rhesus monkey. *Circ Res.* 1974;35(3):358-364.
22. Go KG, Lammertsma AA, Paans AM, Vaalburg W, Woldring MG. Extraction of water labeled with oxygen 15 during single-capillary transit. Influence of blood pressure, osmolarity, and blood-brain barrier damage. *Arch Neurol.* 1981;38(9):581-584.
23. Ewing JR, Wei L, Knight RA, Pawa S, Nagaraja TN, Brusca T, Divine GW, Fenstermacher JD. Direct comparison of local cerebral blood flow rates measured by MRI arterial spin-tagging and quantitative autoradiography in a rat model of experimental cerebral ischemia. *J Cereb Blood Flow Metab.* 2003;23(2):198-209.
24. Paulson OB. Blood-brain barrier, brain metabolism and cerebral blood flow. *Eur Neuropsychopharmacol.* 2002;12(6):495-501.
25. Abbott NJ, Patabendige AA, Dolman DE, Yusof SR, Begley DJ. Structure and function of the blood-brain barrier. *Neurobiol Dis.* 2010;37(1):13-25.
26. Bell RD, Zlokovic BV. Neurovascular mechanisms and blood-brain barrier disorder in Alzheimer's disease. *Acta Neuropathol.* 2009;118(1):103-113.
27. Desai BS, Monahan AJ, Carvey PM, Hendey B. Blood-brain barrier pathology in Alzheimer's and Parkinson's disease: implications for drug therapy. *Cell Transplant.* 2007;16(3):285-299.
28. Kermode AG, Thompson AJ, Tofts P, MacManus DG, Kendall BE, Kingsley DP, Moseley IF, Rudge P, McDonald WI. Breakdown of the blood-brain barrier precedes symptoms and other MRI signs of new lesions in multiple sclerosis. Pathogenetic and clinical implications. *Brain.* 1990;113 (Pt 5):1477-1489.
29. Long DM. Capillary ultrastructure and the blood-brain barrier in human malignant brain tumors. *J Neurosurg.* 1970;32(2):127-144.
30. Sandoval KE, Witt KA. Blood-brain barrier tight junction permeability and ischemic stroke. *Neurobiol Dis.* 2008;32(2):200-219.
31. Kroll RA, Neuwelt EA. Outwitting the blood-brain barrier for therapeutic purposes: Osmotic opening and other means. *Neurosurgery.* 1998;42(5):1083-1099.
32. Doolittle ND, Miner ME, Hall WA, Siegal T, Jerome E, Osztie E, McAllister LD, Bubalo JS, Kraemer DF, Fortin D, Nixon R, Muldoon LL, Neuwelt EA. Safety and efficacy of a multicenter study using intraarterial chemotherapy in conjunction with osmotic opening

of the blood-brain barrier for the treatment of patients with malignant brain tumors. *Cancer.* 2000;88(3):637-647.

33. Gabathuler R. Approaches to transport therapeutic drugs across the blood-brain barrier to treat brain diseases. *Neurobiol Dis.* 2010;37(1):48-57.

34. Oz G, Alger JR, Barker PB, Bartha R, Bizzi A, Boesch C, Bolan PJ, Brindle KM, Cudalbu C, Dincer A, Dydak U, Emir UE, Frahm J, Gonzalez RG, Gruber S, Gruetter R, Gupta RK, Heerschap A, Henning A, Hetherington HP, Howe FA, Huppi PS, Hurd RE, Kantarci K, Klomp DW, Kreis R, Kruiskamp MJ, Leach MO, Lin AP, Luijten PR, Marjanska M, Maudsley AA, Meyerhoff DJ, Mountford CE, Nelson SJ, Pamir MN, Pan JW, Peet AC, Poptani H, Posse S, Pouwels PJ, Ratai EM, Ross BD, Scheenen TW, Schuster C, Smith IC, Soher BJ, Tkac I, Vigneron DB, Kauppinen RA, Group MRSC. Clinical proton MR spectroscopy in central nervous system disorders. *Radiology.* 2014;270(3):658-679.

35. Kaila M, Kaila R. Quantum magnetic resonance imaging diagnostics of human brain disorders. *Elsevier insights*. Oxford: Elsevier,; 2010: https://yale.idm.oclc.org/login?URL=https://www.sciencedirect.com/science/book/9780123847119. Accessed.

36. Alnaes D, Kaufmann T, van der Meer D, Cordova-Palomera A, Rokicki J, Moberget T, Bettella F, Agartz I, Barch DM, Bertolino A, Brandt CL, Cervenka S, Djurovic S, Doan NT, Eisenacher S, Fatouros-Bergman H, Flyckt L, Di Giorgio A, Haatveit B, Jonsson EG, Kirsch P, Lund MJ, Meyer-Lindenberg A, Pergola G, Schwarz E, Smeland OB, Quarto T, Zink M, Andreassen OA, Westlye LT, Karolinska Schizophrenia Project C. Brain Heterogeneity in Schizophrenia and Its Association With Polygenic Risk. *JAMA Psychiatry.* 2019;76(7):739-748.

37. Young AL, Marinescu RV, Oxtoby NP, Bocchetta M, Yong K, Firth NC, Cash DM, Thomas DL, Dick KM, Cardoso J, van Swieten J, Borroni B, Galimberti D, Masellis M, Tartaglia MC, Rowe JB, Graff C, Tagliavini F, Frisoni GB, Laforce R, Jr., Finger E, de Mendonca A, Sorbi S, Warren JD, Crutch S, Fox NC, Ourselin S, Schott JM, Rohrer JD, Alexander DC, Genetic FTDI, Alzheimer's Disease Neuroimaging I. Uncovering the heterogeneity and temporal complexity of neurodegenerative diseases with Subtype and Stage Inference. *Nat Commun.* 2018;9(1):4273.

38. Ciccarelli O, Werring DJ, Barker GJ, Griffin CM, Wheeler-Kingshott CA, Miller DH, Thompson AJ. A study of the mechanisms of normal-appearing white matter damage in multiple sclerosis using diffusion tensor imaging--evidence of Wallerian degeneration. *J Neurol.* 2003;250(3):287-292.

39. Kearney H, Schneider T, Yiannakas MC, Altmann DR, Wheeler-Kingshott CA, Ciccarelli O, Miller DH. Spinal cord grey matter abnormalities are associated with secondary progression and physical disability in multiple sclerosis. *J Neurol Neurosurg Psychiatry.* 2015;86(6):608-614.

40. El Mendili MM, Cohen-Adad J, Pelegrini-Issac M, Rossignol S, Morizot-Koutlidis R, Marchand-Pauvert V, Iglesias C, Sangari S, Katz R, Lehericy S, Benali H, Pradat PF. Multi-parametric spinal cord MRI as potential progression marker in amyotrophic lateral sclerosis. *PLoS One.* 2014;9(4):e95516.

41. Demir A, Ries M, Moonen CT, Vital JM, Dehais J, Arne P, Caille JM, Dousset V. Diffusion-weighted MR imaging with apparent diffusion coefficient and apparent diffusion tensor maps in cervical spondylotic myelopathy. *Radiology.* 2003;229(1):37-43.

42. Wheeler-Kingshott CA, Stroman PW, Schwab JM, Bacon M, Bosma R, Brooks J, Cadotte DW, Carlstedt T, Ciccarelli O, Cohen-Adad J, Curt A, Evangelou N, Fehlings MG, Filippi M, Kelley BJ, Kollias S, Mackay A, Porro CA, Smith S, Strittmatter SM, Summers P, Thompson AJ, Tracey I. The current state-of-the-art of spinal cord imaging: applications. *Neuroimage.* 2014;84:1082-1093.
43. Stroman PW, Wheeler-Kingshott C, Bacon M, Schwab JM, Bosma R, Brooks J, Cadotte D, Carlstedt T, Ciccarelli O, Cohen-Adad J, Curt A, Evangelou N, Fehlings MG, Filippi M, Kelley BJ, Kollias S, Mackay A, Porro CA, Smith S, Strittmatter SM, Summers P, Tracey I. The current state-of-the-art of spinal cord imaging: methods. *Neuroimage.* 2014;84:1070-1081.
44. Barry RL, Vannesjo SJ, By S, Gore JC, Smith SA. Spinal cord MRI at 7T. *Neuroimage.* 2018;168:437-451.
45. Summers P, Staempfli P, Jaermann T, Kwiecinski S, Kollias S. A preliminary study of the effects of trigger timing on diffusion tensor imaging of the human spinal cord. *AJNR Am J Neuroradiol.* 2006;27(9):1952-1961.
46. Noll DC. Multishot rosette trajectories for spectrally selective MR imaging. *IEEE Trans Med Imaging.* 1997;16(4):372-377.
47. Schirda CV, Tanase C, Boada FE. Rosette spectroscopic imaging: optimal parameters for alias-free, high sensitivity spectroscopic imaging. *J Magn Reson Imaging.* 2009;29(6):1375-1385.
48. Schirda CV, Zhao T, Andronesi OC, Lee Y, Pan JW, Mountz JM, Hetherington HP, Boada FE. In vivo brain rosette spectroscopic imaging (RSI) with LASER excitation, constant gradient strength readout, and automated LCModel quantification for all voxels. *Magn Reson Med.* 2016;76(2):380-390.
49. Enoka RM, Duchateau J. Muscle fatigue: what, why and how it influences muscle function. *Journal of Physiology-London.* 2008;586(1):11-23.
50. Spencer CT, Byrne BJ, Bryant RM, Margossian R, Maisenbacher M, Breitenger P, Benni PB, Redfearn S, Marcus E, Cade WT. Impaired cardiac reserve and severely diminished skeletal muscle O(2) utilization mediate exercise intolerance in Barth syndrome. *Am J Physiol Heart Circ Physiol.* 2011;301(5):H2122-2129.
51. Taivassalo T, Jensen TD, Kennaway N, DiMauro S, Vissing J, Haller RG. The spectrum of exercise tolerance in mitochondrial myopathies: a study of 40 patients. *Brain.* 2003;126(Pt 2):413-423.
52. Mitchell JH, Sproule BJ, Chapman CB. The physiological meaning of the maximal oxygen intake test. *J Clin Invest.* 1958;37(4):538-547.
53. Nayler GL, Firmin DN, Longmore DB. Blood-Flow Imaging by Cine Magnetic-Resonance. *Journal of Computer Assisted Tomography.* 1986;10(5):715-722.
54. Pelc NJ, Herfkens RJ, Shimakawa A, Enzmann DR. Phase contrast cine magnetic resonance imaging. *Magn Reson Q.* 1991;7(4):229-254.
55. Langham MC, Jain V, Magland JF, Wehrli FW. Time-resolved absolute velocity quantification with projections. *Magn Reson Med.* 2010;64(6):1599-1606.
56. Mathewson KW, Haykowsky MJ, Thompson RB. Feasibility and reproducibility of measurement of whole muscle blood flow, oxygen extraction, and VO2 with dynamic exercise using MRI. *Magn Reson Med.* 2015;74(6):1640-1651.
57. Raynaud JS, Duteil S, Vaughan JT, Hennel F, Wary C, Leroy-Willig A, Carlier PG. Determination of skeletal muscle perfusion using arterial spin labeling NMRI: Validation

by comparison with venous occlusion plethysmography. *Magnetic Resonance in Medicine.* 2001;46(2):305-311.
58. Fernandez-Seara MA, Techawiboonwong A, Detre JA, Wehrli FW. MR susceptometry for measuring global brain oxygen extraction. *Magn Reson Med.* 2006;55(5):967-973.
59. Haacke EM, Lai S, Reichenbach JR, Kuppusamy K, Hoogenraad FG, Takeichi H, Lin W. In vivo measurement of blood oxygen saturation using magnetic resonance imaging: a direct validation of the blood oxygen level-dependent concept in functional brain imaging. *Hum Brain Mapp.* 1997;5(5):341-346.
60. Englund EK, Langham MC, Li C, Rodgers ZB, Floyd TF, Mohler ER, Wehrli FW. Combined measurement of perfusion, venous oxygen saturation, and skeletal muscle T-2* during reactive hyperemia in the leg. *Journal of Cardiovascular Magnetic Resonance.* 2013;15.
61. Kemp GJ, Ahmad RE, Nicolay K, Prompers JJ. Quantification of skeletal muscle mitochondrial function by 31P magnetic resonance spectroscopy techniques: a quantitative review. *Acta Physiol (Oxf).* 2015;213(1):107-144.
62. Bashir A, Bohnert KL, Reeds DN, Peterson LR, Bittel AJ, de Las Fuentes L, Pacak CA, Byrne BJ, Cade WT. Impaired cardiac and skeletal muscle bioenergetics in children, adolescents, and young adults with Barth syndrome. *Physiol Rep.* 2017;5(3).
63. Meyer RA. A linear model of muscle respiration explains monoexponential phosphocreatine changes. *Am J Physiol.* 1988;254(4 Pt 1):C548-553.
64. Baligand C, Wary C, Menard JC, Giacomini E, Hogrel JY, Carlier PG. Measuring perfusion and bioenergetics simultaneously in mouse skeletal muscle: a multiparametric functional-NMR approach. *NMR Biomed.* 2011;24(3):281-290.
65. Adelnia F, Cameron D, Bergeron CM, Fishbein KW, Spencer RG, Reiter DA, Ferrucci L. The Role of Muscle Perfusion in the Age-Associated Decline of Mitochondrial Function in Healthy Individuals. *Front Physiol.* 2019;10:427.
66. Wray DW, Nishiyama SK, Monnet A, Wary C, Duteil S, Carlier PG, Richhardson RS. Multiparametric NMR-Based Assessment of Skeletal Muscle Perfusion and Metabolism During Exercise in Elderly Persons: Preliminary Findings. *Journals of Gerontology Series a-Biological Sciences and Medical Sciences.* 2009;64(9):968-974.
67. Niess F, Schmid AI, Bogner W, Wolzt M, Carlier P, Trattnig S, Moser E, Meyerspeer M. Interleaved P-31 MRS/H-1 ASL for analysis of metabolic and functional heterogeneity along human lower leg muscles at 7T. *Magnetic Resonance in Medicine.* 2019.
68. Esposito F, Mathieu-Costello O, Shabetai R, Wagner PD, Richardson RS. Limited maximal exercise capacity in patients with chronic heart failure: partitioning the contributors. *J Am Coll Cardiol.* 2010;55(18):1945-1954.
69. Esposito F, Reese V, Shabetai R, Wagner PD, Richardson RS. Isolated quadriceps training increases maximal exercise capacity in chronic heart failure: the role of skeletal muscle convective and diffusive oxygen transport. *J Am Coll Cardiol.* 2011;58(13):1353-1362.
70. Bione S, D'Adamo P, Maestrini E, Gedeon AK, Bolhuis PA, Toniolo D. A novel X-linked gene, G4.5. is responsible for Barth syndrome. *Nat Genet.* 1996;12(4):385-389.
71. Mahmud SZ, Bashir A. Repeatability assessment for simultaneous measurement of arterial blood flow, venous oxygen saturation, and muscle perfusion following dynamic exercise. *NMR Biomed.* 2022:e4872.

72. Mathewson KW, Haykowsky MJ, Thompson RB. Feasibility and Reproducibility of Measurement of Whole Muscle Blood Flow, Oxygen Extraction, and VO2 with Dynamic Exercise Using MRI. *Magnetic Resonance in Medicine.* 2015;74(6):1640-1651.
73. Thompson RB, McVeigh ER. Real-time volumetric flow measurements with complex-difference MRI. *Magn Reson Med.* 2003;50(6):1248-1255.
74. Wehrli FW, Fan AP, Rodgers ZB, Englund EK, Langham MC. Susceptibility-based time-resolved whole-organ and regional tissue oximetry. *NMR Biomed.* 2017;30(4).
75. Wehrli FW, Rodgers ZB, Jain V, Langham MC, Li C, Licht DJ, Magland J. Time-resolved MRI oximetry for quantifying CMRO(2) and vascular reactivity. *Acad Radiol.* 2014;21(2):207-214.
76. Rodgers ZB, Jain V, Englund EK, Langham MC, Wehrli FW. High temporal resolution MRI quantification of global cerebral metabolic rate of oxygen consumption in response to apneic challenge. *J Cereb Blood Flow Metab.* 2013;33(10):1514-1522.
77. Kim SG. Quantification of relative cerebral blood flow change by flow-sensitive alternating inversion recovery (FAIR) technique: application to functional mapping. *Magn Reson Med.* 1995;34(3):293-301.
78. Gold GE, Han E, Stainsby J, Wright G, Brittain J, Beaulieu C. Musculoskeletal MRI at 3.0T: Relaxation times and image contrast. *American Journal of Roentgenology.* 2004;183(2):343-351.
79. Mahmud SZ, Gladden LB, Kavazis AN, Motl RW, Denney TS, Bashir A. Simultaneous Measurement of Perfusion and T2* in Calf Muscle at 7T with Submaximal Exercise using Radial Acquisition. *Sci Rep.* 2020;10(1):6342.
80. Niess F, Schmid AI, Bogner W, Wolzt M, Carlier P, Trattnig S, Moser E, Meyerspeer M. Interleaved (31) P MRS/(1) H ASL for analysis of metabolic and functional heterogeneity along human lower leg muscles at 7T. *Magn Reson Med.* 2020;83(6):1909-1919.
81. Englund EK, Rodgers ZB, Langham MC, Mohler ER, Floyd TF, Wehrli FW. Simultaneous measurement of macro- and microvascular blood flow and oxygen saturation for quantification of muscle oxygen consumption. *Magnetic Resonance in Medicine.* 2018;79(2):846-855.
82. Langham MC, Magland JF, Floyd TF, Wehrli FW. Retrospective correction for induced magnetic field inhomogeneity in measurements of large-vessel hemoglobin oxygen saturation by MR susceptometry. *Magn Reson Med.* 2009;61(3):626-633.
83. Li C, Langham MC, Epstein CL, Magland JF, Wu J, Gee J, Wehrli FW. Accuracy of the cylinder approximation for susceptometric measurement of intravascular oxygen saturation. *Magn Reson Med.* 2012;67(3):808-813.
84. Jain V, Abdulmalik O, Propert KJ, Wehrli FW. Investigating the magnetic susceptibility properties of fresh human blood for noninvasive oxygen saturation quantification. *Magn Reson Med.* 2012;68(3):863-867.
85. Naressi A, Couturier C, Devos JM, Janssen M, Mangeat C, de Beer R, Graveron-Demilly D. Java-based graphical user interface for the MRUI quantitation package. *MAGMA.* 2001;12(2-3):141-152.
86. Vanhamme L, van den Boogaart A, Van Huffel S. Improved method for accurate and efficient quantification of MRS data with use of prior knowledge. *Journal of Magnetic Resonance.* 1997;129(1):35-43.
87. Bashir A, Coggan AR, Gropler RJ. In vivo creatine kinase reaction kinetics at rest and stress in type II diabetic rat heart. *Physiol Rep.* 2015;3(1).

88. Bashir A, Gropler R. Reproducibility of creatine kinase reaction kinetics in human heart: a (31) P time-dependent saturation transfer spectroscopy study. *NMR Biomed.* 2014;27(6):663-671.
89. Kemp GJ, Meyerspeer M, Moser E. Absolute quantification of phosphorus metabolite concentrations in human muscle in vivo by 31P MRS: a quantitative review. *NMR Biomed.* 2007;20(6):555-565.
90. Atkinson G, Nevill AM. Statistical methods for assessing measurement error (reliability) in variables relevant to sports medicine. *Sports Med.* 1998;26(4):217-238.
91. Bland JM, Altman DG. Statistical Methods for Assessing Agreement between Two Methods of Clinical Measurement. *Lancet.* 1986;1(8476):307-310.
92. Pollak AW, Meyer CH, Epstein FH, Jiji RS, Hunter JR, DiMaria JM, Christopher JM, Kramer CM. Arterial Spin Labeling MR Imaging Reproducibly Measures Peak-Exercise Calf Muscle Perfusion A Study in Patients With Peripheral Arterial Disease and Healthy Volunteers. *Jacc-Cardiovascular Imaging.* 2012;5(12):1224-1230.
93. Barker A, Welsman J, Welford D, Fulford J, Williams C, Armstrong N. Reliability of 31P-magnetic resonance spectroscopy during an exhaustive incremental exercise test in children. *Eur J Appl Physiol.* 2006;98(6):556-565.
94. Layec G, Bringard A, Le Fur Y, Vilmen C, Micallef JP, Perrey S, Cozzone PJ, Bendahan D. Reproducibility assessment of metabolic variables characterizing muscle energetics in vivo: A 31P-MRS study. *Magn Reson Med.* 2009;62(4):840-854.
95. Roussel M, Bendahan D, Mattei JP, Le Fur Y, Cozzone PJ. 31P magnetic resonance spectroscopy study of phosphocreatine recovery kinetics in skeletal muscle: the issue of intersubject variability. *Biochim Biophys Acta.* 2000;1457(1-2):18-26.
96. Sedivy P, Kipfelsberger MC, Dezortova M, Krssak M, Drobny M, Chmelik M, Rydlo J, Trattnig S, Hajek M, Valkovic L. Dynamic 31P MR spectroscopy of plantar flexion: influence of ergometer design, magnetic field strength (3 and 7 T), and RF-coil design. *Med Phys.* 2015;42(4):1678-1689.
97. Nagaraj HM, Pednekar A, Corros C, Gupta H, Lloyd SG. Determining exercise-induced blood flow reserve in lower extremities using phase contrast MRI. *Journal of Magnetic Resonance Imaging.* 2008;27(5):1096-1102.
98. Clark MG. Impaired microvascular perfusion: a consequence of vascular dysfunction and a potential cause of insulin resistance in muscle. *Am J Physiol Endocrinol Metab.* 2008;295(4):E732-750.
99. Borsheim E, Bahr R. Effect of exercise intensity, duration and mode on post-exercise oxygen consumption. *Sports Med.* 2003;33(14):1037-1060.
100. Gaesser GA, Brooks GA. Metabolic bases of excess post-exercise oxygen consumption: a review. *Med Sci Sports Exerc.* 1984;16(1):29-43.
101. Raymer GH, Forbes SC, Kowalchuk JM, Thompson RT, Marsh GD. Prior exercise delays the onset of acidosis during incremental exercise. *J Appl Physiol (1985).* 2007;102(5):1799-1805.
102. Forbes SC, Raymer GH, Kowalchuk JM, Thompson RT, Marsh GD. Effects of recovery time on phosphocreatine kinetics during repeated bouts of heavy-intensity exercise. *Eur J Appl Physiol.* 2008;103(6):665-675.
103. Rebeles F, Fink J, Anzai Y, Maravilla KR. Blood-brain barrier imaging and therapeutic potentials. *Top Magn Reson Imaging.* 2006;17(2):107-116.

104. Avsenik J, Bisdas S, Popovic KS. Blood-brain barrier permeability imaging using perfusion computed tomography. *Radiol Oncol.* 2015;49(2):107-114.
105. Barbier EL, St Lawrence KS, Grillon E, Koretsky AP, Decorps M. A model of blood-brain barrier permeability to water: accounting for blood inflow and longitudinal relaxation effects. *Magn Reson Med.* 2002;47(6):1100-1109.
106. Starr JM, Farrall AJ, Armitage P, McGurn B, Wardlaw J. Blood-brain barrier permeability in Alzheimer's disease: a case-control MRI study. *Psychiatry Res.* 2009;171(3):232-241.
107. Heye AK, Thrippleton MJ, Armitage PA, Valdes Hernandez MDC, Makin SD, Glatz A, Sakka E, Wardlaw JM. Tracer kinetic modelling for DCE-MRI quantification of subtle blood-brain barrier permeability. *Neuroimage.* 2016;125:446-455.
108. Manning C, Stringer M, Dickie B, Clancy U, Valdes Hernandez MC, Wiseman SJ, Garcia DJ, Sakka E, Backes WH, Ingrisch M, Chappell F, Doubal F, Buckley C, Parkes LM, Parker GJM, Marshall I, Wardlaw JM, Thrippleton MJ. Sources of systematic error in DCE-MRI estimation of low-level blood-brain barrier leakage. *Magn Reson Med.* 2021;86(4):1888-1903.
109. Olchowy C, Cebulski K, Lasecki M, Chaber R, Olchowy A, Kalwak K, Zaleska-Dorobisz U. The presence of the gadolinium-based contrast agent depositions in the brain and symptoms of gadolinium neurotoxicity - A systematic review. *PLoS One.* 2017;12(2):e0171704.
110. Kanda T, Oba H, Toyoda K, Furui S. Recent Advances in Understanding Gadolinium Retention in the Brain. *AJNR Am J Neuroradiol.* 2016;37(1):E1-2.
111. Wong EC, Buxton RB, Frank LR. Quantitative imaging of perfusion using a single subtraction (QUIPSS and QUIPSS II). *Magn Reson Med.* 1998;39(5):702-708.
112. Alsop DC, Detre JA, Golay X, Gunther M, Hendrikse J, Hernandez-Garcia L, Lu H, MacIntosh BJ, Parkes LM, Smits M, van Osch MJ, Wang DJ, Wong EC, Zaharchuk G. Recommended implementation of arterial spin-labeled perfusion MRI for clinical applications: A consensus of the ISMRM perfusion study group and the European consortium for ASL in dementia. *Magn Reson Med.* 2015;73(1):102-116.
113. Cornford EM, Hyman S. Blood-brain barrier permeability to small and large molecules. *Adv Drug Deliv Rev.* 1999;36(2-3):145-163.
114. Gregori J, Schuff N, Kern R, Gunther M. T2-based arterial spin labeling measurements of blood to tissue water transfer in human brain. *Journal of Magnetic Resonance Imaging.* 2013;37(2):332-342.
115. Hales PW, Clark CA. Combined arterial spin labeling and diffusion-weighted imaging for noninvasive estimation of capillary volume fraction and permeability-surface product in the human brain. *J Cereb Blood Flow Metab.* 2013;33(1):67-75.
116. Wells JA, Siow B, Lythgoe MF, Thomas DL. Measuring biexponential transverse relaxation of the ASL signal at 9.4 T to estimate arterial oxygen saturation and the time of exchange of labeled blood water into cortical brain tissue. *Journal of Cerebral Blood Flow and Metabolism.* 2013;33(2):215-224.
117. Lin ZX, Li Y, Su P, Mao D, Wei ZL, Pillai JJ, Moghekar A, van Osch M, Ge YL, Lu HZ. Non-contrast MR imaging of blood-brain barrier permeability to water. *Magnetic Resonance in Medicine.* 2018;80(4):1507-1520.

118. Lawrence KS, Owen D, Wang DJJ. A two-stage approach for measuring vascular water exchange and arterial transit time by diffusion-weighted perfusion MRI. *Magnetic Resonance in Medicine.* 2012;67(5):1275-1284.
119. Shao XF, Ma SJ, Casey M, D'Orazio L, Ringman JM, Wang DJJ. Mapping water exchange across the blood-brain barrier using 3D diffusion-prepared arterial spin labeled perfusion MRI. *Magnetic Resonance in Medicine.* 2019;81(5):3065-3079.
120. Wang JJ, Fernandez-Seara MA, Wang SM, St Lawrence KS. When perfusion meets diffusion: in vivo measurement of water permeability in human brain. *Journal of Cerebral Blood Flow and Metabolism.* 2007;27(4):839-849.
121. Wengler K, Bangiyev L, Canli T, Duong TQ, Schweitzer ME, He X. 3D MRI of whole-brain water permeability with intrinsic diffusivity encoding of arterial labeled spin (IDEALS). *Neuroimage.* 2019;189:401-414.
122. Balaban RS, Ceckler TL. Magnetization transfer contrast in magnetic resonance imaging. *Magn Reson Q.* 1992;8(2):116-137.
123. Dousset V, Degreze P, Mieze S, Sesay M, BasseCathalinat B, Caille JM. Magnetization transfer on in vitro circulating blood: Implications for time-of-flight MR angiography. *Jmri-Journal of Magnetic Resonance Imaging.* 1995;5(6):786-788.
124. Kim SG, Tsekos NV. Perfusion imaging by a flow-sensitive alternating inversion recovery (FAIR) technique: application to functional brain imaging. *Magn Reson Med.* 1997;37(3):425-435.
125. Sled JG. Modelling and interpretation of magnetization transfer imaging in the brain. *Neuroimage.* 2018;182:128-135.
126. Mahmud SZ, Denney TS, Bashir A. Non-contrast estimate of blood-brain barrier permeability in humans using arterial spin labeling and magnetization transfer at 7 T. *NMR Biomed.* 2023:e4908.
127. Wong EC, Buxton RB, Frank LR. Implementation of quantitative perfusion imaging techniques for functional brain mapping using pulsed arterial spin labeling. *NMR Biomed.* 1997;10(4-5):237-249.
128. Alsop DC, Detre JA. Reduced transit-time sensitivity in noninvasive magnetic resonance imaging of human cerebral blood flow. *J Cereb Blood Flow Metab.* 1996;16(6):1236-1249.
129. Buxton RB, Frank LR, Wong EC, Siewert B, Warach S, Edelman RR. A general kinetic model for quantitative perfusion imaging with arterial spin labeling. *Magn Reson Med.* 1998;40(3):383-396.
130. Barber TW, Brockway JA, Higgins LS. The density of tissues in and about the head. *Acta Neurol Scand.* 1970;46(1):85-92.
131. Renkin EM. Transport of potassium-42 from blood to tissue in isolated mammalian skeletal muscles. *Am J Physiol.* 1959;197:1205-1210.
132. Crone C. The Permeability of Capillaries in Various Organs as Determined by Use of the 'Indicator Diffusion' Method. *Acta Physiol Scand.* 1963;58:292-305.
133. Grossman RI, Gomori JM, Ramer KN, Lexa FJ, Schnall MD. Magnetization-Transfer - Theory and Clinical-Applications in Neuroradiology. *Radiographics.* 1994;14(2):279-290.
134. van Gelderen P, Jiang X, Duyn JH. Effects of magnetization transfer on T-1 contrast in human brain white matter. *Neuroimage.* 2016;128:85-95.

135. van Gelderen P, Jiang X, Duyn JH. Rapid measurement of brain macromolecular proton fraction with transient saturation transfer MRI. *Magn Reson Med.* 2017;77(6):2174-2185.
136. Addicott MA, Yang LL, Peiffer AM, Burnett LR, Burdette JH, Chen MY, Hayasaka S, Kraft RA, Maldjian JA, Laurienti PJ. The Effect of Daily Caffeine Use on Cerebral Blood Flow: How Much Caffeine can we Tolerate? *Human Brain Mapping.* 2009;30(10):3102-3114.
137. Chappell M, MacIntosh B, Okell T, Oxford University P. Introduction to perfusion quantification using arterial spin labeling. Oxford, United Kingdom: Oxford University Press; 2018: https://public.ebookcentral.proquest.com/choice/publicfullrecord.aspx?p=5891340 http://VH7QX3XE2P.search.serialssolutions.com/?V=1.0&L=VH7QX3XE2P&S=JCs&C=TC0002012577&T=marc&tab=BOOKS http://VH7QX3XE2P.search.serialssolutions.com/?V=1.0&L=VH7QX3XE2P&S=AC_T_B&C=Introduction%20to%20Perfusion%20Quantification%20using%20Arterial%20Spin%20Labelling&T=marc&tab=BOOKS. Accessed.
138. Chen Y, Wang DJ, Detre JA. Comparison of arterial transit times estimated using arterial spin labeling. *MAGMA.* 2012;25(2):135-144.
139. Ito H, Kanno I, Ibaraki M, Hatazawa J, Miura S. Changes in human cerebral blood flow and cerebral blood volume during hypercapnia and hypocapnia measured by positron emission tomography. *J Cereb Blood Flow Metab.* 2003;23(6):665-670.
140. Ito H, Takahashi K, Hatazawa J, Kim SG, Kanno I. Changes in human regional cerebral blood flow and cerebral blood volume during visual stimulation measured by positron emission tomography. *J Cereb Blood Flow Metab.* 2001;21(5):608-612.
141. Ito H, Kanno I, Shimosegawa E, Tamura H, Okane K, Hatazawa J. Hemodynamic changes during neural deactivation in human brain: a positron emission tomography study of crossed cerebellar diaschisis. *Ann Nucl Med.* 2002;16(4):249-254.
142. Wong EC, Buxton RB, Frank LR. A theoretical and experimental comparison of continuous and pulsed arterial spin labeling techniques for quantitative perfusion imaging. *Magnetic Resonance in Medicine.* 1998;40(3):348-355.
143. Zhang X, Petersen ET, Ghariq E, De Vis JB, Webb AG, Teeuwisse WM, Hendrikse J, van Osch MJ. In vivo blood T(1) measurements at 1.5 T, 3 T, and 7 T. *Magn Reson Med.* 2013;70(4):1082-1086.
144. Herscovitch P, Raichle ME. What Is the Correct Value for the Brain Blood Partition-Coefficient for Water. *Journal of Cerebral Blood Flow and Metabolism.* 1985;5(1):65-69.
145. Reinstrup P, Ryding E, Ohlsson T, Dahm PL, Uski T. Cerebral blood volume (CBV) in humans during normo- and hypocapnia: influence of nitrous oxide (N(2)O). *Anesthesiology.* 2001;95(5):1079-1082.
146. Herscovitch P, Raichle ME, Kilbourn MR, Welch MJ. Positron emission tomographic measurement of cerebral blood flow and permeability-surface area product of water using [15O]water and [11C]butanol. *J Cereb Blood Flow Metab.* 1987;7(5):527-542.
147. Schepers J, van Osch MJ, Bartels LW, Heukels SN, Viergever MA, Nicolay K. The effect of B1 field inhomogeneity and the nonselective inversion profile on the kinetics of FAIR-based perfusion MRI. *Magn Reson Med.* 2005;53(6):1355-1362.
148. Gardener AG, Jezzard P. Investigating white matter perfusion using optimal sampling strategy arterial spin labeling at 7 Tesla. *Magn Reson Med.* 2015;73(6):2243-2248.

149. Wu WC, Fernandez-Seara M, Detre JA, Wehrli FW, Wang J. A theoretical and experimental investigation of the tagging efficiency of pseudocontinuous arterial spin labeling. *Magn Reson Med.* 2007;58(5):1020-1027.
150. Gunther M, Oshio K, Feinberg DA. Single-shot 3D imaging techniques improve arterial spin labeling perfusion measurements. *Magn Reson Med.* 2005;54(2):491-498.
151. Zuo Z, Wang R, Zhuo Y, Xue R, St Lawrence KS, Wang DJ. Turbo-FLASH based arterial spin labeled perfusion MRI at 7 T. *PLoS One.* 2013;8(6):e66612.
152. Raichle ME, Eichling JO, Straatmann MG, Welch MJ, Larson KB, Terpogossian MM. Blood-Brain-Barrier Permeability of C-11-Labeled Alcohols and O-15-Labeled Water. *American Journal of Physiology.* 1976;230(2):543-552.
153. Berridge MS, Adler LP, Nelson AD, Cassidy EH, Muzic RF, Bednarczyk EM, Miraldi F. Measurement of human cerebral blood flow with [15O]butanol and positron emission tomography. *J Cereb Blood Flow Metab.* 1991;11(5):707-715.
154. Mathew RJ, Wilson WH. Caffeine induced changes in cerebral circulation. *Stroke.* 1985;16(5):814-817.
155. Back G, Seidel G, Endell W. Effects of caffeine and ethanol on the blood-brain barrier in rats. *Pharmacology.* 1976;14(1):67-75.
156. Chen X, Gawryluk JW, Wagener JF, Ghribi O, Geiger JD. Caffeine blocks disruption of blood brain barrier in a rabbit model of Alzheimer's disease. *J Neuroinflammation.* 2008;5:12.
157. Chen X, Ghribi O, Geiger JD. Caffeine protects against disruptions of the blood-brain barrier in animal models of Alzheimer's and Parkinson's diseases. *J Alzheimers Dis.* 2010;20 Suppl 1(Suppl 1):S127-141.
158. Chen X, Lan X, Roche I, Liu R, Geiger JD. Caffeine protects against MPTP-induced blood-brain barrier dysfunction in mouse striatum. *J Neurochem.* 2008;107(4):1147-1157.
159. Qosa H, Abuznait AH, Hill RA, Kaddoumi A. Enhanced brain amyloid-beta clearance by rifampicin and caffeine as a possible protective mechanism against Alzheimer's disease. *J Alzheimers Dis.* 2012;31(1):151-165.
160. Ribeiro JA, Sebastiao AM. Caffeine and adenosine. *J Alzheimers Dis.* 2010;20 Suppl 1:S3-15.
161. Hurtado-Alvarado G, Dominguez-Salazar E, Velazquez-Moctezuma J, Gomez-Gonzalez B. A2A Adenosine Receptor Antagonism Reverts the Blood-Brain Barrier Dysfunction Induced by Sleep Restriction. *PLoS One.* 2016;11(11):e0167236.
162. Rieg T, Vallon V. ATP and adenosine in the local regulation of water transport and homeostasis by the kidney. *Am J Physiol Regul Integr Comp Physiol.* 2009;296(2):R419-427.
163. Lee J, Ha JH, Kim S, Oh Y, Kim SW. Caffeine decreases the expression of Na+/K+-ATPase and the type 3 Na+/H+ exchanger in rat kidney. *Clin Exp Pharmacol Physiol.* 2002;29(7):559-563.
164. Bai R, Springer CS, Jr., Plenz D, Basser PJ. Fast, Na(+) /K(+) pump driven, steady-state transcytolemmal water exchange in neuronal tissue: A study of rat brain cortical cultures. *Magn Reson Med.* 2018;79(6):3207-3217.
165. Bai R, Springer CS, Jr., Plenz D, Basser PJ. Brain active transmembrane water cycling measured by MR is associated with neuronal activity. *Magn Reson Med.* 2019;81(2):1280-1295.

166. Schwarzbauer C, Morrissey SP, Deichmann R, Hillenbrand C, Syha J, Adolf H, Noth U, Haase A. Quantitative magnetic resonance imaging of capillary water permeability and regional blood volume with an intravascular MR contrast agent. *Magn Reson Med.* 1997;37(5):769-777.
167. Rooney WD, Li X, Sammi MK, Bourdette DN, Neuwelt EA, Springer CS, Jr. Mapping human brain capillary water lifetime: high-resolution metabolic neuroimaging. *NMR Biomed.* 2015;28(6):607-623.
168. Carr JP, Buckley DL, Tessier J, Parker GJM. What levels of precision are achievable for quantification of perfusion and capillary permeability surface area product using ASL? *Magnetic Resonance in Medicine.* 2007;58(2):281-289.
169. Kim YR, Tejima E, Huang S, Atochin DN, Dai G, Lo EH, Huang PL, Bogdanov A, Jr., Rosen BR. In vivo quantification of transvascular water exchange during the acute phase of permanent stroke. *Magn Reson Med.* 2008;60(4):813-821.
170. Neil JJ, Bosch CS, Ackerman JJH. An Evaluation of the Sensitivity of the Intravoxel Incoherent Motion (Ivim) Method of Blood-Flow Measurement to Changes in Cerebral Blood-Flow. *Magnetic Resonance in Medicine.* 1994;32(1):60-65.
171. Neil JJ, Ackerman JJH. Detection of Pseudodiffusion in Rat-Brain Following Blood Substitution with Perfluorocarbon. *Journal of Magnetic Resonance.* 1992;97(1):194-201.
172. Lin Z, Li Y, Su P, Mao D, Wei Z, Pillai JJ, Moghekar A, van Osch M, Ge Y, Lu H. Non-contrast MR imaging of blood-brain barrier permeability to water. *Magn Reson Med.* 2018;80(4):1507-1520.
173. Liu Z, Pardini M, Yaldizli O, Sethi V, Muhlert N, Wheeler-Kingshott CAM, Samson RS, Miller DH, Chard DT. Magnetization transfer ratio measures in normal-appearing white matter show periventricular gradient abnormalities in multiple sclerosis. *Brain.* 2015;138:1239-1246.
174. Chappell MA, Woolrich MW, Kazan S, Jezzard P, Payne SJ, MacIntosh BJ. Modeling dispersion in arterial spin labeling: validation using dynamic angiographic measurements. *Magn Reson Med.* 2013;69(2):563-570.
175. Luh WM, Wong EC, Bandettini PA, Hyde JS. QUIPSS II with thin-slice TI1 periodic saturation: a method for improving accuracy of quantitative perfusion imaging using pulsed arterial spin labeling. *Magn Reson Med.* 1999;41(6):1246-1254.
176. Henning A, Fuchs A, Murdoch JB, Boesiger P. Slice-selective FID acquisition, localized by outer volume suppression (FIDLOVS) for (1)H-MRSI of the human brain at 7 T with minimal signal loss. *NMR Biomed.* 2009;22(7):683-696.
177. Bogner W, Gruber S, Trattnig S, Chmelik M. High-resolution mapping of human brain metabolites by free induction decay (1)H MRSI at 7 T. *NMR Biomed.* 2012;25(6):873-882.
178. Scheenen TW, Heerschap A, Klomp DW. Towards 1H-MRSI of the human brain at 7T with slice-selective adiabatic refocusing pulses. *MAGMA.* 2008;21(1-2):95-101.
179. Nassirpour S, Chang P, Avdievitch N, Henning A. Compressed sensing for high-resolution nonlipid suppressed (1) H FID MRSI of the human brain at 9.4T. *Magn Reson Med.* 2018;80(6):2311-2325.
180. Boer VO, Klomp DW, Juchem C, Luijten PR, de Graaf RA. Multislice (1)H MRSI of the human brain at 7 T using dynamic B(0) and B(1) shimming. *Magn Reson Med.* 2012;68(3):662-670.

181. Strasser B, Povazan M, Hangel G, Hingerl L, Chmelik M, Gruber S, Trattnig S, Bogner W. (2 + 1)D-CAIPIRINHA accelerated MR spectroscopic imaging of the brain at 7T. *Magn Reson Med.* 2017;78(2):429-440.
182. Hangel G, Strasser B, Povazan M, Heckova E, Hingerl L, Boubela R, Gruber S, Trattnig S, Bogner W. Ultra-high resolution brain metabolite mapping at 7 T by short-TR Hadamard-encoded FID-MRSI. *Neuroimage.* 2018;168:199-210.
183. Hangel G, Strasser B, Povazan M, Gruber S, Chmelik M, Gajdosik M, Trattnig S, Bogner W. Lipid suppression via double inversion recovery with symmetric frequency sweep for robust 2D-GRAPPA-accelerated MRSI of the brain at 7 T. *NMR Biomed.* 2015;28(11):1413-1425.
184. Kirchner T, Fillmer A, Tsao J, Pruessmann KP, Henning A. Reduction of voxel bleeding in highly accelerated parallel (1) H MRSI by direct control of the spatial response function. *Magn Reson Med.* 2015;73(2):469-480.
185. Donoho DL. Compressed sensing. *IEEE Transactions on Information Theory.* 2006;52(4):1289-1306.
186. Lustig M, Donoho D, Pauly JM. Sparse MRI: The application of compressed sensing for rapid MR imaging. *Magn Reson Med.* 2007;58(6):1182-1195.
187. Cao P, Wu EX. Accelerating phase-encoded proton MR spectroscopic imaging by compressed sensing. *J Magn Reson Imaging.* 2015;41(2):487-495.
188. Chatnuntawech I, Gagoski B, Bilgic B, Cauley SF, Setsompop K, Adalsteinsson E. Accelerated (1) H MRSI using randomly undersampled spiral-based k-space trajectories. *Magn Reson Med.* 2015;74(1):13-24.
189. Geethanath S, Baek HM, Ganji SK, Ding Y, Maher EA, Sims RD, Choi C, Lewis MA, Kodibagkar VD. Compressive sensing could accelerate 1H MR metabolic imaging in the clinic. *Radiology.* 2012;262(3):985-994.
190. Klauser A, Strasser B, Thapa B, Lazeyras F, Andronesi O. Achieving high-resolution (1)H-MRSI of the human brain with compressed-sensing and low-rank reconstruction at 7 Tesla. *J Magn Reson.* 2021;331:107048.
191. Adalsteinsson E, Irarrazabal P, Topp S, Meyer C, Macovski A, Spielman DM. Volumetric spectroscopic imaging with spiral-based k-space trajectories. *Magn Reson Med.* 1998;39(6):889-898.
192. Sabati M, Sheriff S, Gu M, Wei J, Zhu H, Barker PB, Spielman DM, Alger JR, Maudsley AA. Multivendor implementation and comparison of volumetric whole-brain echo-planar MR spectroscopic imaging. *Magn Reson Med.* 2015;74(5):1209-1220.
193. Schirda C, Zhao T, Hetherington H, Yushmanov V, Pan JJPpaI. Rosette spectroscopic imaging (RSI) of human brain at 7T. Paper presented at: Proc. Intl. Soc. Mag. Reson. Med., 2016.
194. Cunningham CH, Vigneron DB, Chen AP, Xu D, Nelson SJ, Hurd RE, Kelley DA, Pauly JM. Design of flyback echo-planar readout gradients for magnetic resonance spectroscopic imaging. *Magn Reson Med.* 2005;54(5):1286-1289.
195. Bogner W, Otazo R, Henning A. Accelerated MR spectroscopic imaging-a review of current and emerging techniques. *NMR Biomed.* 2021;34(5):e4314.
196. Li Y, Yang R, Zhang C, Zhang J, Jia S, Zhou Z. Analysis of generalized rosette trajectory for compressed sensing MRI. *Med Phys.* 2015;42(9):5530-5544.
197. Schirda CV, Zhao T, Yushmanov VE, Lee Y, Ghearing GR, Lieberman FS, Panigrahy A, Hetherington HP, Pan JW. Fast 3D rosette spectroscopic imaging of neocortical

abnormalities at 3 T: Assessment of spectral quality. *Magn Reson Med.* 2018;79(5):2470-2480.
198. Tal A, Zhao T, Schirda C, Hetherington HP, Pan JW, Gonen O. Fast, regional three-dimensional hybrid (1D-Hadamard 2D-rosette) proton MR spectroscopic imaging in the human temporal lobes. *NMR Biomed.* 2021;34(6):e4507.
199. Ogg RJ, Kingsley PB, Taylor JS. WET, a T1- and B1-insensitive water-suppression method for in vivo localized 1H NMR spectroscopy. *J Magn Reson B.* 1994;104(1):1-10.
200. Nassirpour S, Chang P, Henning A. High and ultra-high resolution metabolite mapping of the human brain using (1)H FID MRSI at 9.4T. *Neuroimage.* 2018;168:211-221.
201. Strasser B, Chmelik M, Robinson SD, Hangel G, Gruber S, Trattnig S, Bogner W. Coil combination of multichannel MRSI data at 7 T: MUSICAL. *NMR Biomed.* 2013;26(12):1796-1805.
202. Moser P, Bogner W, Hingerl L, Heckova E, Hangel G, Motyka S, Trattnig S, Strasser B. Non-Cartesian GRAPPA and coil combination using interleaved calibration data - application to concentric-ring MRSI of the human brain at 7T. *Magn Reson Med.* 2019;82(5):1587-1603.
203. Provencher SW. Estimation of metabolite concentrations from localized in vivo proton NMR spectra. *Magn Reson Med.* 1993;30(6):672-679.
204. Irarrazabal P, Meyer CH, Nishimura DG, Macovski A. Inhomogeneity correction using an estimated linear field map. *Magn Reson Med.* 1996;35(2):278-282.
205. Hingerl L, Bogner W, Moser P, Povazan M, Hangel G, Heckova E, Gruber S, Trattnig S, Strasser B. Density-weighted concentric circle trajectories for high resolution brain magnetic resonance spectroscopic imaging at 7T. *Magn Reson Med.* 2018;79(6):2874-2885.
206. Mayer D, Levin YS, Hurd RE, Glover GH, Spielman DM. Fast metabolic imaging of systems with sparse spectra: application for hyperpolarized 13C imaging. *Magn Reson Med.* 2006;56(4):932-937.
207. Jackson JI, Meyer CH, Nishimura DG, Macovski A. Selection of a convolution function for Fourier inversion using gridding [computerised tomography application]. *IEEE Trans Med Imaging.* 1991;10(3):473-478.
208. Bucholz EK, Song J, Johnson GA, Hancu I. Multispectral imaging with three-dimensional rosette trajectories. *Magn Reson Med.* 2008;59(3):581-589.
209. Bilgic B, Chatnuntawech I, Fan AP, Setsompop K, Cauley SF, Wald LL, Adalsteinsson E. Fast image reconstruction with L2-regularization. *J Magn Reson Imaging.* 2014;40(1):181-191.
210. Simpson R, Devenyi GA, Jezzard P, Hennessy TJ, Near J. Advanced processing and simulation of MRS data using the FID appliance (FID-A)-An open source, MATLAB-based toolkit. *Magn Reson Med.* 2017;77(1):23-33.
211. Furuyama JK, Wilson NE, Thomas MA. Spectroscopic imaging using concentrically circular echo-planar trajectories in vivo. *Magn Reson Med.* 2012;67(6):1515-1522.
212. de Graaf RA, Brown PB, McIntyre S, Nixon TW, Behar KL, Rothman DL. High magnetic field water and metabolite proton T1 and T2 relaxation in rat brain in vivo. *Magn Reson Med.* 2006;56(2):386-394.
213. Chang P, Nassirpour S, Avdievitch N, Henning A. Non-water-suppressed (1) H FID-MRSI at 3T and 9.4T. *Magn Reson Med.* 2018;80(2):442-451.

214. Fillmer A, Kirchner T, Cameron D, Henning A. Constrained image-based B0 shimming accounting for "local minimum traps" in the optimization and field inhomogeneities outside the region of interest. *Magn Reson Med.* 2015;73(4):1370-1380.
215. Pan JW, Lo KM, Hetherington HP. Role of very high order and degree B0 shimming for spectroscopic imaging of the human brain at 7 tesla. *Magnetic Resonance in Medicine.* 2012;68(4):1007-1017.
216. Xu D, Cunningham CH, Chen AP, Li Y, Kelley DA, Mukherjee P, Pauly JM, Nelson SJ, Vigneron DB. Phased array 3D MR spectroscopic imaging of the brain at 7 T. *Magn Reson Imaging.* 2008;26(9):1201-1206.
217. Balchandani P, Pauly J, Spielman D. Interleaved narrow-band PRESS sequence with adiabatic spatial-spectral refocusing pulses for 1H MRSI at 7T. *Magn Reson Med.* 2008;59(5):973-979.
218. Zölch N. High Precision External Reference Standards for Quantitative in vivo Magnetic Resonance Spectroscopy, 2016.
219. Gasparovic C, Song T, Devier D, Bockholt HJ, Caprihan A, Mullins PG, Posse S, Jung RE, Morrison LA. Use of tissue water as a concentration reference for proton spectroscopic imaging. *Magn Reson Med.* 2006;55(6):1219-1226.
220. Povazan M, Hangel G, Strasser B, Gruber S, Chmelik M, Trattnig S, Bogner W. Mapping of brain macromolecules and their use for spectral processing of (1)H-MRSI data with an ultra-short acquisition delay at 7 T. *Neuroimage.* 2015;121:126-135.
221. Seeger U, Klose U, Mader I, Grodd W, Nagele T. Parameterized evaluation of macromolecules and lipids in proton MR spectroscopy of brain diseases. *Magn Reson Med.* 2003;49(1):19-28.
222. Zhao W, Cohen-Adad J, Polimeni JR, Keil B, Guerin B, Setsompop K, Serano P, Mareyam A, Hoecht P, Wald LL. Nineteen-channel receive array and four-channel transmit array coil for cervical spinal cord imaging at 7T. *Magn Reson Med.* 2014;72(1):291-300.
223. Zhang B, Seifert AC, Kim JW, Borrello J, Xu J. 7 Tesla 22-channel wrap-around coil array for cervical spinal cord and brainstem imaging. *Magn Reson Med.* 2017;78(4):1623-1634.
224. Massire A, Taso M, Besson P, Guye M, Ranjeva JP, Callot V. High-resolution multi-parametric quantitative magnetic resonance imaging of the human cervical spinal cord at 7T. *Neuroimage.* 2016;143:58-69.
225. Duan Q, Nair G, Gudino N, de Zwart JA, van Gelderen P, Murphy-Boesch J, Reich DS, Duyn JH, Merkle H. A 7T spine array based on electric dipole transmitters. *Magn Reson Med.* 2015;74(4):1189-1197.
226. Figley CR, Stroman PW. Measurement and characterization of the human spinal cord SEEP response using event-related spinal fMRI. *Magn Reson Imaging.* 2012;30(4):471-484.
227. Noll DC, Peltier SJ, Boada FE. Simultaneous multislice acquisition using rosette trajectories (SMART): a new imaging method for functional MRI. *Magn Reson Med.* 1998;39(5):709-716.
228. Wilm BJ, Barmet C, Gross S, Kasper L, Vannesjo SJ, Haeberlin M, Dietrich BE, Brunner DO, Schmid T, Pruessmann KP. Single-shot spiral imaging enabled by an expanded encoding model: Demonstration in diffusion MRI. *Magn Reson Med.* 2017;77(1):83-91.

229. Liu C, Bammer R, Kim DH, Moseley ME. Self-navigated interleaved spiral (SNAILS): application to high-resolution diffusion tensor imaging. *Magn Reson Med.* 2004;52(6):1388-1396.
230. Li Z, Schar M, Wang D, Zwart NR, Madhuranthakam AJ, Karis JP, Pipe JG. Arterial spin labeled perfusion imaging using three-dimensional turbo spin echo with a distributed spiral-in/out trajectory. *Magn Reson Med.* 2016;75(1):266-273.
231. Robison RK, Cornejo P, Kuwabara M, Ooi MB, Temkit H, Miller JH. Evaluation of axial gradient Echo spiral MRI of the spine at 1.5 T. *Magn Reson Imaging.* 2022;89:24-32.
232. Brown RA, Narayanan S, Arnold DL. Segmentation of magnetization transfer ratio lesions for longitudinal analysis of demyelination and remyelination in multiple sclerosis. *Neuroimage.* 2013;66:103-109.
233. McCreary CR, Bjarnason TA, Skihar V, Mitchell JR, Yong VW, Dunn JF. Multiexponential T2 and magnetization transfer MRI of demyelination and remyelination in murine spinal cord. *Neuroimage.* 2009;45(4):1173-1182.
234. Smith SA, Golay X, Fatemi A, Jones CK, Raymond GV, Moser HW, van Zijl PC. Magnetization transfer weighted imaging in the upper cervical spinal cord using cerebrospinal fluid as intersubject normalization reference (MTCSF imaging). *Magn Reson Med.* 2005;54(1):201-206.
235. Candes EJ, Romberg J, Tao T. Robust uncertainty principles: exact signal reconstruction from highly incomplete frequency information. *IEEE Transactions on Information Theory.* 2006;52(2):489-509.
236. Wang H, Miao Y, Zhou K, Yu Y, Bao S, He Q, Dai Y, Xuan SY, Tarabishy B, Ye Y, Hu J. Feasibility of high temporal resolution breast DCE-MRI using compressed sensing theory. *Med Phys.* 2010;37(9):4971-4981.
237. Zhang T, Chowdhury S, Lustig M, Barth RA, Alley MT, Grafendorfer T, Calderon PD, Robb FJ, Pauly JM, Vasanawala SS. Clinical performance of contrast enhanced abdominal pediatric MRI with fast combined parallel imaging compressed sensing reconstruction. *J Magn Reson Imaging.* 2014;40(1):13-25.
238. Hsiao A, Lustig M, Alley MT, Murphy M, Chan FP, Herfkens RJ, Vasanawala SS. Rapid pediatric cardiac assessment of flow and ventricular volume with compressed sensing parallel imaging volumetric cine phase-contrast MRI. *AJR Am J Roentgenol.* 2012;198(3):W250-259.
239. Worters PW, Sung K, Stevens KJ, Koch KM, Hargreaves BA. Compressed-sensing multispectral imaging of the postoperative spine. *J Magn Reson Imaging.* 2013;37(1):243-248.
240. Magnotta VA, Friedman L, First B. Measurement of Signal-to-Noise and Contrast-to-Noise in the fBIRN Multicenter Imaging Study. *J Digit Imaging.* 2006;19(2):140-147.
241. Wolff SD, Balaban RS. Magnetization transfer contrast (MTC) and tissue water proton relaxation in vivo. *Magn Reson Med.* 1989;10(1):135-144.
242. Feng L, Grimm R, Block KT, Chandarana H, Kim S, Xu J, Axel L, Sodickson DK, Otazo R. Golden-angle radial sparse parallel MRI: combination of compressed sensing, parallel imaging, and golden-angle radial sampling for fast and flexible dynamic volumetric MRI. *Magn Reson Med.* 2014;72(3):707-717.
243. De Leener B, Lévy S, Dupont SM, Fonov VS, Stikov N, Collins DL, Callot V, Cohen-Adad J. SCT: Spinal Cord Toolbox, an open-source software for processing spinal cord MRI data. *Neuroimage.* 2017;145:24-43.

244. Henning A, Koning W, Fuchs A, Raaijmakers A, Bluemink JJ, van den Berg CA, Boer VO, Klomp DW. (1) H MRS in the human spinal cord at 7 T using a dielectric waveguide transmitter, RF shimming and a high density receive array. *NMR Biomed.* 2016;29(9):1231-1239.

245. Eryaman Y, Guerin B, Keil B, Mareyam A, Herraiz JL, Kosior RK, Martin A, Torrado-Carvajal A, Malpica N, Hernandez-Tamames JA, Schiavi E, Adalsteinsson E, Wald LL. SAR reduction in 7T C-spine imaging using a "dark modes" transmit array strategy. *Magn Reson Med.* 2015;73(4):1533-1539.